NOTICE

The quality of this microform is heavily dependent upon the quality of the original thesis submitted for microfilming. Every effort has been made to ensure the highest quality of reproduction possible.

If pages are missing, contact the university which granted the degree.

Some pages may have indistinct print especially if the original pages were typed with a poor typewriter ribbon or if the university sent us an inferior photocopy.

Reproduction in full or in part of this microform is governed by the Canadian Copyright Act, R.S.C. 1970, c. C-30, and subsequent amendments.

AVIS

La qualité de cette microforme dépend grandement de la qualité de la thèse soumise au microfilmage. Nous avons tout fait pour assurer une qualité supérieure de reproduction.

S'il manque des pages, veuillez communiquer avec l'université qui a conféré le grade.

La qualité d'impression de certaines pages peut laisser à désirer, surtout si les pages originales ont été dactylographiées à l'aide d'un ruban usé ou si l'université nous a fait parvenir une photocopie de qualité inférieure.

La reproduction, même partielle, de cette microforme est soumise à la Loi canadienne sur le droit d'auteur, SRC 1970, c. C-30, et ses amendements subséquents.

Canada

RADIATIVE TRANSFER IN CLOUDS WITH INTERNAL INHOMOGENEITY

By

Jiangnan Li

SUBMITTED IN PARTIAL FULFILLMENT OF THE
REQUIREMENTS FOR THE DEGREE OF
DOCTOR OF PHILOSOPHY
AT
DALHOUSIE UNIVERSITY
HALIFAX, NOVA SCOTIA
9 SEPTEMBER, 1994

ISBN 0-315-98890-8

Canada

Name JIANGNAN LI

Dissertation Abstracts International is arranged by broad, general subject categories. Please select the one subject which most nearly describes the content of your dissertation. Enter the corresponding four-digit code in the spaces provided.

Atmospheric Science

SUBJECT TERM

0 0 0 8

SUBJECT CODE

U·M·I

Subject Categories

THE HUMANITIES AND SOCIAL SCIENCES

COMMUNICATIONS AND THE ARTS

Architecture 0729
Art History 0377
Cinema 0900
Dance 0378
Fine Arts 0357
Information Science 0723
Journalism 0391
Library Science 0399
Mass Communications 0708
Music 0413
Speech Communication 0459
Theater 0465

EDUCATION

General 0515
Administration 0514
Adult and Continuing 0516
Agricultural 0517
Art 0273
Bilingual and Multicultural 0282
Business 0688
Community College 0275
Curriculum and Instruction 0727
Early Childhood 0518
Elementary 0524
Finance 0277
Guidance and Counseling 0519
Health 0680
Higher 0745
History of 0520
Home Economics 0278
Industrial 0521
Language and Literature 0279
Mathematics 0280
Music 0522
Philosophy of 0998
Physical 0523
Psychology 0525
Reading 0535
Religious 0527
Sciences 0714
Secondary 0533
Social Sciences 0534
Sociology of 0340
Special 0529
Teacher Training 0530
Technology 0710
Tests and Measurements 0288
Vocational 0747

LANGUAGE, LITERATURE AND LINGUISTICS

Language
- General 0679
- Ancient 0289
- Linguistics 0290
- Modern 0291

Literature
- General 0401
- Classical 0294
- Comparative 0295
- Medieval 0297
- Modern 0298
- African 0316
- American 0591
- Asian 0305
- Canadian (English) 0352
- Canadian (French) 0355
- English 0593
- Germanic 0311
- Latin American 0312
- Middle Eastern 0315
- Romance 0313
- Slavic and East European 0314

PHILOSOPHY, RELIGION AND THEOLOGY

Philosophy 0422
Religion
- General 0318
- Biblical Studies 0321
- Clergy 0319
- History of 0320
- Philosophy of 0322

Theology 0469

SOCIAL SCIENCES

American Studies 0323
Anthropology
- Archaeology 0324
- Cultural 0326
- Physical 0327

Business Administration
- General 0310
- Accounting 0272
- Banking 0770
- Management 0454
- Marketing 0338

Canadian Studies 0385
Economics
- General 0501
- Agricultural 0503
- Commerce-Business 0505
- Finance 0508
- History 0509
- Labor 0510
- Theory 0511

Folklore 0358
Geography 0366
Gerontology 0351
History
- General 0578
- Ancient 0579
- Medieval 0581
- Modern 0582
- Black 0328
- African 0331
- Asia, Australia and Oceania 0332
- Canadian 0334
- European 0335
- Latin American 0336
- Middle Eastern 0333
- United States 0337

History of Science 0585
Law 0398
Political Science
- General 0615
- International Law and Relations 0616
- Public Administration 0617

Recreation 0814
Social Work 0452
Sociology
- General 0626
- Criminology and Penology 0627
- Demography 0938
- Ethnic and Racial Studies 0631
- Individual and Family Studies 0628
- Industrial and Labor Relations 0629
- Public and Social Welfare 0630
- Social Structure and Development 0700
- Theory and Methods 0344

Transportation 0709
Urban and Regional Planning 0999
Women's Studies 0453

THE SCIENCES AND ENGINEERING

BIOLOGICAL SCIENCES

Agriculture
- General 0473
- Agronomy 0285
- Animal Culture and Nutrition 0475
- Animal Pathology 0476
- Food Science and Technology 0359
- Forestry and Wildlife 0478
- Plant Culture 0479
- Plant Pathology 0480
- Plant Physiology 0817
- Range Management 0777
- Wood Technology 0746

Biology
- General 0306
- Anatomy 0287
- Biostatistics 0308
- Botany 0309
- Cell 0379
- Ecology 0329
- Entomology 0353
- Genetics 0369
- Limnology 0793
- Microbiology 0410
- Molecular 0307
- Neuroscience 0317
- Oceanography 0416
- Physiology 0433
- Radiation 0821
- Veterinary Science 0778
- Zoology 0472

Biophysics
- General 0786
- Medical 0760

EARTH SCIENCES

Biogeochemistry 0425
Geochemistry 0996
Geodesy 0370
Geology 0372
Geophysics 0373
Hydrology 0388
Mineralogy 0411
Paleobotany 0345
Paleoecology 0426
Paleontology 0418
Paleozoology 0985
Palynology 0427
Physical Geography 0368
Physical Oceanography 0415

HEALTH AND ENVIRONMENTAL SCIENCES

Environmental Sciences 0768
Health Sciences
- General 0566
- Audiology 0300
- Chemotherapy 0992
- Dentistry 0567
- Education 0350
- Hospital Management 0769
- Human Development 0758
- Immunology 0982
- Medicine and Surgery 0564
- Mental Health 0347
- Nursing 0569
- Nutrition 0570
- Obstetrics and Gynecology 0380
- Occupational Health and Therapy 0354
- Ophthalmology 0381
- Pathology 0571
- Pharmacology 0419
- Pharmacy 0572
- Physical Therapy 0382
- Public Health 0573
- Radiology 0574
- Recreation 0575
- Speech Pathology 0460
- Toxicology 0383

Home Economics 0386

PHYSICAL SCIENCES

Pure Sciences

Chemistry
- General 0485
- Agricultural 0749
- Analytical 0486
- Biochemistry 0487
- Inorganic 0488
- Nuclear 0738
- Organic 0490
- Pharmaceutical 0491
- Physical 0494
- Polymer 0495
- Radiation 0754

Mathematics 0405
Physics
- General 0605
- Acoustics 0986
- Astronomy and Astrophysics 0606
- Atmospheric Science 0608
- Atomic 0748
- Electronics and Electricity 0607
- Elementary Particles and High Energy 0798
- Fluid and Plasma 0759
- Molecular 0609
- Nuclear 0610
- Optics 0752
- Radiation 0756
- Solid State 0611

Statistics 0463

Applied Sciences

Applied Mechanics 0346
Computer Science 0984
Engineering
- General 0537
- Aerospace 0538
- Agricultural 0539
- Automotive 0540
- Biomedical 0541
- Chemical 0542
- Civil 0543
- Electronics and Electrical 0544
- Heat and Thermodynamics 0348
- Hydraulic 0545
- Industrial 0546
- Marine 0547
- Materials Science 0794
- Mechanical 0548
- Metallurgy 0743
- Mining 0551
- Nuclear 0552
- Packaging 0549
- Petroleum 0765
- Sanitary and Municipal 0554
- System Science 0790

Geotechnology 0428
Operations Research 0796
Plastics Technology 0795
Textile Technology 0994

PSYCHOLOGY

General 0621
Behavioral 0384
Clinical 0622
Developmental 0620
Experimental 0623
Industrial 0624
Personality 0625
Physiological 0989
Psychobiology 0349
Psychometrics 0632
Social 0451

Contents

Table of Contents iv

List of Tables vii

List of Figures viii

Abstract xii

List of symbols xiii

Acknowledgments xvii

1 Introduction 1

1.1 Background 1

1.2 Purpose and outline of study 3

2 Solar Radiative Transfer In Clouds With Vertical Internal Inhomogeneity 5

2.1 Vertical profiles of LWC and r_e in stratocumulus clouds 6

2.2 Monte Carlo models 7

2.2.1 Physical principle of Monte Carlo simulations 9

2.2.2 Monte Carlo Cloud model with internal variation of optical properties 10

2.2.3 Error analysis of Monte Carlo models 14

2.3 Photon transport in vertically internally inhomogeneous clouds 16
2.3.1 Overcast cloud field with vertical inhomogeneity 16
2.3.2 Broken cloud field with vertical internal inhomogeneity 21
2.3.3 Cloud absorption 26
2.3.4 Effective cloud amount for cloud absorption 28
2.4 Summary 35

3 Perturbation Solution For 3-D Radiative Transfer In A Horizontally Periodic Inhomogeneous Cloud Field 36
3.1 The lowest order solution for plane parallel case 38
3.2 Perturbation solution 40
3.3 Results and discussions 45
3.3.1 The distribution of the radiance field 47
3.3.2 Shift phenomenon 54
3.3.3 Distribution of cloud heating rate 62
3.4 Summary 64

4 Second Order Perturbation Solution for Radiative Transfer in Clouds with a Horizontally Arbitrary Periodic Inhomogeneity 67
4.1 Perturbation solution for multi-mode case 68
4.2 Numerical results and discussions 73
4.3 Summary 84

5 Distributions of Irradiance, Monte Carlo Simulations 86
5.1 The limitations of Monte Carlo simulations 86
5.2 Horizontal distribution of irradiance 88
5.3 The anomalous distribution in reflectance for a cloud field with geometric structure variation 92
5.4 Again, on the cloud absorption anomaly 94
5.5 Summary 97

6 Conclusions and Outlook for Further Work 98

Appendix A 101

Appendix B 104

Bibliography 105

List of Tables

2.1 Coefficients in Eqs. (2.14), (2.15) and (2.16) according to the parameterization of Slingo (1989)). Although the significance of all given decimal places is doubtful, a discussion of error bars is not given in this reference. 14

List of Figures

2.1 (a) and (b) the vertical profiles of LWC and droplet cross section area for water clouds of A18 and M29 obtained from aircraft observations (after Noonkester(1984)), (c) the vertical profiles of corresponding r_e. 8

2.2 Vertical profiles of the single scattering properties of the cloud A18. The curves of single scattering albedo for band 1 and band 2 are both very close to one. 13

2.3 Normalized upward flux at the top of A18 cloud for number of photon N=10^4, 10^5 and 10^6, respectively, for 51 different seeds in random number initialization. 15

2.4 Standard deviation (solid line) for normalized upward flux calculated from Eqs.(2.22) and (2.23) for five different values of total photon numbers, compared to $1/N^{1/2}$ dependence (dotted line). 17

2.5 Vertical Reflectances for overcast clouds with different surface albedos. A18 is the real cloud, and <A18> is the vertically averaged counterpart. 20

2.6 Reflectances of the regular array cloud field for different distance ratios. 22

2.7 Reflectances of an "aged" cloud ($\overline{A18}$) with an inverse variation of internal optical quantities of A18 and its vertical averaged counterpart. 25

2.8 Cloud absorptance for different distance ratios. 27

2.9 Cloud absorptance for different cloud amounts, aspect ratio $a = 1$. . . 29

2.10 Cloud absorptance for different cloud amounts, aspect ratio $a = 0.2$. . 30

2.11 Ratios of effective cloud amounts to cloud amounts and corresponding WW parametrizations. 33
2.12 Reflectances and absorptance for the cloud M29 with different distance ratios. 34

3.1 The maximum limit value of the direct solar irradiance (dotted line) and its expansion approximation (solid line) as functions of the geometric path length. The irradiance is normalized with respect to πF_0. 42
3.2 Two dimensional distribution of the scaled extinction coefficient in a periodic region with the periodic length L. $k_0 = 50\,km^{-1}$, $g = 0.86$ and $\omega = 0.999$. 48
3.3 Two dimensional distributions of upwelling intensities with different periodic lengths: (a) $L = 1000\,m$, (b) $L = 600\,m$, (c) $L = 200\,m$. Solar zenith angle $\theta_0 = 0°$. The intensity unit is normalized with respect to $\mu_0 F_0$. 49
3.4 One dimensional distributions of the upwelling intensities on the line ($y = 0$) at different heights. (a) $L = 200\,m$; (b) $L = 1000\,m$. Solar zenith angle $\theta_0 = 0°$. The intensities are normalized with respect to $\mu_0 F_0$. 51
3.5 The relative fluctuation as a function of: (a) periodic length L, (b) cloud depth z_0, (c) extinction coefficient k_0. $g = 0.86$ and $\omega = 0.999$. Solar zenith angle $\theta_0 = 0°$. 53
3.6 Two dimensional distributions of upwelling intensities with different periodic lengths: (a) $L = 1000\,m$, (b) $L = 600\,m$, (c) $L = 200\,m$. Solar zenith angle $\theta_0 = 60°$. The intensity unit is normalized with respect to $\mu_0 F_0$. 55
3.7 One dimensional distributions of upwelling intensities on the line ($y = 0$) with different solar zenith angles. The intensities are normalized with respect to $\mu_0 F_0$. 56

3.8 One dimensional distributions of vertical direct solar flux on the line ($y = 0$) at different heights. Solar zenith angle $\theta_0 = 60°$. $\pi F_0 = 340\,W\,m^{-2}$. 58

3.9 Upwelling intensities on the line ($y = 0$) with different asymmetry factors. Cloud thickness $z_0 = 500\,m$. Solar zenith angle $\theta_0 = 60°$. The intensities are normalized with respect to $\mu_0 F_0$. 60

3.10 Downwelling intensities on the line ($y = 0$) with different asymmetry factors. Cloud thickness $z_0 = 120\,m$. Solar zenith angle $\theta_0 = 60°$. The intensities are normalized with respect to $\mu_0 F_0$. 61

3.11 Upwelling intensities on the line ($y = 0$) with different single scattering albedos. Solar zenith angle $\theta_0 = 60°$. The intensities are normalized with respect to $\mu_0 F_0$. 63

3.12 One dimensional distributions of heating rates on the line ($y = 0$) at different heights. $\pi F_0 = 340\,W\,m^{-2}$. (a) Solar zenith angle $\theta_0 = 60°$; (b) $\theta_0 = 45°$. 65

4.1 Two dimensional distributions of the upwelling intensities. In (a) and (b), the perturbation correction is up to the first order. In (c) and (d), the perturbation correction is up to the second order. Cloud depth 500m. Solar zenith angle $\theta_0 = 0^0$ in (a) and (c), and $\theta_0 = 60^0, \varphi_0 = 0^0$ in (b) and (d). The intensities are normalized with respect to $\mu_0 F_0$. . 74

4.2 The relative change of cloud albedo as a function of: (a) cloud depth z_0, (b) cloud horizontal periodic length L. Solar zenith angle $\theta_0 = 0^0$. 76

4.3 The relative change of cloud albedo as a function of: (a) extinction coefficient k_0 ($g = 0.86, \omega = 0.999$), (b) asymmetry factor g ($k_0 = 50\,km^{-1}, \omega = 0.999$), (c) single scattering albedo ω ($k_0 = 50\,km^{-1}, g = 0.86$). Solar zenith angle $\theta_0 = 0^0$. 78

4.4 One dimensional distributions of extinction coefficient in one periodic region (solid line), and the 16 mode Fourier series fits (dashed line). In the y direction the distribution is homogeneous. 79

4.5 One dimensional distributions of upward fluxes corresponding to the distribution of extinction coefficient in Fig.4.4(a). Solar zenith angle $\theta_0 = 0^0$. The fluxes are normalized with respect to $\mu_0 \pi F_0$. 81
4.6 Same as that in Fig.4.5, with $\theta_0 = 60^0, \varphi_0 = 0^0$. 83
4.7 One dimensional distributions of upward fluxes corresponding to the distribution of extinction coefficient in Fig.4.4(b). Solar zenith angle $\theta_0 = 0^0$. The fluxes are normalized with respect to $\mu_0 \pi F_0$. 85

5.1 Two dimensional distributions of the upward irradiance $F^{\uparrow}$ at different periodic lengths. (a) $L = 200\,m$; (b) $L = 1000\,m$. Solar zenith angle $\theta_0 = 0°$. The optical parameters $k_0 = 0.05\,m^{-1}$, $g = 0.86$, and $\omega = 0.999$. Cloud depth $z_0 = 500\,m$. The irradiances are normalized with respect to $\mu_0 \pi F_0$. 89
5.2 One-dimensional distributions of the upward irradiance. The g and ω vary with the change of k (solid line) or constant equal to the averaged values (dashed line). Solar zenith angle $\theta_0 = 0°$. The irradiances are normalized with respect to $\mu_0 \pi F_0$. 91
5.3 Two dimensional distributions of the upward irradiance $F^{\uparrow}$ for cloud field with height variation of Eq.(3). (a) $L = 200\,m$; (b) $L = 2000\,m$. Solar zenith angle $\theta_0 = 0°$. The cloud is internally homogeneous with optical parameters $k = 0.05\,m^{-1}$, $g = 0.86$, and $\omega = 0.999$. Unperturbed cloud depth $z_0 = 500\,m$. The irradiances are normalized with respect to $\mu_0 \pi F_0$. 93
5.4 Cloud absorption for cloud A18 and its vertical averaged counterpart <A18>. Also cloud absorption for A18 with top cosinusoidal variation of different periodic lengths. 96

Abstract

In order to investigate the photon transport in inhomogeneous clouds, a Monte Carlo cloud model with internal variation of optical properties is developed. The data for cloud vertical internal inhomogeneity are chosen from published observations. Parameterization of the solar radiative properties of clouds is used in the form of the liquid water content and the effective radius of cloud droplet. The Monte Carlo simulations show that for overcast stratocumulus clouds, the differences in reflectance between the vertical inhomogeneous clouds and their plane-parallel counterpart are very small (only about 1%). These differences can be enhanced up to 10% for large solar zenith angles, when the overcast clouds are separated into broken cloud fields. If the cloud coverage is large, the vertical inhomogeneity of clouds can cause about 7% increase in cloud absorption, which may help to explain the cloud absorption anomaly. Also, the parameterization of effective cloud amount for cloud absorption is discussed.

For a vertical homogeneous plane-parallel layer with horizontal cosinusoidal periodic variations of the extinction coefficient, the first order perturbation solution of the three dimensional radiative transfer equation has been obtained. There exists a correspondence between the distribution of the extinction coefficient and the distribution of the upwelling intensity. However, under certain conditions, the distribution of the upwelling intensity is opposite to the distribution of the extinction coefficient. If the solar zenith angle is large, shifts in the configurations of the distribution of the upwelling intensity may appear. The single scattering parameters can influence the distribution of the diffuse radiative intensity. The distribution of the heating rate inside the cloud and the distribution of the extinction coefficient are nearly coincident with each other.

The perturbation solution can be extended to second order multi-mode case. The calculations show that the perturbation solution series is convergent. The cloud albedo changes from the unperturbed value when the second order perturbation correction is applied. The change of albedo can be negative as well as positive. The albedo changes due to the geometric factors and scattering factors are discussed. Also, the radiative transfer in a medium with an internal variation other than the cosinusoidal type is investigated.

Monte Carlo simulation is used again to investigate the horizontal irradiance distribution in clouds, to verify the results of the analytical solution. Also the impact of geometric variation to the distribution of irradiance has been discussed.

List of symbols

a - aspect ratio

A - cross sectional area

$Abs_{pp}(100\%)$ - absorption for plane-parallel cloud

$Abs_{pp}(N)$ - absorption for plane-parallel cloud with cloud amount N

α - cloud albedo

$\Delta\alpha$ - change of cloud albedo

c_p - specific heat

D - side length of cubic cloud

ϵ - perturbation coefficient

F_0 - incident solar irradiance divided by π

$F^{\uparrow}$ - upward flux

$F^{\downarrow}$ - downward flux

$\mathbf{F}$ - net diffuse solar irradiance vector

$\mathbf{F}^d$ - net direct solar irradiance vector

g - asymmetry factor

g' - scaled asymmetry factor

$\bar{g}$ - vertical averaged asymmetry factor

g_i - asymmetry factor for band i

H - height of cubic cloud

I - radiative intensity (radiance)

I_0^0 - first term of the Eddington intensity expansion for plane-parallel cloud

I_x^0 - x component of the Eddington intensity expansion for plane-parallel cloud

I_y^0 - y component of the Eddington intensity expansion for plane-parallel cloud

I_z^0 - z component of the Eddington intensity expansion for plane-parallel cloud

I_0^1 - first term of the Eddington intensity expansion for the first order of perturbation

I_x^1 - x component of the Eddington intensity expansion for the first order of perturbation

I_y^1 - y component of the Eddington intensity expansion for the first order of perturbation

I_z^1 - z component of the Eddington intensity expansion for the first order of perturbation

I_0^2 - first term of the Eddington intensity expansion for the second order of perturbation

I_x^2 - x component of the Eddington intensity expansion for the second order of perturbation

I_y^2 - y component of the Eddington intensity expansion for the second order of perturbation

I_z^2 - z component of the Eddington intensity expansion for the second order of perturbation

J - internal source term from multiple scattering

J_0 - external solar source term

k - extinction coefficient

k' - scaled extinction coefficient

k_0 - unperturbed extinction coefficient

$\bar{k}$ - vertical averaged extinction coefficient

LWC - liquid water content

LWP - liquid water path

μ - cosine of local polar angle

μ_0 - cosine of solar zenith angle

ν - sine of local polar angle

ν_0 - sine of solar zenith angle

N - cloud amount

N_e - effective cloud amount

$N_{e\,A18}$ - effective cloud amount for cloud A18

$N_{e\,<A18>}$ - effective cloud amount for cloud <A18>

ω - single scattering albedo

ω' - scaled single scattering albedo

$\bar{\omega}$ - vertical averaged single scattering albedo

ω_i - single scattering albedo for band i

P - relative fluctuation

$\mathrm{P}(\mu)$ - scattering phase function

r_e - effective radius

R - distance ratio

ρ - air density

σ - standard deviation

τ - optical depth

S - distance between two neighbouring cubic cloud centers

τ_i - optical depth for band i

W - liquid water content

Acknowledgments

I would like to thank my supervisors Petr Chýlek and D. J. W. Geldart for their enthusiasm, critical suggestions and support.

I am grateful to the members of my committee, H. J. Kreuzer and W. T. Hyde, for their interest in my work and helpful suggestions. I also appreciate O. Hertzman for his help.

Discussions with the students in the atmospheric science group, especially with B. Crenna, P. Damiano, S. Dobbie and J. Wong, were instrumental in the development of this work.

Thanks go to Dr. H. W. Barker for making his Monte Carlo program available to our group.

Finally I wish to thank the Atmospheric Environment Service and Natural Science and Engineering Research Council of Canada, the Killam Foundation at Dalhousie University, NCAR/C4 and the American Meteorological Society for scholarship support.

Chapter 1

Introduction

1.1 Background

Climatic change and stability are intimately related to the Earth's radiation budget, which itself is strongly influenced by clouds. In turn, clouds are governed by the Earth's radiation budget and thus by climate. For example, simple energy balance conservations imply that 5% change in cloud amount will result in an estimated change around of 2 degrees in the surface temperature. The potential importance of this feedback has initiated a large research effort to understand the cloud-radiation interaction. Clouds are one of the most crucial and least understood components of the climate system. The basic lack of understanding stems from our inability both to realistically describe the various life cycle processes of clouds and to effectively determine the radiative properties of realistic clouds. A process that is likely to play a central role in the evolution of clouds and cloud systems is the interaction of radiation with the atmospheric environment both in and around clouds. This interaction depends on the cloud geometric structure and cloud internal optical properties, which are highly nonlinear. However, in present climate models the plane-parallel approximation is generally used. Plane-parallel clouds are idealized flat, homogeneous slabs of infinite horizontal extent. The finite cloud geometry and cloud internal inhomogeneity are generally ignored. Such simple cloud models can hardly describe correctly

the cloud-radiation interaction. Therefore efforts are being made to improve radiative transfer methods to account for clouds with more realistic forms..

One approach to the problem is to simulate photon transport in cloud fields using the Monte Carlo model. In early work, Monte Carlo simulation was used to examine photon transport in homogeneous isolated clouds of definite shapes (Busygin *et al.*, 1973; McKee and Cox, 1974; Davies, 1978). The large scale cloud fields were simplified to be regular arrays, in which all clouds are of the same shape and the distance between any two neighbouring cloud centers is the same. The importance of cloud shape and cloud field arrangement for radiative transfer process has been investigated by several groups (Busygin *et al.*, 1973; Aida, 1973; Welch and Wielicki, 1984). Kobayashi (1988) extended the regular array field to a cloud field composed of various sizes of clouds in a random distribution. Recently, Barker and Davies (1992) studied solar radiative transfer in a realistic broken cloud field with a scaling power law, motivated by observations showing that a cloud field on mesoscopic scale exhibits "scaling" or spatial autocorrelation structure (Cahalan and Snider, 1989).

A number of works have focused on the parameterization of Monte Carlo calculation results (Harshvardhan and Weinman, 1982; Weinman and Harshvardhan, 1982; Harshvardhan and Thomas, 1984; Schmetz, 1984; Welch and Wielicki, 1985; Breon, 1992). In order to describe more accurately radiative transfer processes in climate models by incorporating the Monte Carlo simulation findings, a successful parameterization is necessary, since a direct Monte Carlo simulation is not practical in climate models.

Realistic photon transport processes are simulated in Monte Carlo methods and computation of irradiance is fairly easy for any specified cloud geometry. However, since the number density of incoming photons (number per square meter) used in Monte Carlo simulations is much smaller than that of the real solar beam, the distribution of radiance is hard to be obtained using a Monte Carlo method. Also, the Monte Carlo simulation requires an excessive computer time.

Another approach to the radiative transfer problem is to solve the multi-dimensional radiative transfer equation. Davies (1978), Brandley (1981), Preisendorfer and Stephens (1984), and Stephens and Preisendorfer (1984) have derived solutions that describe the radiance fields of an isolated homogeneous cuboidal cloud. For more complicated geometric cloud shapes, such a method is generally not applicable.

For both of the above approaches, the study of radiative transfer has been mostly restricted to the effect of cloud geometry with the cloud still taken as internally homogeneous. However, in addition to having complicated geometric structures, clouds generally have internal inhomogeneity. For example, in cumulus clouds the liquid water content (LWC) and the effective radius increase with height. Such an increase of LWC with height is not observed in cirrus clouds. Horizontally the clouds are also inhomogeneous; the central core regions (updraft regions) in cumulus cloud have larger LWC and the boundary regions (downdraft regions) have smaller LWC. The impact of the internal inhomogeneity on the radiative transfer process has seldom been investigated either by Monte Carlo simulation or by any analytical method.

Recently Kabayashi (1991) and Evans (1993) have considered photon transport in internally inhomogeneous clouds using a numerical model (space grid method). Just as in the Monte Carlo simulations, such numerical models are generally very time consuming. However, since the direct solar beam term has been treated very approximately in their works, these works did not observe all of the physical phenomena shown in the following chapters.

1.2 Purpose and outline of study

The purpose of this thesis is to explore the impact of the cloud internal inhomogeneity on the radiative transfer process in clouds and our attention has been concentrated on this cloud internal inhomogeneity. An analytical method for solving the three dimensional radiative transfer equation and the Monte Carlo simulation method are both used in the study.

In the second chapter the cloud internal vertical inhomogeneity is investigated. In order to deal with the cloud internal variations, we develop a new Monte Carlo simulation scheme in which the cloud internal optical properties can be taken into account. There exist observations of the vertical variation of the LWC and droplet effective radius and all the observations show that the vertical variation of LWC is quite similar for cumulus (stratocumulus) clouds. Therefore, in calculations we can take the cloud vertical variation from observations and use a parameterization to obtain the internal optical properties from the observed liquid water content (LWC) and effective radius. Flat clouds and broken clouds are investigated. Cloud absorption was seldom considered before in Monte Carlo models, but cloud absorption is an important aspect in our study.

We find that an analytical solution can be obtained for radiative transfer in a medium with internal inhomogeneity using a perturbation method. In chapter 3, the first order perturbation solution of radiative transfer in a cloud with internal cosinusoidal periodic variation is obtained. The distribution of the upwelling intensity and cloud internal heating rate are discussed.

In chapter 4, the analytical solution is extended to the multi-mode case and to second order perturbation expansion. An arbitrary form of cloud internal inhomogeneity can then be investigated. When the second order perturbation is considered, a change in cloud albedo results due to inhomogeneity, which will be extensively studied in that chapter.

The Monte Carlo simulation is used again in chapter 5 to explore radiative transfer in clouds with internal horizontal variation. One purpose of this study is to verify numerically results obtained in chapter 3 and 4.

Physical explanations for the phenomena explored are always emphasized in following chapters.

Chapter 2

Solar Radiative Transfer In Clouds With Vertical Internal Inhomogeneity

In the last twenty years Monte Carlo simulation of solar photon transport in cloud fields has been extensively investigated. Although most of the reported Monte Carlo simulation works have improved on the plane-parallel assumption by considering cloud (cloud field) geometry structures, the improvements are more qualitative than quantitative. In most of these Monte Carlo simulations, the attention has only been paid to cloud geometry. The internal variations of cloud optical properties have not been considered and the clouds are taken as internally homogeneous.

It is established from observations that a cumulus (stratocumulus) cloud is inhomogeneous in both horizontal and vertical directions (Mason, 1971; Paltridge, 1974; Platt, 1976; Slingo *et al.*, 1982a; Slingo *et al.*, 1982b; Noonkester, 1984). For instance, inside a cumulus (stratocumulus) cloud the liquid water content (LWC) and the cloud droplet size distribution vary with height (Mason, 1971), which leads to the single scattering properties of cloud droplets being variable in the vertical direction. Therefore, the radiative transfer in a cloud would be influenced by the cloud inhomogeneity.

To what degree can the inhomogeneity of clouds affect the Monte Carlo simulation of radiative transfer in broken clouds? By consideration of the vertical internal inhomogeneity, will the cloud albedo difference between a broken cloud and its plane-parallel counterpart be enhanced or reduced? What is the influence on the cloud solar absorption? These questions are important for both the study of radiative transfer in the realistic cloud field itself and the parameterization of Monte Carlo results in climate modeling.

In order to study the internal inhomogeneity of clouds, the spatial variation of cloud optical properties has to be considered in a Monte Carlo cloud model. In this model the length scales of homogeneous cells constituting a cloud will be taken to be small, close to the mean free path of photons in the cloud. Consequently on average, a photon will scatter only once as it passes through each cell. The spatial variation is taken into account properly in the photon transport process. In this chapter, the cloud vertical internal inhomogeneity will be investigated first.

2.1 Vertical profiles of LWC and r_e in stratocumulus clouds

In the last 40 years, there have been a lot of aircraft observations of the droplet distribution in cumulus (stratocumulus) clouds (Mason, 1971; Paltridge, 1974; Platt, 1976; Slingo *et al.*, 1982a; Slingo *et al.*, 1982b; Noonkester, 1984). All the observational results showed that inside a cumulus (stratocumulus) cloud, the LWC and the droplet radius increase with height above the cloud base. This phenomenon is attributed to the water vapor condensation process.

In the following, we use the observational results of Noonkester (1984). In his observations, besides the vertical profile of LWC, the vertical distribution of cross sectional areas of droplets are also presented. Fig.2.1a and 2.1b show the profiles of LWC and cross sectional area of the droplet in stratocumulus clouds measured for actual marine clouds. The two curves represent the two aircraft observational

results of August 18 (A18) and May 29 (M29) near San Diego in 1981. The droplet spectrometer probes are used in measurements. The vertical profiles of LWC and cross sectional area are calculated from droplet spectrum in different height. The clouds of A18 and M29 are pure water clouds.

From the cloud base to the positions near the cloud top (200 m on A18, 280 m on M29), the LWC increases almost linearly. Noonkester gave the approximate formulae for the vertical variations of LWC in these regions from the observation results

$$\text{A18}: \qquad \mathrm{W} = 0.0074 + 0.0016z \ (g\ m^{-3}) \ , \tag{2.1}$$

$$\text{M29}: \qquad \mathrm{W} = 0.019 + 0.0012z \ (g\ m^{-3}) \ , \tag{2.2}$$

where z is the height in meters from the cloud base. Noonkester also presented the approximate formulae for droplet cross sectional areas in these regions,

$$\text{A18}: \qquad \mathrm{A} = 54 + 1.9z \ (cm^{-2}m^{-3}) \tag{2.3}$$

$$\text{M29}: \qquad \mathrm{A} = 50 + 1.3z \ (cm^{-2}m^{-3}) \tag{2.4}$$

Above these linear regions to the tops of clouds, LWC increases slowly (on M29) or decreases (on A18), which is due to the turret structures in the top of stratocumulus clouds. Above a cloud top the LWC decreases sharply.

The cloud effective radius can be obtained by given liquid water content and droplet cross section

$$r_e = \frac{3}{4\rho}\frac{\mathrm{W}}{\mathrm{A}}\, 10^{10}(\mu m) \ , \tag{2.5}$$

where $\rho(g\, m^{-3})$ is the liquid water density. Fig.1 (c) shows the vertical profiles of r_e for clouds of A18 and M29. In radiative transfer processes, the LWC and r_e are the most important integrated quantities derived from the micro-physical structure of clouds, since LWC and r_e are associated with the cloud internal optical properties.

2.2 Monte Carlo models

We consider the Monte Carlo method because the solutions of the radiative transfer equation in non-planar inhomogeneous clouds through analytical methods are very

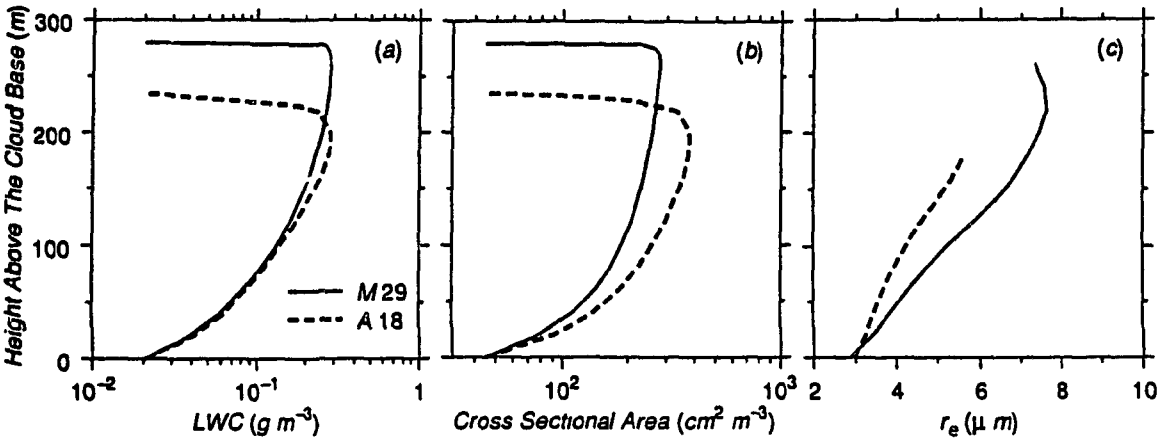

Figure 2.1: (a) and (b) the vertical profiles of LWC and droplet cross section area for clouds of A18 and M29 obtained from aircraft observations (after Noonkester(1984)), (c) the vertical profiles of corresponding r_e.

cumbersome and also limited in their applicability. The Monte Carlo simulation of photon transport offers a different quantitative approach for studying the radiative transfer process in realistic clouds. In Monte Carlo simulations, the irradiances can be computed fairly easily for general cloud shape and internal inhomogeneity.

2.2.1 Physical principle of Monte Carlo simulations

The fundamental blocks of the Monte Carlo model are homogeneous cubes filled with scattering and absorbing particles. All particles are assumed to be spherical cloud droplets. A cloud or cloud field is simulated by a chosen number of elemental cubes of geometric size l_x, l_y and l_z in x, y and z Cartesian coordinates. Each cube is assigned a volume extinction coefficient $k(l,m,n)$, where the l, m and n indices, specify the cell.

To establish the Monte Carlo algorithm, it is convenient to simulate the distance travelled by a photon between successive collisions. In accordance with Beer's law, the probability that a photon has travelled an optical pathlength τ between successive collisions is taken to be the fraction of radiation transmitted through that pathlength, that is

$$\Pr[\tau] = e^{-\tau} \tag{2.6}$$

Choose a random number RN$\in$(0,1) to represent Pr[τ] in Eq.(2.6). If in the process the photon has passed through N cells with optical depth τ' ($\tau' < \tau$),

$$\mathrm{RN} < e^{-\tau'} = \exp[-\sum_{j=1}^{\mathrm{N}} f_j [k(l,m,n)]_j] \tag{2.7}$$

where f_j and $[k(l,m,n)]_j$ are the geometric pathlength through and the associated extinction coefficient of the j^{th} cell traversed by the photon, respectively. The updated position of the photon is

$$\mathbf{x}_{\mathrm{N+1}} = \mathbf{x}_0 + \hat{\mathbf{s}} \sum_{j=1}^{\mathrm{N}} f_j \tag{2.8}$$

where $\mathbf{x}_0$ is the initial position of the photon and $\hat{\mathbf{s}}$ is the unit vector in the direction of the photon path.

Assume the residual pathlength which remains before scattering or absorption is

$$f_{res} = \frac{-\ln(\mathrm{RN}) - \sum_{j=1}^{\mathrm{N}} f_j[k(l,m,n)]_j}{[k(l,m,n)]_{\mathrm{N+1}}} \tag{2.9}$$

where $[k(l,m,n)]_{\mathrm{N+1}}$ is the extinction coefficient of the cell containing the photon. If the number of the cell containing $\mathbf{x}_{\mathrm{N+1}}$ equals the number of the cell containing

$$\mathbf{x} = \mathbf{x}_{\mathrm{N+1}} + \hat{\mathbf{s}} f_{res} \,, \tag{2.10}$$

there is a scattering or absorption event at $\mathbf{x}$ for the required optical pathlength has then been obtained. If this condition is not satisfied, then f_{res} is discarded and the updating process is again repeated.

If $\mathbf{x}_{\mathrm{N+1}}$ is within the correct cell, then either a scattering or absorption event takes place. Assume the single scattering albedo of droplet is ω. At each events, before the scattering angles are determined, a uniform random number RN$\in$(0,1) is generated. If RN$>\omega$ the photon is taken to be absorbed and its trajectory is terminated. If RN $<\omega$, a scattering event takes place.

When a scattering events occurs, the scattering angle, θ_s, is computed in the Monte Carlo code by solving

$$\mathrm{RN} = \frac{1}{2}\int_{\cos\theta_s}^{1} \mathrm{P}(\mu)\,\mathrm{d}\mu \,, \tag{2.11}$$

where $\mathrm{P}(\mu)$ is the phase function. For simplicity the Henyey-Greenstein phase function $\mathrm{P_{HG}}(\mu)$ is used. It is given as

$$\mathrm{P_{HG}}(\mu) = \frac{1-g^2}{[1+g^2-2g\mu]^{3/2}} \,, \tag{2.12}$$

where g is the asymmetry factor. By Eqs.(2.11) and (2.12) the scattering angle, θ_s, can be determined. The azimuthal angle of scattering is to be

$$\varphi_s = 2\pi(\mathrm{RN}) \,, \tag{2.13}$$

Once θ_s and φ_s are obtained then the new photon traverse direction is known.

2.2.2 Monte Carlo Cloud model with internal variation of optical properties

As we have pointed out, most of Monte Carlo models used so far have focused on cloud geometric shape and cloud field arrangement. The internal variations of cloud optical properties have not been considered. In these models the size of spatial cells in cloud fields generally has a length scale of about 1 km. If we take account of cloud internal inhomogeneity on the radiative transfer process, the spatial cells of clouds must be much smaller. The photon mean free path length in a typical stratocumulus cloud is about 20 m (for an extinction coefficient of 50 km^{-1}). Therefore, the spatial extent of cells in the cloud field should be chosen with a size length of about 20 m or less. In previous Monte Carlo models, the asymmetry factor and single scattering albedo have been taken to be constant for all cells. This must be improved in order to show the spatial correlation of the three optical parameters.

The Monte Carlo cloud models with cells of this size can be used in practical simulations of isolated clouds with internal variation of optical properties. The calculations can also be extended to an overcast cloud field (planar cloud with an infinite horizontal extent) or a cloud field with a regular array, since the computational requirements of such cloud fields can be much reduced by the cyclic boundary conditions. However, the mesoscale studies are not feasible in the present model, since at least 10^{10} spatial cells are needed to describe the mesoscale cloud field, and such sizes are too large.

The radiative transfer processes in a cloud are not directly associated with cloud LWC and r_e, but are related to the cloud droplet single scattering properties, which are the extinction coefficient, single scattering albedo and asymmetry factor. By a suitable parameterization of solar radiative properties of water cloud (Slingo, 1989), the relation between the LWC and r_e and the single scattering properties of cloud droplets are established.

We choose the 4 band parameterization scheme developed by Slingo (1989). For a given spectral interval i, the single scattering properties of cloud droplets are parameterized in terms of the liquid water path (LWP) and the effective radius of the

size distribution.

$$\tau_i = \mathrm{LWP}(a_i + \frac{b_i}{r_e}) \,, \tag{2.14}$$

$$\omega_i = 1 - c_i - d_i r_e \,, \tag{2.15}$$

$$g_i = e_i + f_i r_e \,, \tag{2.16}$$

where τ_i is the cloud optical path, ω_i is the single scattering albedo and g_i is the asymmetry factor. The LWP is defined as

$$\mathrm{LWP} = \int_{\text{cloud base}}^{\text{cloud top}} \mathrm{LWC}\; ds \tag{2.17}$$

where ds is the differential geometric length along the transfer path. The values of the coefficients in Eqs.(2.14), (2.15) and (2.16) are listed in Table 2.1. The 'weight' is the fraction of solar irradiance at the top of the atmosphere in each spectral band. In our calculations, the average single scattering properties are obtained for each band (using Slingo's parameterization) and one Monte Carlo simulation is performed for each spectral band.

In the Monte Carlo model, each cell is homogeneous in micro-physical quantities. We denote LWC and r_e for each cloud cell as $\mathrm{LWC}(l,m,n)$ and $r_e(l,m,n)$, where l, m and n are the cell numbers in the x, y and z direction, respectively. From this the optical path is

$$\tau_i = \sum k_i(l,m,n)\; s(l,m,n) \tag{2.18}$$

where the sum is over the cells along the optical path, $s(l,m,n)$ is the geometric path length through the cell (l,m,n) , and

$$k_i(l,m,n) = \mathrm{LWC}(l,m,n)(a_i + \frac{b_i}{r_e(l,m,n)}) \tag{2.19}$$

is the volume averaged extinction coefficient for the cell (l,m,n) . Similarly,

$$\omega_i(l,m,n) = 1 - c_i - d_i r_e(l,m,n) \,, \tag{2.20}$$

$$g_i(l,m,n) = e_i + f_i r_e(l,m,n) \tag{2.21}$$

i	(μm)	a_i ($10^{-2}m^2/g$)	b_i ($\mu m m^2/g$)	c_i	d_i (μm^{-1})	e_i	f_i ($10^{-3}/\mu m$)	weight
1	0.25-0.69	2.817	1.305	-5.62e-8	1.63e-7	0.829	2.482	0.459760
2	0.69-1.19	2.682	1.346	-6.94e-6	2.35e-5	0.794	4.226	0.326158
3	1.19-2.38	2.264	1.454	4.64e-4	1.24e-3	0.754	6.560	0.180608
4	2.38-4.00	1.281	1.641	2.01e-1	7.56e-3	0.826	4.353	0.033474

Table 2.1: Coefficients in Eqs. (2.14), (2.15) and (2.16) according to the parameterization of Slingo (1989)). Although the significance of all given decimal places is doubtful, a discussion of error bars is not given in this reference.

are the volume averaged single scattering albedo and asymmetry factor in cell (l, m, n).

The vertical distributions of k_i, ω_i and g_i for the cloud case of A18 are presented in Fig.2.2.

2.2.3 Error analysis of Monte Carlo models

The Monte Carlo simulation is based on statistical methods and a finite number of photons should lead to a quasi-random unbiased error in flux estimates. Here we use a simple method for estimating errors in Monte Carlo calculations of radiation flux. We consider a planar cloud type of A18 with internal inhomogeneity. The solar zenith angle is chosen to be 0°. Statistical fluctuations in the Monte Carlo simulations result from a change of the initial RN seed. In Fig.2.3, the upward flux at cloud top corresponds to the different RN initialization. The total number of photons used are different in Fig.2.3 a, b and c. The statistical fluctuations decrease with an increase in the number of photons used. We can obtain the standard deviation from

$$\sigma = [\frac{1}{\mathrm{M}-1}\sum_{k=1}^{\mathrm{M}}(p_k - \bar{p})^2]^{1/2}, \tag{2.22}$$

where M is the total number of calculations with different RN seed initialization, p_k is the flux corresponding to the k^{th} different RN seed initialization. The averaged value is

$$\bar{p} = \frac{1}{\mathrm{M}}\sum_{k=1}^{\mathrm{M}} p_k . \tag{2.23}$$

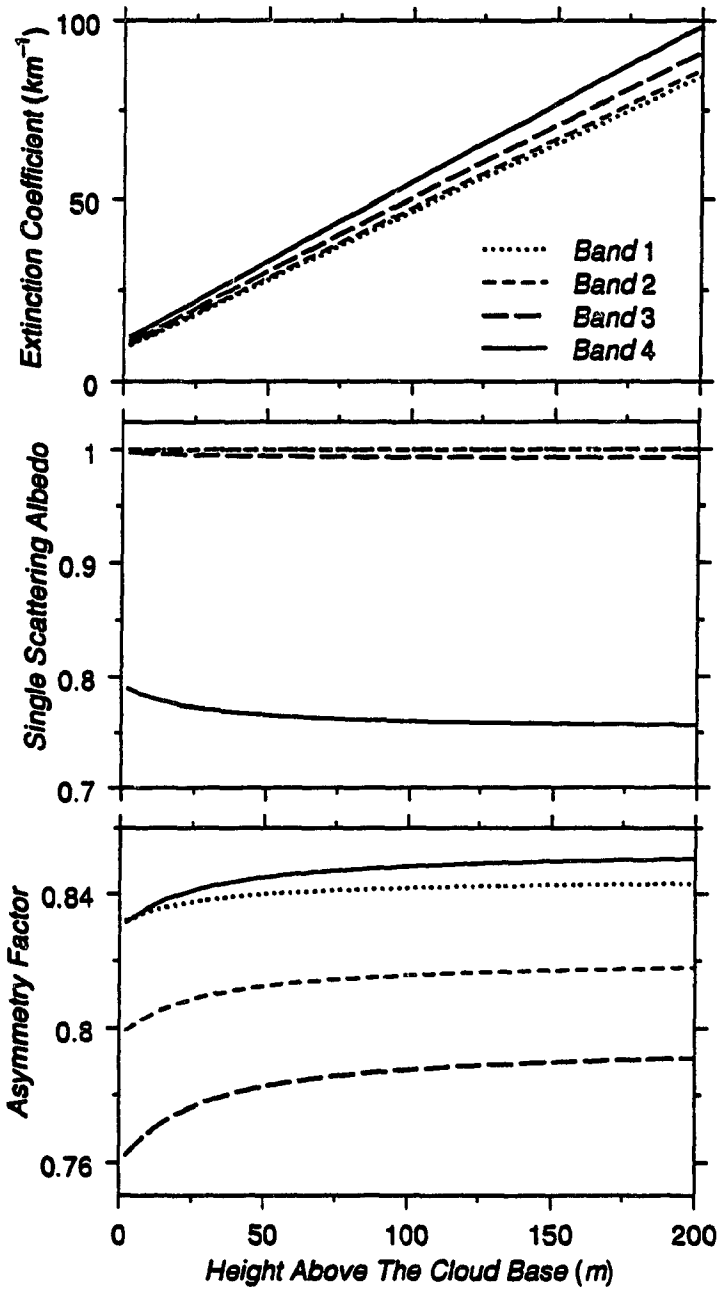

Figure 2.2: Vertical profiles of the single scattering properties of the cloud A18. The curves of single scattering albedo for band 1 and band 2 are both very close to one.

By Eq.(2.22) the standard deviations can be obtained for different numbers of total photon used, N. In Fig.2.4, the standard deviation is plotted versus $1/N^{1/2}$. We find that all the values of σ are under the dotted line. This shows that the standard deviation is smaller than the $1/N^{1/2}$. This is consistent with the theoretical expression of standard deviation,

$$\sigma = [\frac{\bar{p}(1-\bar{p})}{N}]^{1/2}. \tag{2.24}$$

Therefore, an upper bound on the standard deviation may be taken to be $1/N^{1/2}$ with reliability. In following Monte Carlo simulations in this chapter, 10^6 photons will be always used. Therefore, the standard deviation is smaller than 0.001.

2.3 Photon transport in vertically internally inhomogeneous clouds

We will take the cloud case of A18 in section 2 as an example to show the influences of the cloud vertical internal inhomogeneity on the radiative transfer in clouds. A18 is a typical stratocumulus cloud; its vertically averaged extinction coefficient is about 50 km^{-1} (McKee and Cox, 1974). The case of A18 is simple since the linear results of LWC and droplet cross section cover nearly all the vertical cloud region. The uppermost part of the cloud above the linear region is small, and can be ignored. We have pointed out that it is a common observational conclusion that the linear region can nearly cover the full cloud height except the cloud top turrets (Mason, 1971; Paltridge, 1974; Platt, 1976; Slingo *et al.*, 1982a; Slingo *et al.*, 1982b).

2.3.1 Overcast cloud field with vertical inhomogeneity

Radiative transfer is dependent on the cloud geometry effects as well as on the cloud single scattering variables (extinction coefficient, single scattering albedo and asymmetry factor). The extinction coefficient is the sum of the scattering coefficient and

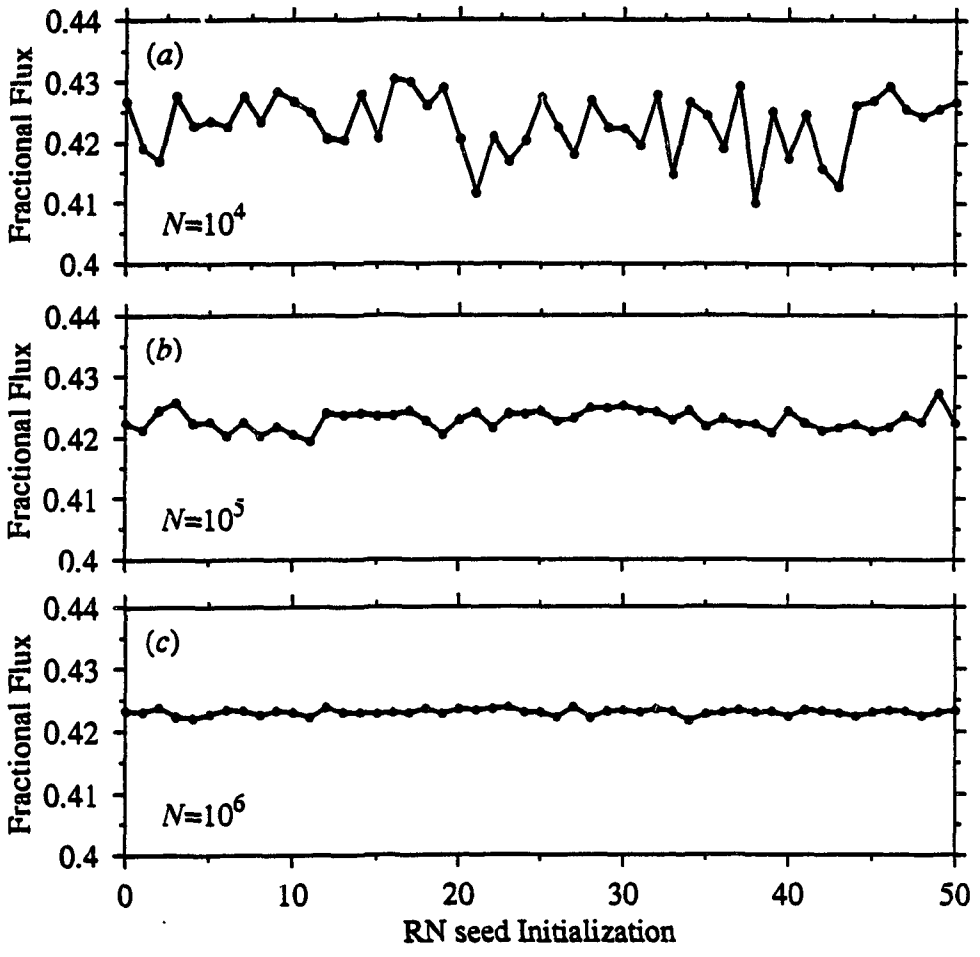

Figure 2.3: Normalized upward flux at the top of A18 cloud for number of photon N=10^4, 10^5 and 10^6, respectively, for 51 different seeds in random number initialization.

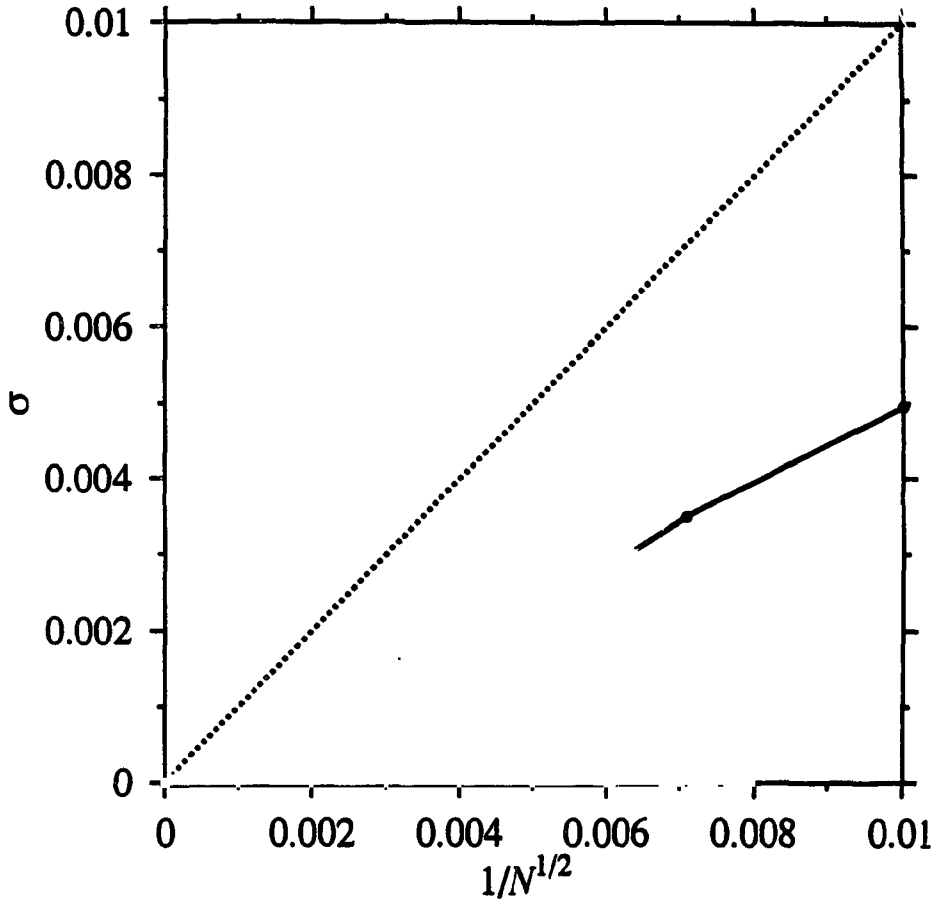

Figure 2.4: Standard deviation (solid line) for normalized upward flux calculated from Eqs.(2.22) and (2.23) for five different values of total photon numbers, compared to $1/N^{1/2}$ dependence (dotted line).

the absorption coefficient. The larger the extinction coefficient, the larger the probability that a photon is scattered or absorbed in the transport process. The single scattering albedo represents the probability of a photon not being absorbed when a scattering event occurs. The asymmetry factor represents a average forward component of the scattering flux.

From Fig.2.2, along the vertical direction inside the cloud (A18), the changes in the extinction coefficient are large for each spectral interval, but the changes of the single scattering albedos and asymmetry factors are relatively small. Especially for single scattering albedos, there is nearly no change for the first three bands. However, the radiative transfer process is very sensitive to the changes of ω and g. Let us consider a case of overcast cloud layer. Then the radiative transfer reduces to the one dimensional case. We keep ω and g constant in the whole vertical region, but let k vary with the height. This corresponds to the situation that all cloud droplets are of the same radius; the change of k is due to the spatial variation of the volume density of the cloud droplets. In this case the cloud reflectance is the same for taking k to have vertical variation or taking k as its vertically averaged value. If ω and g are constants, the cloud reflectance is determined by $\tau(z_0)$ only, where the total optical depth is

$$\tau(z_0) = -\int_0^{z_0} k(z')\, dz' \ , \tag{2.25}$$

and z_0 is the cloud vertical geometric depth. The results are only dependent on the total vertical optical depth of the cloud, not associated with the vertical variation of $k(z)$. Therefore, the result is the same as for replacing $k(z)$ by its vertically averaged value

$$\bar{k} = \int_0^{z_0} k(z')\, dz' \,/ z_0 \tag{2.26}$$

in all space. This can be verified by Monte Carlo simulations.

In a real cloud, the spatial variation of k is usually accompanied by spatial variation of g and ω. Therefore a change in cloud reflectance is expected. Let us take the real cloud A18 as an example. The reflectances of solar radiation for an overcast cloud (A18) with an infinite horizontal extent are shown in Fig.2.5. Two values of surface

albedos have been taken into account. The real cloud (A18) has vertical variations of single scattering properties as shown in Fig.2.2. Its counterpart (<A18>) corresponds to the plane-parallel case, with vertically averaged single scattering variables $\bar{k}$, $\bar{g}$, and $\bar{\omega}$. $\bar{k}$ is given in Eq.(2.26), while $\bar{\omega}$ and $\bar{g}$, are defined by

$$\bar{\omega} = \int_0^{z_0} \omega(z')\, dz' \,/ z_0 \,, \tag{2.27}$$

$$\bar{g} = \int_0^{z_0} g(z')\, dz' \,/ z_0 \,. \tag{2.28}$$

In Fig.2.5, we find that the inhomogeneous real cloud has a smaller solar reflectance in comparison with that of the homogeneous plane-parallel counterpart (relative reduction is about 1%). Though small, the differences in reflectance between the real cloud and its vertically averaged counterpart are larger than the standard deviation. The results in Fig.2.5 are consistent with the common belief that the cloud inhomogeneity leads to reduction in cloud reflectance (Stephens and Tsay, 1990). Although we are not aware of a rigorous proof, a physical explanation for the changes of solar reflectance can be given, taking into account the scattering properties.

For cloud A18, the extinction coefficient and the asymmetry factor increase with the height (above cloud base); the single scattering albedo decreases with height (Fig.2.2). Since the downward directed transport of solar photon number decreases exponentially inside the clouds, the larger extinction coefficient at the upper part of a cloud leads to more scattering events for the downward directed solar photons. The larger asymmetry factor in this region leads to the scattered photons having a larger tendency to go downward, thus contributing less to the reflectance. In addition, the smaller single scattering albedo in this region of more scattering events results in more photons being absorbed, which also reduces the cloud reflectance.

As mentioned above, for an overcast cloud, if we keep ω and g constant, the vertical variation of k does not make any difference for the cloud reflectance. Differences in reflectance only appear when the region of more scattering events has a larger asymmetry factor or a smaller single scattering albedo. These two processes both contribute in a real stratocumulus cloud case.

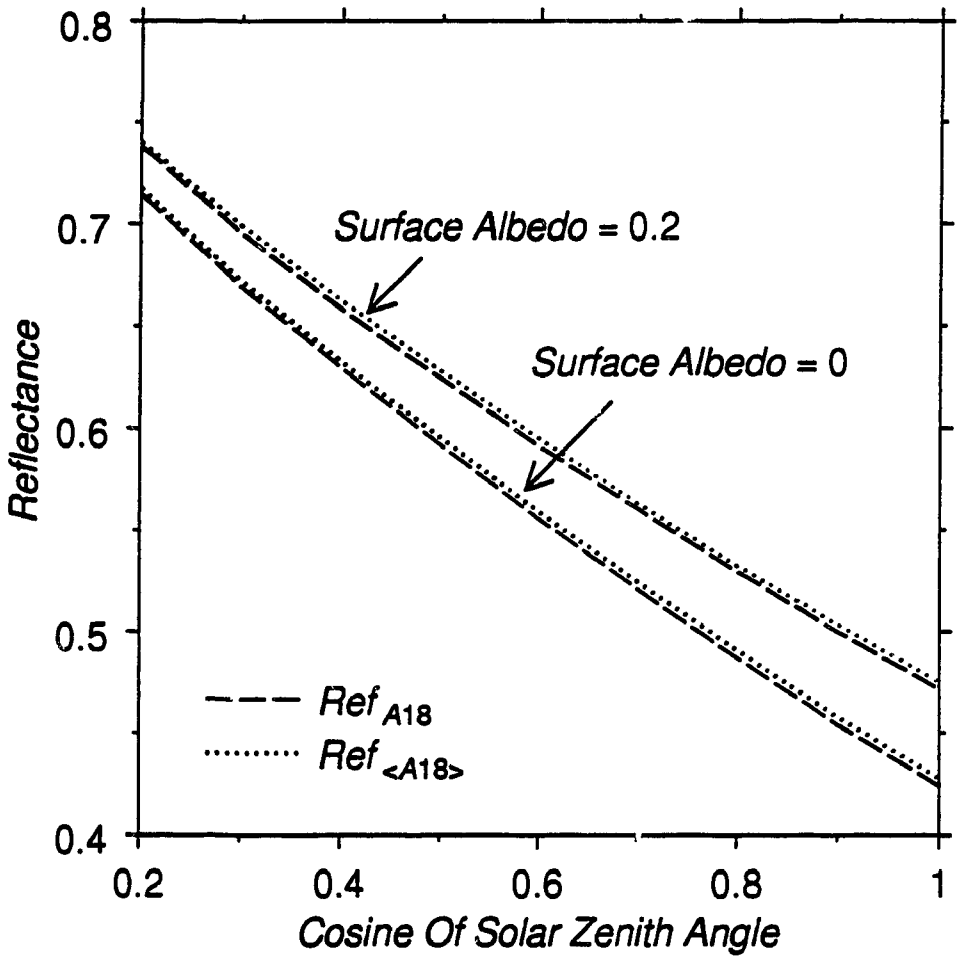

Figure 2.5: Vertical Reflectances for overcast clouds with different surface albedos. A18 is the real cloud, and <A18> is the vertically averaged counterpart.

In Fig.2.5, the reductions of the solar reflectance due to the cloud internal inhomogeneity are small, and the reductions are not obviously dependent on the solar zenith angle and the surface albedo. Since the considered cloud case is a typical stratocumulus cloud, we conclude that for an overcast stratocumulus cloud the influence of internal inhomogeneity on the radiative transfer is not important for cloud albedo. The homogeneous plane-parallel assumption is a good approximation for a horizontally infinite overcast stratocumulus cloud field.

2.3.2 Broken cloud field with vertical internal inhomogeneity

For overcast clouds, the inhomogeneity in the micro-physical quantities of the cloud leads to a slightly reduced cloud albedo in comparison with that of the plane-parallel counterpart. However, the stratocumulus cloud field is not usually of overcast form. Therefore, the investigation of the internal inhomogeneity should be extended to the broken cloud field.

In order to compare broken cloud field results with the results of the overcast clouds, A18 is chosen as a real cloud case. Noonkester (1984) did not show the cloud size distribution of the stratocumulus cloud field; he concentrated on the micro-physical quantities. Therefore, the cloud field arrangement must be specified. An idealized broken cloud field is taken in the form of an extended regular array of cubes. Denote the side length of a cubic cloud by D, the height of a cubic cloud by H, and the distance between two neighbouring cloud centers by S. The aspect ratio $a = H/D$. The distance ratio $R = S/D$ and the cloud amount $N = R^{-2}$. Consider a regular array of clouds of aspect ratio $a = 1$. The cubic clouds have a side length of 200 m. The change of the distance ratio corresponds to the change of cloud amount. The cloud vertical internal inhomogeneity of optical properties are also determined by Fig.2.2, the cloud lateral variation of optical properties due to entrainment is ignored.

For the cloud field consisting of cubic clouds, the results of the radiative transfer is dependent on the azimuthal angle. Since the clouds in a real cloud field do not

show a specific orientation, the azimuthally averaged case may be interpreted as more realistic from a climatological point of view (Barker and Davies, 1992). Therefore, in the following, most of results are azimuthally averaged.

In Fig.2.6, the cloud reflectances of the regular cloud array (A18) with different distance ratios are presented. The ground surface albedo is assumed to be zero. If the surface albedo is not zero, the reflectance is dependent on the cloud base height. In Fig.2.6 when $R = 1.2$, the difference between the two curves of A18 and its vertically averaged counterpart <A18> is still small. As the distance ratio increases, the differences in the reflectances of A18 and <A18> for a large solar zenith angle are enhanced. However, this enhancement is only up to a certain value. From $R = 3$ to $R = 5$, the relative enhancements in the reflectances are not much different for different distance ratios.

When an overcast cloud field is separated into a broken cloud field with a regular array, and if the solar zenith angle is not zero, the lateral sides of the cubic clouds would increase the illuminated area. Consider a photon entering the higher part of a lateral side of the cubic cloud with vertical internal inhomogeneity. Such a region corresponds to a larger extinction coefficient, a larger asymmetry factor and a smaller single scattering albedo, in comparison with its vertically averaged counterpart. Then the photon would have a larger tendency to go downward or to be absorbed, and reflectance will decrease. The physics is the same as that discussed for the overcast cloud in the last subsection.

Now consider a photon entering the lower part of a lateral side of the cubic cloud. In contrast to the vertically averaged case, this region corresponds to a smaller extinction coefficient, a smaller asymmetry factor and a larger single scattering albedo. The smaller asymmetry factor leads to the photon deviating more from its original path direction, so the distribution of the scattered photons becomes more isotropic, which would increase the reflectance. The larger single scattering albedo means that the photons are less likely to be absorbed in this region, and the reflectance would

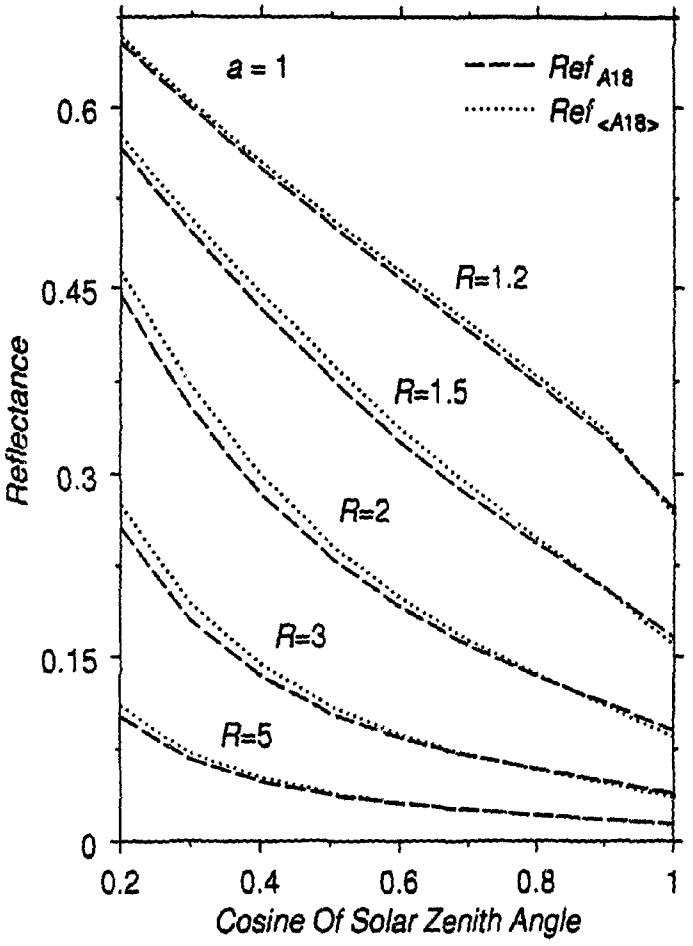

Figure 2.6: Reflectances of the regular array cloud field for different distance ratios.

increase. However, the smaller extinction coefficient in this region results in less scattering. Therefore the downward directed solar photons would undergo less scattering events and pass through the cloud more easily. This effect would compensate for the increase of reflectance due to smaller asymmetry factors and larger single scattering albedos in this region. Taking into account the two regions, for a large solar zenith angle, the net result is that the difference in reflectance is enhanced (Fig.2.6).

For a large solar zenith angle, as the distance ratio increases, the exposed lateral sides intercept more photons. Then the differences in reflectance between A18 and <A18> are enhanced (from $R = 1.2$ to $R = 2$, in Fig.2.6). However, beyond a certain value, further increase in the distance ratio does not lead to an increase of intercepted photons by the lateral sides. The differences between A18 and <A18> are not further enhanced ($R = 3$ and $R = 5$ in Fig.2.6).

For all cases in Fig.2.6, when the solar zenith angle is very small the situation is reversed. The reflectance of A18 becomes larger than that of <A18> (the differences are larger than the standard deviation), which suggests that in a broken cloud field case the heterogeneity does not always lead to a reduced cloud reflectance.

The physical explanation for this anomalous phenomenon is that the scattered photons of the direct downward solar beam have a larger chance to leak through the lateral side boundary if the asymmetry factor is smaller. Some of the leaked photons can be absorbed by the surface directly. In the upper part of a real cumulus cloud the asymmetry factor is larger, in comparison with the vertically averaged counterpart case. Since the photon number of the direct solar beam decays exponentially as the beam transports downward, the effect of photons leaking through the lateral sides is more dependent on the situation of the upper part of the cloud. On the other hand, since the solar zenith angle is very small, the cloud lateral effect discussed above is very weak.

This argument can be verified by a test. Usually when a cloud becomes "aged", or in a precipitation state, the droplets with larger radii are in the lower part of the cloud and the smaller droplets are in the upper part of the cloud. The situation is opposite

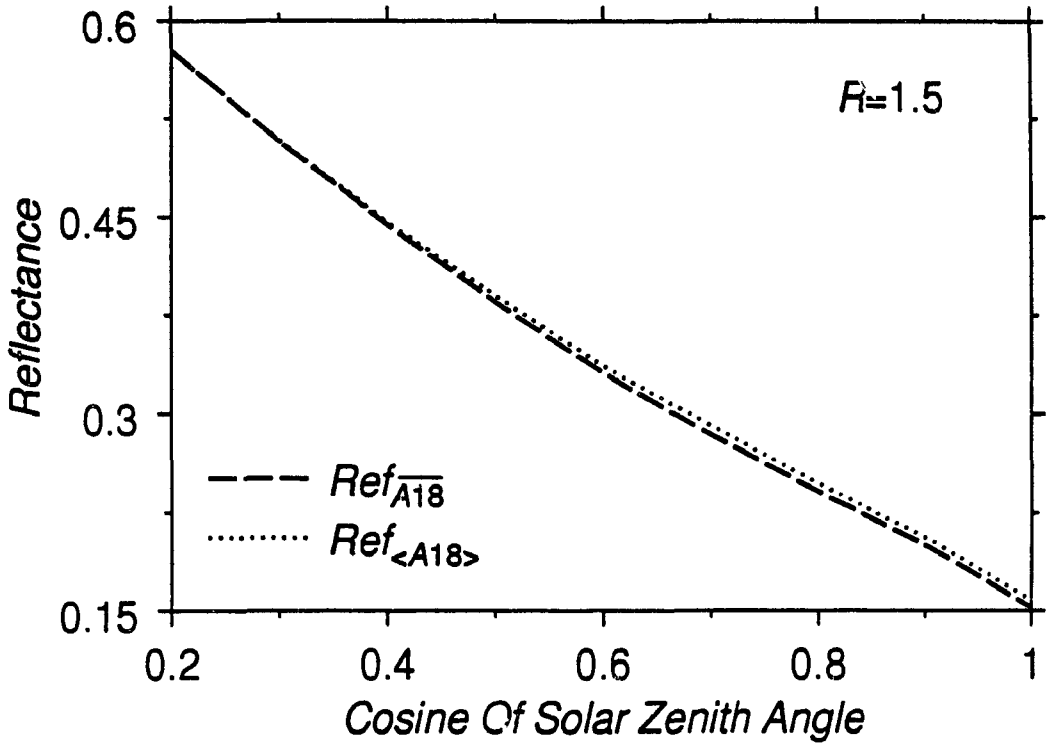

Figure 2.7: Reflectances of an "aged" cloud ($\overline{\text{A18}}$) with an inverse variation of internal optical quantities of A18 and its vertical averaged counterpart.

to that of growing cumulus clouds. Considering the photon transport in a "aged" cloud, for simplicity and comparison, we assume that variations with the height of single scattering properties are opposite to that of cloud A18, i.e. the LWC and cross sectional area linearly decrease with height (denote as $\overline{\text{A18}}$). The calculated results are shown in Fig.2.7. In comparison with that of <A18>, the asymmetry factor is smaller in the upper part of cloud $\overline{\text{A18}}$. At a very small zenith angle, the reflectance of <A18> exceeds that of $\overline{\text{A18}}$, since the photons have a better chance to leak through the lateral boundary when the asymmetry factor is smaller in the upper part of the cloud $\overline{\text{A18}}$.

2.3.3 Cloud absorption

Cloud solar heating rate plays an important role in the local energy balance. Studies show that the solar heating rate also has a considerable effect on cloud droplet (ice crystal) growth (Stephens, 1983; Ramaswamy and Detwiler, 1986). The cloud absorption anomaly has been one of the challenging problems in atmospheric science for many years (Stephens and Tsay, 1990).

In Fig.2.8, the cloud absorptions corresponding to different distance ratios are plotted. The distance ratio $R = 1$ represents the overcast cloud. In Fig.2.8 shows that the cloud absorption is enhanced for the overcast cloud with a realistic vertical inhomogeneity, in comparison with that of the homogeneous counterpart. The cloud absorption anomaly refers to the fact that measurements of cloud solar absorption tends to exceed theoretical estimates. However the theoretical estimates are based on the plane-parallel assumption (Stephens and Tsay, 1990) and the cloud inhomogeneity has been ignored. Therefore, Fig.2.8 ($R = 1$) suggests that the cloud absorption anomaly might be partly attributed to the cloud vertical inhomogeneity. The physical explanation of the enhancement of absorption has been given in subsection 2.3.1. The region with larger k corresponds to smaller ω; more scattering events occur in higher absorption regions.

When the distance ratio $R = 1.2$, cloud absorptions are sharply reduced for small

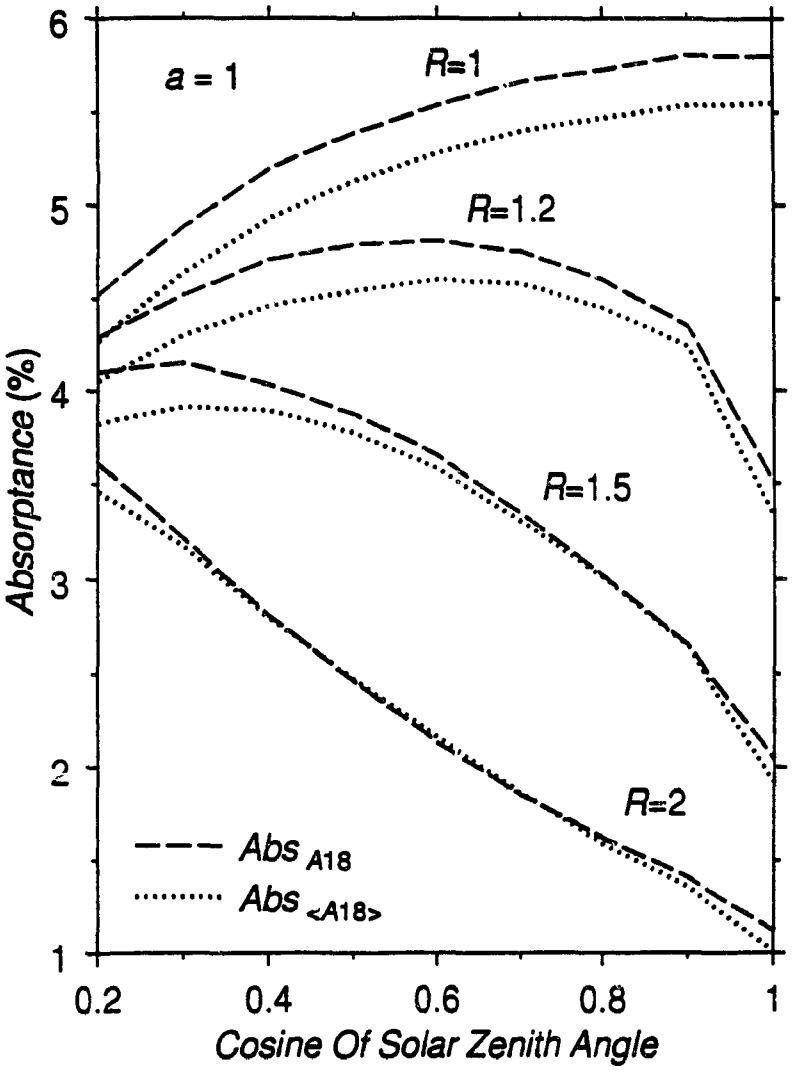

Figure 2.8: Cloud absorptance for different distance ratios.

zenith angles. Since many photons directly penetrate through the intervals between the clouds, less photons have been trapped by the clouds. As the distance ratio increases further, the absorption by clouds is decreased, and the differences in absorption between the real clouds and their vertically averaged counterparts are reduced. As discussed in subsection 2.3.2, the lower part of real stratocumulus cloud has smaller k and larger ω, in comparison with its vertically averaged counterpart. Photons which enter the lower parts of the lateral sides pass more easily through the cloud with less probability of being absorbed. This is opposite to the effect of larger absorption at the upper part of the cloud, and results in the reduction of the difference in absorptions of A18 and <A18> ($R = 1.5$ and $R = 2$ in Fig.2.8).

2.3.4 Effective cloud amount for cloud absorption

The cloud absorption is plotted as a function of the cloud coverage in Fig.2.9. Besides the inhomogeneous broken cloud and its vertically averaged counterpart, the corresponding plane-parallel case is also presented. The plane-parallel cloud absorption at the same value of cloud coverage is $Abs_{pp}(N) = Abs_{pp}(100\%)N$, where the $Abs_{pp}(100\%)$ is the absorption for a plane-parallel cloud and N is the cloud amount.

When $\theta_0 = 0^0$, the absorption of fractionally covered plane-parallel cloud exceeds the absorptions of broken clouds for most values of the cloud amount. This is due to the boundary leak of photons in broken cloud cases. Also, Fig.2.9(a) shows that the absorption of the inhomogeneous cloud is larger than its averaged counterpart.

When $\theta_0 = 60^0$, the absorptions of both cases of the broken cloud dramatically exceed that of the plane-parallel cloud for all values of the cloud amount. This is because more photons have been intercepted by the lateral sides. In the large cloud amount regions, the absorption of inhomogeneous cloud is larger than its homogeneous counterpart.

For a large solar zenith angle, the substantial increase of cloud absorption by broken clouds (A18 or <A18>) in comparison with the plane-parallel case seems to show that the variability of cloud absorption is mostly associated with cloud geometry

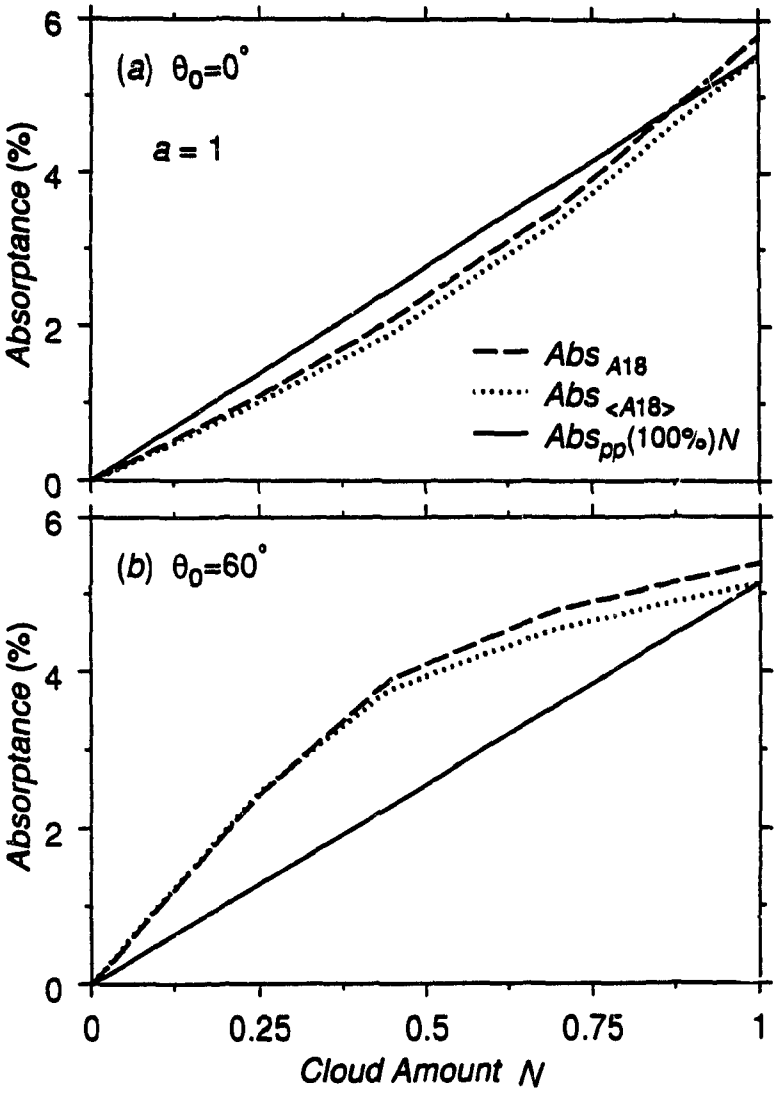

Figure 2.9: Cloud absorptance for different cloud amounts, aspect ratio $a = 1$.

rather than micro-physical variation in this case.

Fig.2.10 shows the cloud amount dependence of cloud absorption for A18 with $a = 0.2$. The rectangular slab clouds have a side length of $1000\,m$. In comparison with Fig.2.9, for the cloud with larger side length, the differences in cloud absorption between broken cloud (A18 or <A18>) and the plane-parallel case are reduced especially for the case of a small value of cloud amount. The cloud lateral side area per unit cloud amount is proportional to $DH/S^2 = NH/D$. For a given cloud amount, the cloud lateral side area per unit cloud amount is in inverse proportion to the cloud side length. Thus the number of photons trapped by lateral side is less for a cloud array containing clouds with larger side lengths. Hence the differences in cloud absorption between broken cloud and plane-parallel case are reduced.

From above, it can be found that using only the cloud amount to describe the geometry of broken cloud is incomplete, and the parameterization of effective cloud amount is necessary. In earlier parameterizations of effective cloud amount for cloud absorption (Harshvardhan and Thomas, 1984), only the cloud geometry factor was considered. In some cases, especially for thin clouds or small zenith angles, the increase of illuminated cloud area would not enhance the cloud reflectance. The cloud internal optical properties are also important and should be taken into account in the parameterization of effective cloud amount. This was realized by Welch and Wielicki (1985). Besides cloud geometry factors, the cloud optical depth also plays an important role in the Welch and Wielicki (WW) parameterization. The effective cloud amount N_e in the WW parametrization is given by

$$N_e/N = \begin{cases} 1 + a\,f\tan\theta_0 - C\mu_0(1-N^2) & N \le N_s \\ (1-f) + f\,N^{-1/2} - C\mu_0(1-N^2) & N \ge N_s \end{cases} \tag{2.29}$$

where a is the aspect ratio, $\mu_0 = \cos\theta_0$, $N_s = (1 + a\tan\theta_0)^{-2}$, f and C are

$$f = \{\ln[1.05 + 0.045(\ln\tau)^2] + 0.05(\mu_0^{-2} - 1)[1 - (\tau/70)^2]$$

$$- 0.0015\mu_0^{-4} - 0.25(\mu_0 - \mu_*)(\tau/50)^2\}(1 + N^2), \tag{2.30}$$

$$C = 0.25 - 0.13\tau^{-2} - 0.05(\tau/50)^2, \tag{2.31}$$

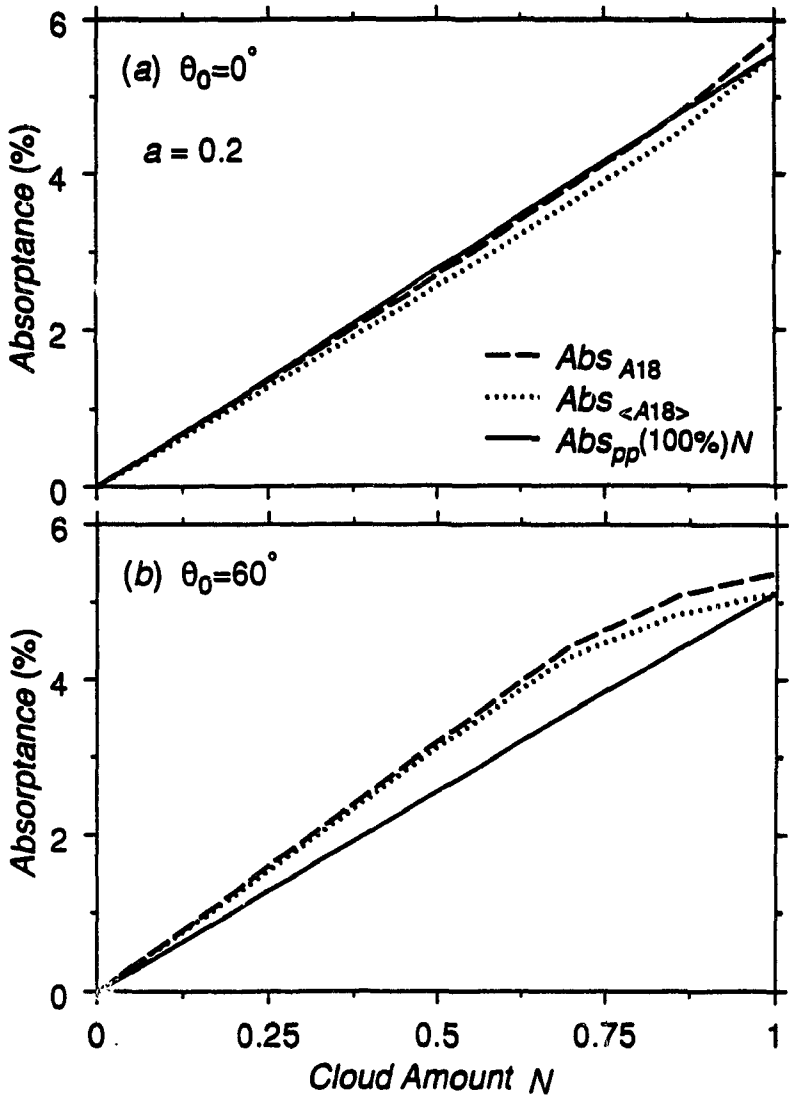

Figure 2.10: Cloud absorptance for different cloud amounts, aspect ratio $a = 0.2$.

where $\mu_* = \cos 72.5°$, and τ is cloud vertical optical depth. The WW parametrization is determined from cloud reflectance. It is unknown if this parameterization can be extended to broken cloud absorption. Similar to reflectance, the effective cloud amount for broken clouds A18 and its vertically averaged counterpart <A18> in cloud absorption case are defined as

$$Abs_{A18} = Abs_{pp}(100\%)N_{e\,A18}, \tag{2.32}$$

$$Abs_{<A18>} = Abs_{pp}(100\%)N_{e\,<A18>}, \tag{2.33}$$

where $N_{e\,A18}$ and $N_{e\,<A18>}$ are effective cloud amounts for A18 and <A18> respectively.

$N_{e\,A18}/N$ ($N_{e\,<A18>}/N$) represents the ratio of the cloud absorption for a broken cloud field (its vertically averaged counterpart) to that of the plane-parallel cloud case. $N_{e\,A18}/N$, $N_{e\,<A18>}/N$ and N_e/N by the WW parametrization for three values of zenith angle are plotted in Fig.2.11. The aspect ratio $a = 1$. The cloud vertical optical depth obtained by band fractional weighted mean is 9.37 for A18. In this case the azimuthal angle $\varphi = 0°$, since the WW parameterization is for fixed azimuthal angle. Fig.2.11 shows that the WW parametrization nearly agrees with the Monte Carlo simulation in small zenith angle cases. The change tendencies for Monte Carlo simulation and parametrization are quite similar. However, in large zenith angle cases the WW parameterization underestimates the effective cloud amount. This defect is due to the different physical processes of reflectance and absorption. In Fig.2.11 also it can be found that the cloud vertical inhomogeneity is not a negligible factor in determining the effective cloud amount. Cloud vertical internal inhomogeneity can cause about a 10% difference in effective cloud amount.

In the above calculations, only one real cloud case has been considered. Here we briefly consider another real cloud case of M29 in (Noonkester, 1984). The formulae of Eqs.(2.2) and (2.4) do not cover the whole vertical cloud region, the values of LWC and r_e for the upper part of the cloud are obtained from Fig.2.1 directly. Fig.2.12 shows the calculation results for $a = 1$; $R = 1$ and 1.5. The surface albedo is zero.

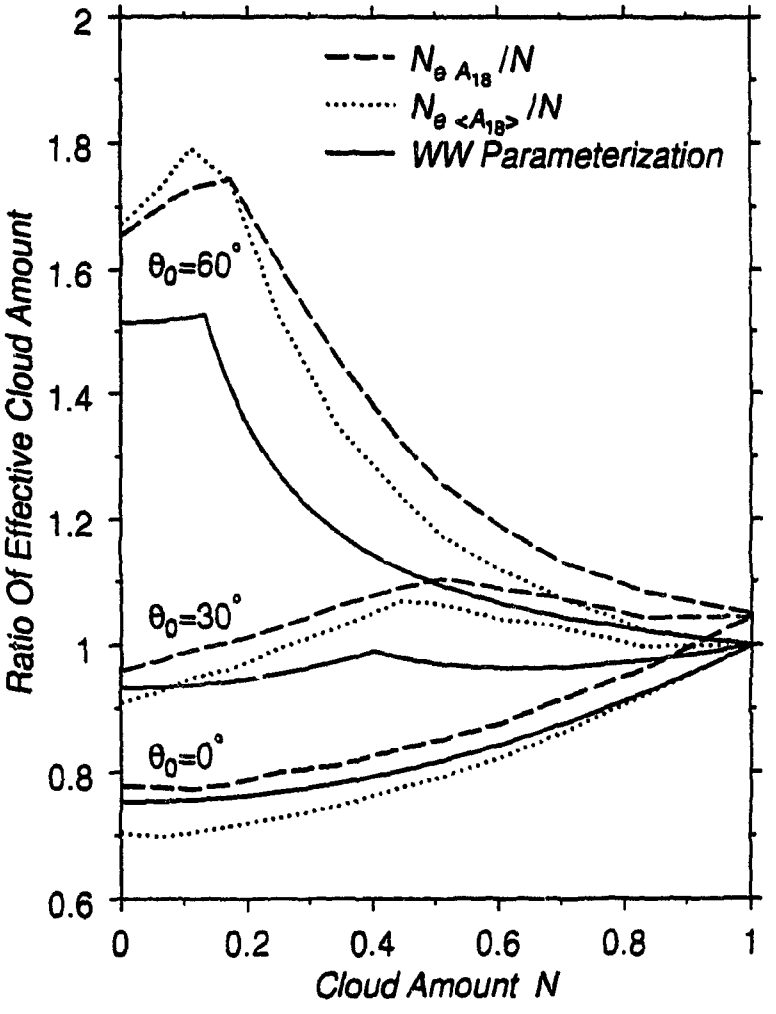

Figure 2.11: Ratios of effective cloud amounts to cloud amounts and corresponding WW paramerizations.

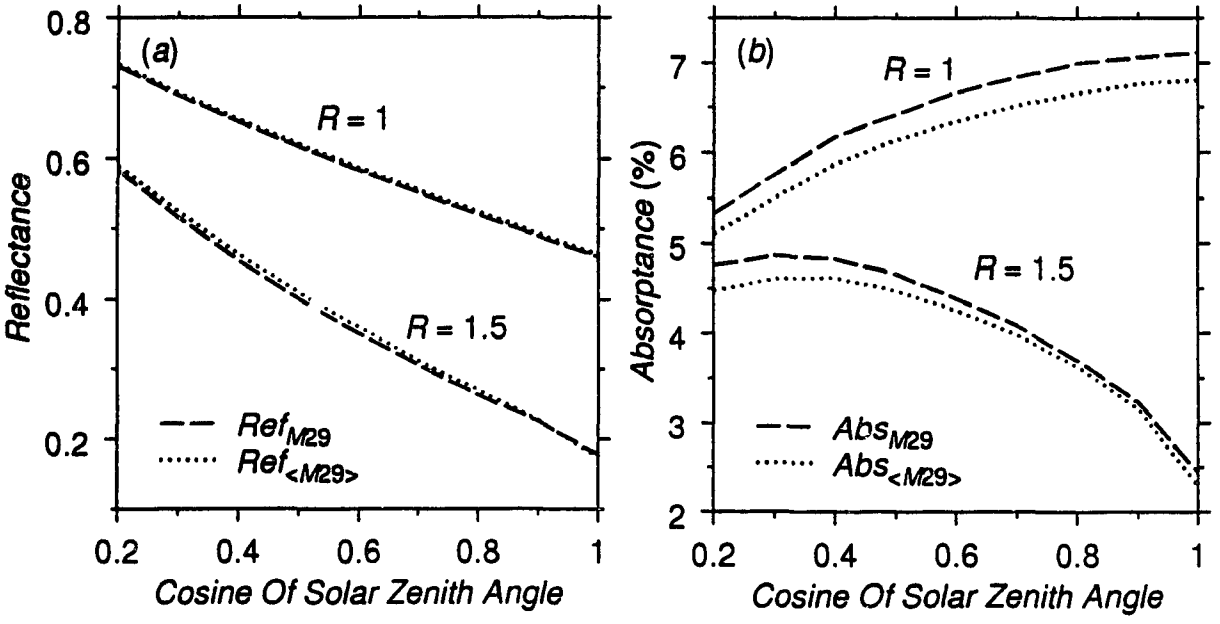

Figure 2.12: Reflectances and absorptance for the cloud M29 with different distance ratios.

We find the results are quite similar to that of the corresponding cases in A18. Our conclusions therefore appear to have some general validity for the considered type of cloud.

2.4 Summary

In contrast to previous Monte Carlo cloud simulations, the cloud micro-physics of spatially varying single scattering properties has been introduced into our model. The relations between the observable physical quantities (LWC and r_e) and the single scattering properties are determined by the parameterization of shortwave radiative properties of water clouds. Then, the real process of photon transport in clouds is simulated. The cloud examples were chosen from observational results; they were typical stratocumulus clouds with average extinction coefficient of about 50 km^{-1}.

In overcast clouds, the reflectance was reduced for a real cloud with internal vertical inhomogeneity in comparison with the vertical averaged counterpart. Generally the reductions were small. However, in broken cloud cases, the difference in reflectances for the inhomogeneous clouds and their averaged counterparts were enhanced at large solar zenith angles.

In broken cloud fields, it is not always true that a heterogeneous cloud leads to the reduction of cloud reflectance. The radiative transfer in clouds is dependent on the cloud geometry and the mutual relationship between three single scattering variables. Simplified arguments can not predict the change of reflectance.

When cloud amount is large, inhomogeneous clouds lead to an increase of cloud absorption, which is one factor that should be taken into account in the cloud absorption anomaly problem. In general, the difference in cloud absorption due to cloud vertical internal inhomogeneity is smaller than that due to cloud geometry. The parametrization of effective cloud amount determined from cloud reflectance can be used approximately for cloud absorption, especially in the case of a small zenith angle.

Chapter 3

Perturbation Solution For 3-D Radiative Transfer In A Horizontally Periodic Inhomogeneous Cloud Field

In this chapter we turn our interest to clouds with horizontal inhomogeneity. Weinman and Swarztrauber (1967) considered radiative transfer in plane-parallel layers with the horizontal inhomogeneity of volume extinction coefficient $k = k_0 + k_1\cos(lx)$. Even under the assumption of isotropic scattering, they were only able to solve the problem numerically. Recently Kobayashi (1991) applied the discrete-ordinate method to an inhomogeneous cloud with volume extinction coefficient of one dimensional variation $\alpha = B + H_1\cos(\pi ax/L_x) + H_2\cos(\pi bx/L_x)$. The direct use of the discrete-ordinate method to the radiative transfer equation in an inhomogeneous medium results in the mixture of different modes. The analytical solution becomes complicated due to formulation in the form of the inverse matrix for the eigenvalue problem. The solution can be obtained only numerically. Evans (1993) purposed a 2D numerical model for radiative transfer in clouds with internal inhomogeneity. What we are interested in is an analytical method.

Due to convection, turbulence and other factors, clouds are generally inhomogeneous in both horizontal and vertical directions. For instance, stratocumulus clouds are horizontally inhomogeneous. The updraft regions have larger liquid water content (larger extinction coefficient) than surrounding downdraft regions. We can simply simulate such horizontal inhomogeneity as a two dimensional variation in the extinction coefficient,

$$k = k_0\{1 + \epsilon[\cos(ax) + \cos(by)]\} , \tag{3.1}$$

where k_0, ϵ, a, b are constants, and $\epsilon < 0.5$. The cloud layer will still be taken as plane-parallel, the inhomogeneity refers to the interior of the cloud. To solve the three dimensional radiative transfer equation directly in an inhomogeneous medium such as that of Eq.(3.1) is difficult, since the equation is equivalent to a set of partial differential equations with non-constant coefficients. Generally, exact solutions are not known. However one way to avoid this difficulty is through a perturbation method. The perturbation method for solving differential equations is commonly used in many branches of physics. Using the perturbation method, a complicated differential equation is replaced by a series of differential equations of simpler form. The perturbation method for the three dimensional radiative transfer equation in a cloud with cosinusoidal extinction coefficient was considered by Romanova (1975); however the explicit solution for the radiance (irradiance) was not obtained. The case of one dimensional radiative transfer was considered by Box et al. (1989). In the perturbation method, the lowest order solution should be obtained; then the higher order solutions may be obtained by recurrence relations. In radiative transfer problems, the lowest order solution is the solution for the plane-parallel homogeneous case, which has already been obtained. The solution of the plane-parallel homogeneous case is then the starting point to develop the higher order perturbation calculations. Usually in perturbation methods, the higher order calculations are cumbersome. However, if the perturbation coefficient ϵ in Eq.(3.1) is much smaller than one, i.e. the inhomogeneity of the cloud is small, we can obtain very accurate results even to the first order of the perturbation calculation.

3.1 The lowest order solution for plane parallel case

The three dimensional radiative transfer equation with external source term is

$$\frac{dI}{ds} = k'(-I + J + J_0) \,, \tag{3.2}$$

with

$$\frac{d}{ds} = \nu\cos\varphi\frac{d}{dx} + \nu\sin\varphi\frac{d}{dy} + \mu\frac{d}{dz} \,, \tag{3.3}$$

where $\mu = \cos\theta$, $\nu = \sin\theta$, θ is the local zenith angle, φ is the local azimuth angle, k' is the scaled extinction coefficient, $I(s,\theta,\varphi)$ is the diffuse radiance in the direction θ,φ at distance s, J is the source term due to internal multiple scattering and J_0 is the source term due to single scattering with the direct solar beam. Expanding the phase function to the first order of Legendre polynomials, we have (Davies, 1978)

$$J = \frac{\omega'}{4\pi}\int_0^{2\pi} d\varphi' \int_0^{\pi} \{1 + 3g'[\mu\mu' + \nu\nu'\cos(\varphi - \varphi')]\} I(s,\theta',\varphi')\, d\theta' \,, \tag{3.4}$$

$$J_0 = \frac{\omega'}{4\pi}\{1 + 3g'[\mu\mu_0 + \nu\nu_0\cos(\varphi - \varphi_0)]\} F(s,\theta_0,\varphi_0) \,, \tag{3.5}$$

and

$$F(s,\theta_0,\varphi_0) = \pi F_0 e^{-\tau_0} \,. \tag{3.6}$$

where μ_0 and ν_0 are the cosine and sine of solar zenith angle respectively, g' is the scaled asymmetry factor, ω' is the scaled single scattering albedo, and πF_0 is the incident solar irradiance. The optical depth for the direct solar beam is defined as

$$\tau_0 = \int k'\, ds \,. \tag{3.7}$$

The relationship of the scattering factors to the scaled scattering factors are determined by considering the separation of the forward scattering peak from the phase function (Joseph *et al.*,1976):

$$k' = k(1 - \omega g^2) \,, \tag{3.8}$$

$$\omega' = \omega(1-g^2)/(1-\omega g^2)\,, \tag{3.9}$$

$$g' = g/(1+g)\,. \tag{3.10}$$

In the plane-parallel homogeneous case, the medium is homogeneous (k and k' are constants) and horizontally infinite. Therefore the radiative field has no horizontal variability, and it is a function of the vertical variable only. Using the Eddington approximation, we expand the radiance

$$I^0(z,\theta,\varphi) = I_0^0(z) + I_x^0(z)\nu\cos\varphi + I_y^0(z)\nu\sin\varphi + I_z^0(z)\mu\,, \tag{3.11}$$

where we append the superscript '0' to describe the radiance in the lowest order for the plane-parallel case. Also, we denote the k' by k_0' for the lowest order case, since the extinction coefficient is a constant. From Eqs.(3.4) and (3.5)

$$J^0 = \omega'\{I_0^0(z) + g'[I_x^0(z)\nu\cos\varphi + I_y^0(z)\nu\sin\varphi + I_z^0(z)\mu]\}\,, \tag{3.12}$$

$$J_0^0 = \frac{\omega'}{4}\{1+3g'[\mu\mu_0 + \nu\nu_0\cos(\varphi-\varphi_0)]\}F_0 e^{-k_0'z/\mu_0}\,. \tag{3.13}$$

Integrating Eq.(3.2) in turn over 4π steradians with respect to $d\mu d\varphi$, $\nu\cos\varphi d\mu d\varphi$, $\nu\sin\varphi d\mu d\varphi$, $\mu d\mu d\varphi$ yields respectively (Davies, 1978),

$$\frac{dI_z^0}{dz} = -3k_0'(1-\omega')I_0^0 + \frac{3}{4}k_0'\omega' F_0 e^{-k_0'z/\mu_0}\,, \tag{3.14}$$

$$0 = -k_0'(1-\omega'g')I_x^0 + \frac{3}{4}k_0'\omega'g'\nu_0\cos\varphi_0 F_0 e^{-k_0'z/\mu_0}\,, \tag{3.15}$$

$$0 = -k_0'(1-\omega'g')I_y^0 + \frac{3}{4}k_0'\omega'g'\nu_0\sin\varphi_0 F_0 e^{-k_0'z/\mu_0}\,, \tag{3.16}$$

$$\frac{dI_0^0}{dz} = -k_0'(1-\omega'g')I_z^0 + \frac{3}{4}k_0'\omega'g'\mu_0 F_0 e^{-k_0'z/\mu_0}\,. \tag{3.17}$$

where I_x^0 and I_y^0 are given by Eqs.(3.15) and (3.16) directly. From Eqs.(3.14) and (3.17) we obtain (Shettle and Weinman, 1971)

$$I_0^0 = Ce^{-\lambda z} + De^{\lambda z} - \alpha e^{-k_0'z/\mu_0}\,, \tag{3.18}$$

$$I_z^0 = W(Ce^{-\lambda z} - De^{\lambda z}) - \beta e^{-k_0' z/\mu_0} , \tag{3.19}$$

where

$$\lambda = [3k_0'^2(1-\omega')(1-g'\omega')]^{\frac{1}{2}} , \tag{3.20}$$

$$W = [3(1-\omega')(1-g'\omega')]^{\frac{1}{2}} , \tag{3.21}$$

$$\alpha = \frac{3}{4}k_0'^2\omega'\mu_0^2 F_0[1+g'(1-\omega')]/(k_0'^2 - \mu_0^2\lambda^2) , \tag{3.22}$$

and

$$\beta = \frac{3}{4}k_0'^2\omega'\mu_0 F_0[1+3g'\mu_0^2(1-\omega')]/(k_0'^2 - \mu_0^2\lambda^2) . \tag{3.23}$$

The constants C and D are determined by the boundary conditions. For simplicity, we assume there is no downward directed diffuse irradiance at the top of the cloud layer. Also, we take the surface albedo to be zero (the ground is taken to be blackbody), so there is no upward directed diffuse irradiance at the bottom of the cloud layer. We will therefore require

$$F^{0\downarrow}(0) = \pi[I_0^0(0) + \frac{2}{3}I_z^0(0)] = 0 , \tag{3.24}$$

$$F^{0\uparrow}(z_0) = \pi[I_0^0(z_0) - \frac{2}{3}I_z^0(z_0)] = 0 , \tag{3.25}$$

where z_0 is the vertical geometric length of the cloud layer. From Eqs.(3.24) and (3.25) we can obtain C and D. We have only considered the nonconservative case ($\omega \neq 1$), the discussion is similar for the conservative case.

Finally we point out that I_x^0 and I_y^0 may be neglected if only the upwelling ($\mu = -1$) and downwelling radiances ($\mu = 1$) or upward and downward irradiances are required.

3.2 Perturbation solution

Now we discuss the radiative transfer in an inhomogeneous cloud. We consider the extinction coefficient given in Eq.(3.1) with two dimensional horizontally periodic variations, and replace the k and k_0 with the scaled variables. The ϵ in Eq.(3.1) is

taken to be much smaller than one so that terms of higher order in powers of ϵ can be neglected. The solar beam flux $F(s,\theta_0,\varphi_0) = \pi F_0 e^{-\tau_0}$, and the optical depth for the direct solar beam is

$$\tau_0 = \int k_0'\{1+\epsilon[\cos(ax)+\cos(by)]\}\,ds = k_0' s + \epsilon H(s,\theta_0,\varphi_0)\ , \tag{3.26}$$

where the geometric path length $s = z/\mu_0$ and

$$\begin{aligned} H &= \int k_0'[\cos(ax)+\cos(by)]\,ds \\ &= \frac{k_0'}{\mu_0\eta}\{\sin(ax)[1-\cos(\eta z)]+\cos(ax)\sin(\eta z)\} \\ &+ \frac{k_0'}{\mu_0\zeta}\{\sin(by)[1-\cos(\zeta z)]+\cos(by)\sin(\zeta z)\}\ , \end{aligned} \tag{3.27}$$

where $\eta = a\nu_0\cos\varphi_0/\mu_0$ and $\zeta = b\nu_0\sin\varphi_0/\mu_0$. As $\theta_0 \to 0$, $H \to k_0'[\cos(ax)+\cos(by)]z$, therefore $\int k'\,as = k'z$.

H is finite for a finite optical depth and, from Eq.(3.27), upper and low bounds are given by

$$-2k_0' s \le H \le 2k_0' s\ . \tag{3.28}$$

Taking $k_0' \approx 0.014\,m^{-1}$ for typical stratocumulus clouds, and $\epsilon = 0.1$, then even for s of several hundred meters we have $2\epsilon k_0' s < 1$. Therefore we can expand

$$\pi F_0 e^{-k_0' s-\epsilon H} \approx (1-\epsilon H)\pi F_0 e^{-k_0' s}\ . \tag{3.29}$$

Of course, if s is too large, the inequality of $2\epsilon k_0' s < 1$ is no longer valid. However, when s is large, the factor $e^{-k_0' s}$ approaches zero and the absolute error for the expansion is small. From Eq.(3.28) and Eq.(3.29)

$$\pi F_0 e^{-k_0' s-\epsilon H} < \pi F_0 e^{-k_0' s+2\epsilon k_0' s}\ . \tag{3.30}$$

In Fig.3.1 we plot the maximum limit ($H = -2k_0' s$) of the incident solar flux and its approximate expansion by Eq.(3.29). We find that for a large geometric path

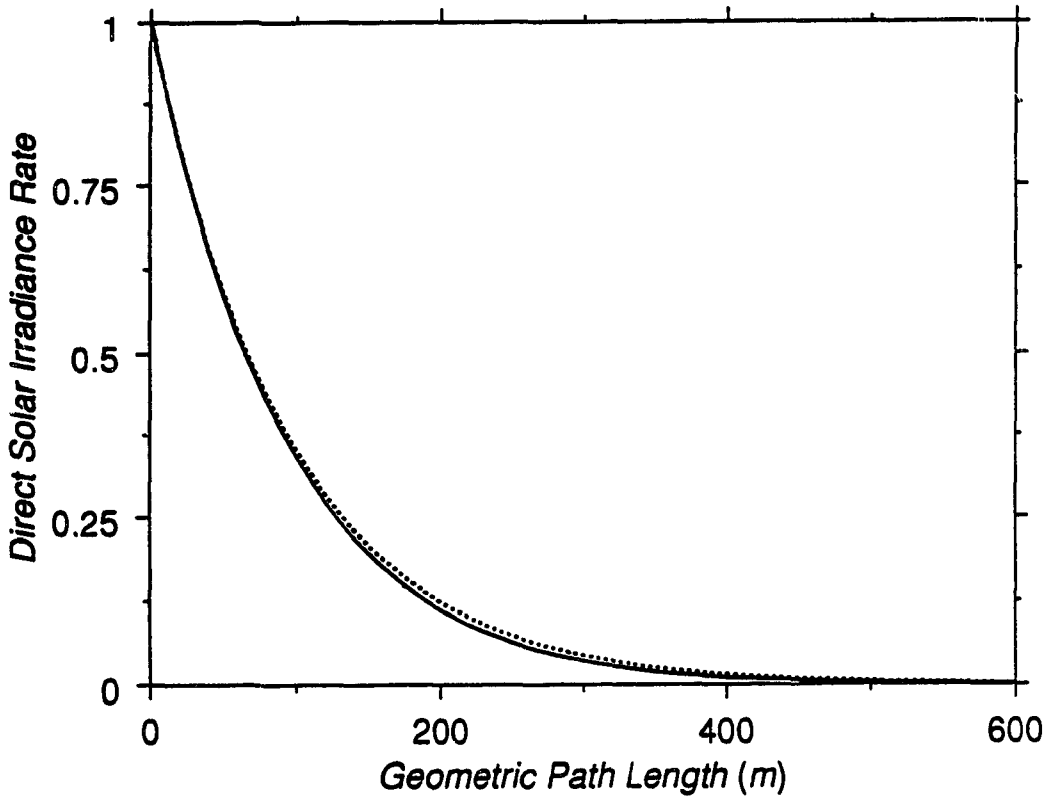

Figure 3.1: The maximum limit value of the direct solar irradiance (dotted line) and its expansion approximation (solid line) as functions of the geometric path length. The irradiance is normalized with respect to πF_0.

the contribution of the direct solar beam to the diffuse radiative transfer becomes negligible, and the approximate expansion is always accurate.

In terms of the expansion in Eq.(3.29), J_0 can be written as

$$J_0 = J_0^0 + \epsilon J_0^1 \,, \tag{3.31}$$

where J_0^0 is given in Eq.(3.13), and

$$J_0^1 = -\frac{\omega'}{4}\{1 + 3g'[\mu\mu_0 + \nu\nu_0\cos(\varphi - \varphi_0)]\}HF_0 e^{-k_0' z/\mu_0} \,. \tag{3.32}$$

To use the perturbation method to solve the radiative transfer equation we expand the radiance I in powers of ϵ. To the first order, we retain only the first two terms

$$I = I^0 + \epsilon I^1 \,, \tag{3.33}$$

where I^0 is the lowest order of the radiance discussed in the last section, and I^1 is the first order correction. Therefore, the radiative transfer equation becomes

$$\frac{d}{ds}(I^0+\epsilon I^1) = k_0'\{1+\epsilon[\cos(ax)+\cos(by)]\}[-(I^0+\epsilon I^1)+(J^0+\epsilon J^1)+(J_0^0+\epsilon J_0^1)] \,. \tag{3.34}$$

Regrouping the terms in Eq.(3.34) with the same order of ϵ yields,

$$\frac{dI^0}{ds} = k_0'(-I^0 + J^0 + J_0^0) \,, \tag{3.35}$$

$$\frac{dI^1}{ds} = k_0'(-I^1 + J^1 + J_0^1) + k_0'[\cos(ax) + \cos(by)](-I^0 + J^0 + J_0^0) \,. \tag{3.36}$$

The lowest order solution for Eq.(3.35) has been given in the last section by the Eddington approximation. Eq.(3.36) is an inhomogeneous partial differential equation with constant coefficients. We again use the Eddington expansion to first order of the perturbation solution

$$I^1(s,\theta,\varphi) = I_0^1(s) + I_x^1(s)\nu\cos\varphi + I_y^1(s)\nu\sin\varphi + I_z^1(s)\mu \,. \tag{3.37}$$

By a process similar to that for the lowest order solution, we obtain

$$\frac{\partial I_x^1}{\partial x} + \frac{\partial I_y^1}{\partial y} + \frac{\partial I_z^1}{\partial z} = -3k_0'(1-\omega')I_0^1 + 3k_0'[\cos(ax)+$$

$$+\cos(by)][-(1-\omega')I_0^0+\frac{\omega'}{4}F_0e^{-k_0'z/\mu_0}]-\frac{3}{4}k_0'\omega'HF_0e^{-k_0'z/\mu_0}\ , \tag{3.38}$$

$$\frac{\partial I_0^1}{\partial x}=-k_0'(1-\omega'g')I_x^1-\frac{3}{4}k_0'\omega'g'\nu_0\cos\varphi_0HF_0e^{-k_0'z/\mu_0}\ , \tag{3.39}$$

$$\frac{\partial I_0^1}{\partial y}=-k_0'(1-\omega'g')I_y^1-\frac{3}{4}k_0'\omega'g'\nu_0\sin\varphi_0HF_0e^{-k_0'z/\mu_0}\ , \tag{3.40}$$

$$\frac{\partial I_0^1}{\partial z}=-k_0'(1-\omega'g')I_z^1+k_0'[\cos(ax)+\cos(by)][-(1-\omega'g')I_z^0+$$
$$+\frac{3}{4}\omega'g'\mu_0F_0e^{-k_0'z/\mu_0}]-\frac{3}{4}k_0'\omega'g'\mu_0HF_0e^{-k_0'z/\mu_0}\ . \tag{3.41}$$

Differentiating Eq.(3.39) with respect to x, Eq.(3.40) with respect to y and Eq.(3.41) with respect to z, and using Eqs.(3.14) and (3.38) yields

$$\nabla^2I_0^1-\lambda^2I_0^1=[\cos(ax)+\cos(by)][2\lambda^2I_0^0-2he^{-k_0'z/\mu_0}]+hHe^{-k_0'z/\mu_0}\ , \tag{3.42}$$

where $h=\frac{3}{4}(1+g'-\omega'g')\omega'k_0'^2F_0$. Eq.(3.42) is solved (see Appendix A) to obtain I_0^1, and then I_x^1, I_y^1 and I_z^1 can be derived from Eqs.(3.39),(3.40) and (3.41) respectively.

The total downward and upward diffuse irradiances are given to first order in ϵ by

$$F^{\downarrow}=F^{0\downarrow}+\epsilon F^{1\downarrow}=\pi[I_0^0(x,y,0)+\frac{2}{3}I_z^0(x,y,0)]+\epsilon\pi[I_0^1(x,y,0)+\frac{2}{3}I_z^1(x,y,0)]\ , \tag{3.43}$$

$$F^{\uparrow}=F^{0\uparrow}+\epsilon F^{1\uparrow}=\pi[I_0^0(x,y,z_0)-\frac{2}{3}I_z^0(x,y,z_0)]+\epsilon\pi[I_0^1(x,y,z_0)-\frac{2}{3}I_z^1(x,y,z_0)]\ . \tag{3.44}$$

The required boundary conditions are that the downward directed diffuse irradiance at the top of the cloud layer is zero and that the upward directed diffuse irradiance at the bottom of the cloud layer is zero. Taking into account the boundary conditions for the plane-parallel approximation (Eqs.(3.24) and (3.25)), we require from Eqs.(3.43) and (3.44) that:

$$I_0^1(x,y,0)+\frac{2}{3}I_z^1(x,y,0)=0\ , \tag{3.45}$$

$$I_0^1(x,y,z_0)-\frac{2}{3}I_z^1(x,y,z_0)=0\ . \tag{3.46}$$

Since $\cos(ax), \cos(by), \sin(ax)$ and $\sin(by)$ are orthogonal to each other, Eqs.(3.45) and (3.46) yield four groups of conditions which determine the constants C_1, D_1; C_2, D_2; C_3, D_3; and C_4, D_4 (see Appendix A).

The net diffuse irradiance vector (Goody and Yung, 1989) is

$$\mathbf{F} = F_x \mathbf{e_x} + F_y \mathbf{e_y} + F_z \mathbf{e_z} \,, \tag{3.47}$$

where $F_x = \frac{4}{3}\pi(I_x^0 + \epsilon I_x^1), F_y = \frac{4}{3}\pi(I_y^0 + \epsilon I_y^1)$, and $F_z = \frac{4}{3}\pi(I_z^0 + \epsilon I_z^1)$.

The net direct solar irradiance vector is

$$\mathbf{F}^d = F_x^d \mathbf{e_x} + F_y^d \mathbf{e_y} + F_z^d \mathbf{e_z} \,, \tag{3.48}$$

where $F_x^d = \nu_0 \cos\varphi_0 \pi F_0 e^{-\tau} \approx (1 - \epsilon H)\nu_0 \cos\varphi_0 \pi F_0 e^{-k_0' z/\mu_0}$,

$F_y^d \approx (1 - \epsilon H)\nu_0 \sin\varphi_0 \pi F_0 e^{-k_0' z/\mu_0}$, and $F_z^d \approx (1 - \epsilon H)\mu_0 \pi F_0 e^{-k_0' z/\mu_0}$.

Therefore the heating rate is given by

$$\frac{\partial T}{\partial t} = -\frac{1}{c_p \rho} \nabla \cdot (\mathbf{F} + \mathbf{F}^d) = \frac{1}{c_p \rho} \pi (1 - \omega') k' [4I_0^0 + F_0 e^{-k_0' z/\mu_0}]$$

$$+ \frac{\epsilon}{c_p \rho} \pi (1 - \omega') k_0' [4I_0^1 - H F_0 e^{-k_0' z/\mu_0}] \,, \tag{3.49}$$

where c_p is the specific heat and ρ is the air density. Eq.(3.49) gives the distributions of the heating rate inside the cloud layer.

3.3 Results and discussions

We have derived the diffuse radiance for a horizontal periodic inhomogeneous medium using the first order perturbation method. If the perturbation coefficient ϵ is small enough, the errors due to the higher order contributions are very small.

The reflection for solar irradiance (cloud albedo) is defined as

$$\alpha = F^{\uparrow}(0)/\mu_0 \pi F_0 \,. \tag{3.50}$$

The solution shows that the slight horizontal periodic variation of the extinction coefficient makes the radiance also a periodic function, although the periodic form of the

radiance is more complicated than that of the extinction coefficient. Therefore, the horizontally averaged cloud albedo is the same as for the plane-parallel homogeneous case, since the horizontal average of the periodic form of the first order perturbation correction is zero. In our solution, no approximation has been used except that of Eddington and the perturbation method itself, but because the perturbation is only up to the first order, the results can not be considered as exact. However, since the higher order corrections are usually very small for a small perturbation coefficient, we conclude that the plane-parallel is a good approximation for the horizontally averaged cloud albedo regardless of the consideration of the small internal horizontal inhomogeneity of clouds.

The zero change in the horizontally averaged cloud albedo compared to the plane-parallel homogeneous case does not mean that the first order perturbation solution is without significance. The local spatial distribution of radiance field may affect the local and even the large scale climate system. The cloud radiation interaction is an important factor for the nonlinearity of climate, which contains chaotic tendencies. In a nonlinear chaotic system, small scale variability can modulate significantly the overall state of the system. Locally, the distributions of solar radiance field and heating rate play an important role for the local energy balance. They influence the infrared radiation and the thermal circulation. The spatial distribution of radiance is also important for remote sensing, since the observation image of a cloud is determined by the distribution of the diffuse radiance field.

Consider a layer of a typical stratocumulus cloud with extinction coefficient $k_0 \sim 50\,km^{-1}$, and cloud droplet asymmetry factor $g \sim 0.86$. The single scattering albedo is largely dependent on the solar wavelength; in the following we choose ω between 0.98-0.999.

We first examine the horizontal distribution of the extinction coefficient $k' = k'_0\{1 + \epsilon[\cos(ax) + \cos(by)]\}$. Let $a = b = 2\pi/L$, where L is the length of a period of the cosinusoidal cloud field. Taking $\epsilon = 0.1$, $g = 0.86$, $\omega = 0.999$ and $k_0 = 50\,km^{-1}$, the scaled k'_0 is determined by Eq.(3.8). In Fig.3.2 the two dimensional distribution

of the scaled extinction coefficient is shown for one period.

In the following, the behaviours of radiance field and cloud heating rate related to the horizontally inhomogeneous cloud field shown in Fig.3.2 will be investigated.

3.3.1 The distribution of the radiance field

Fig.3.3 gives the distributions of upwelling radiative intensities ($I(\mu = -1)$) at the top of a cloud corresponding to the extinction coefficient shown in Fig.3.2. The solar zenith angle $\theta_0 = 0^0$, the cloud thickness $z_0 = 500\,m$, and the scattering factors are the same as those in Fig.3.2. From Fig.3.3a to 3.3c, different values of cloud periodic length L are considered.

In Fig.3.3, although the cloud scattering properties and cloud depth are the same, the distributions of the upwelling radiative intensities are quite different for different cloud periodic lengths. Comparing Fig.3.2 with Fig.3.3a, there exists an explicit correlation in the distributions of the extinction coefficient and the upwelling intensity with the configuration of the distribution of the upwelling intensity being similar to the configuration of the distribution of the extinction coefficient. This is as expected. The smaller the extinction coefficient, the smaller the cloud reflection, since it is easier for the photons to pass through the cloud. We call the distribution of upwelling intensity in Fig.3.3a a correlated distribution.

Comparing Fig.3.2 with Fig.3.3b and 3.3c there also exist clear correlations between the distributions of the extinction coefficient and the upwelling intensities. However, the configurations of the distributions of the upwelling intensities are opposite to the configuration of the distribution of the extinction coefficient. We call these distributions of upwelling intensities anti-correlated distributions.

To understand why the anti-correlated distributions happen, we have plotted in Fig.3.4 the one dimensional cross sections ($y = 0$) of the distributions of the upwelling intensities at different heights inside the cloud. The periodic lengths of $L = 200\,m$ and $L = 1000\,m$ are considered. At the height of $z = 100\,m$ (down from the top of the cloud), the distributions of the upwelling intensities are quite similar for both

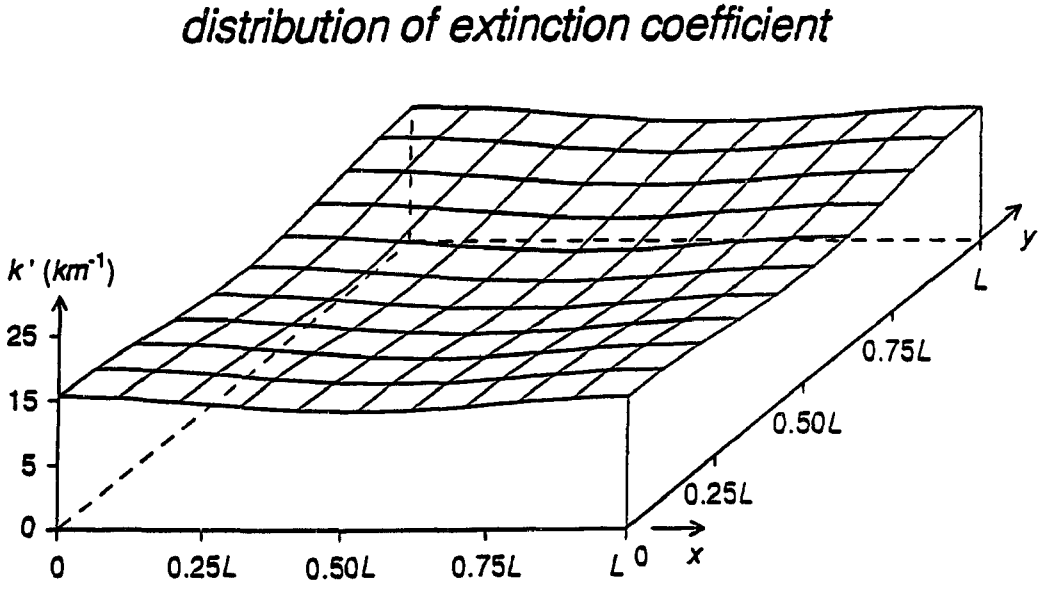

Figure 3.2: Two dimensional distribution of the scaled extinction coefficient in a periodic region with the periodic length L. $k_0 = 50\,km^{-1}$, $g = 0.86$ and $\omega = 0.999$.

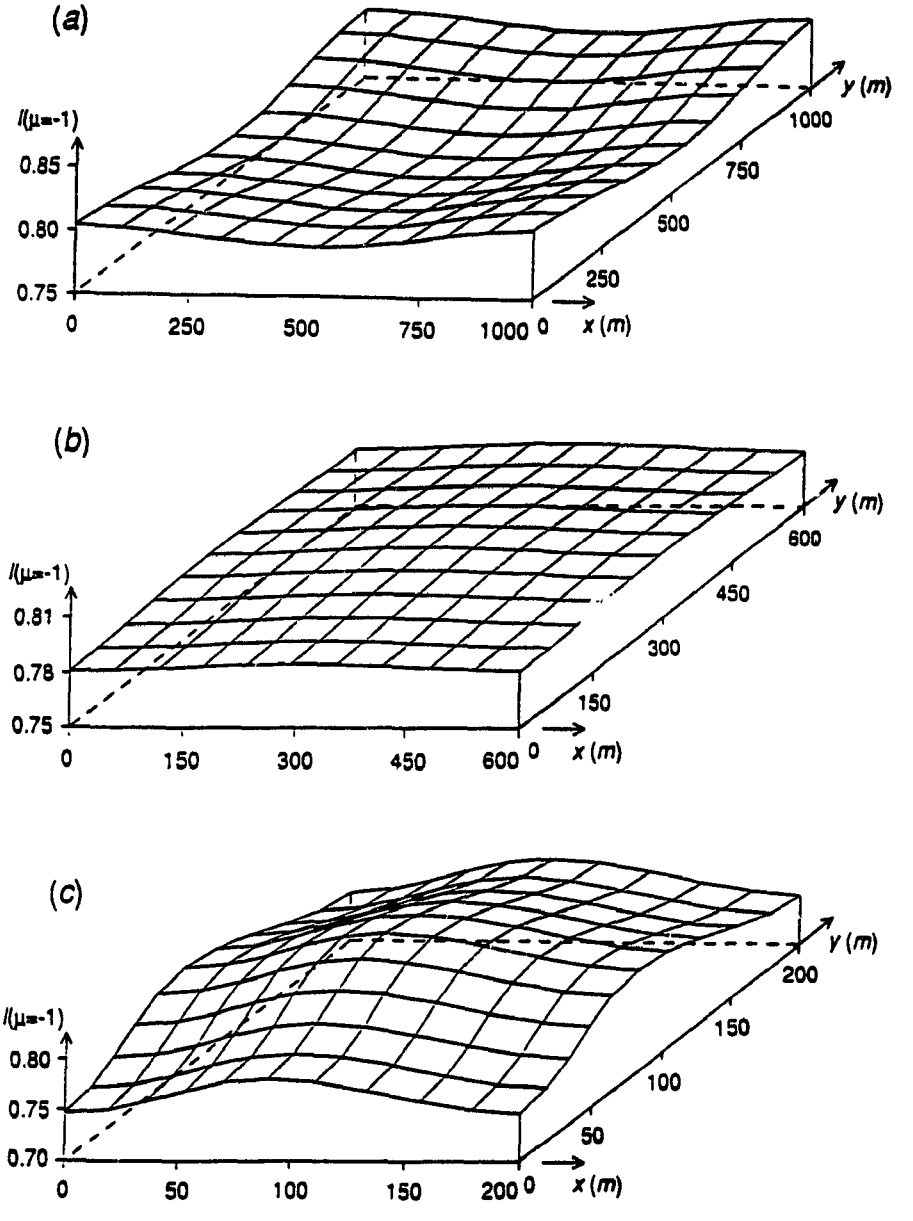

Figure 3.3: Two dimensional distributions of upwelling intensities with different periodic lengths: (a) $L = 1000\,m$, (b) $L = 600\,m$, (c) $L = 200\,m$. Solar zenith angle $\theta_0 = 0°$. The intensity unit is normalized with respect to $\mu_0 F_0$.

the cases of $L = 200\,m$ and $L = 1000\,m$. The upwelling intensities are less in the central region. This is because, the smaller the extinction coefficient, the smaller the probability of a photon being scattered or absorbed, resulting in fewer reflected photons in this region. As the reflected photons travel upward through the cloud, more rising diffuse photons produced by the scattering of the direct solar beam are added, increasing the upwelling intensity (see Fig.3.4).

Since the cloud droplet asymmetry factor is about 0.86, it is possible that a photon would deviate from its transport direction after a scattering event. If the upward travelling photons enter the central region from the side regions (see Fig.3.4), because of the smaller absorption and fewer scattering events in the central region, photons are more easily transported upward. On the other hand, if the upward travelling photons enter the side regions from the central region, because of the larger absorption and more scatterings in the side regions, the photons are more likely to be trapped or to be scattered into a new direction. Then the probability of going downward is enhanced. Therefore, the diffuse photons travelling upward have the tendency of "leaking" horizontally in the cloud from regions of higher extinction coefficient to regions of lower extinction coefficient. This is demonstrated in Fig.3.4a, from $z = 250\,m$ to $z = 0\,m$ (top of the cloud), the upwelling intensities in the central region increase faster than that in the side regions.

If the length of the horizontal period of cloud is large, the interaction between the regions of different extinction coefficients is weak. The number of the horizontally "leaking" photons is not enough to completely change the configuration of the distribution of the upwelling intensity. Therefore, the correlated distribution appears (Fig.3.3a). For Fig.3.3b the number of the horizontal "leaking" photons is just large enough to reverse the correlated distribution. The configuration of the distribution is very smooth.

In order to describe succinctly the dependence of the upwelling intensity at the top of the cloud on the various cloud parameters, we define a relative fluctuation for

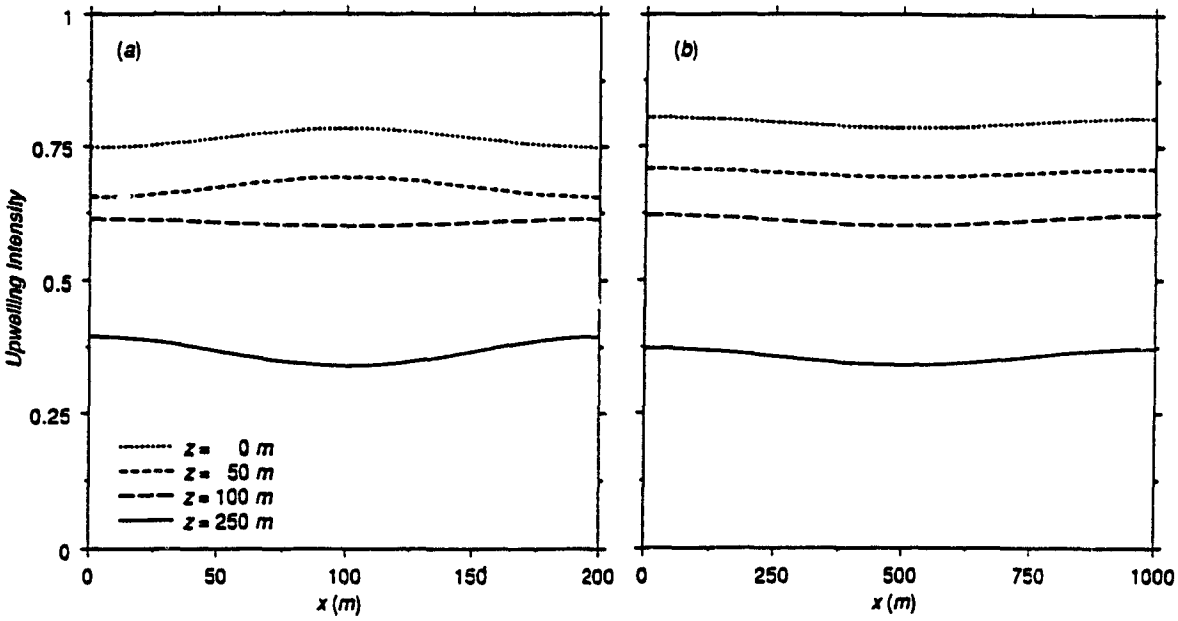

Figure 3.4: One dimensional distributions of the upwelling intensities on the line ($y = 0$) at different heights. (a) $L = 200\,m$; (b) $L = 1000\,m$. Solar zenith angle $\theta_0 = 0°$. The intensities are normalized with respect to $\mu_0 F_0$.

the distribution of upwelling intensity as

$$P = \frac{I_a(\mu = -1) - I_b(\mu = -1)}{\frac{1}{2}(I_a(\mu = -1) + I_b(\mu = -1))} \tag{3.51}$$

where $I_a(\mu = -1)$ is the upwelling intensity at the top of the cloud with the maximum vertical optical depth (such as the point $(x = 0, y = 0)$ in Fig.3.2), and $I_b(\mu = -1)$ is the upwelling intensity at the top of the cloud with minimum vertical optical depth (such as the central point $(x = \frac{L}{2}, y = \frac{L}{2})$ in Fig.3.2). $P > 0$ represents a correlated distribution and $P < 0$ represents an anti-correlated distribution.

Fig.3.5a shows P as a function of the periodic length L. The other parameters are all the same as those in Fig.3.3. For large values of L, P increases slowly with the increase of L to a limit value. The value of P is very close to zero for L near $600\,m$. This is the case illustrated in Fig.3.3b, in which the distribution is very smooth. The minimum value of P is near $L = 200\,m$. This is the case illustrated in Fig.3.3c, in which the anti-correlated distribution has a large amplitude of fluctuation. Then, if L decreases further, P increases again. When the horizontal periodic length of the cloud field is close to the free path length of photons, the photons can travel through an entire period of the cloud field between two scattering events. Therefore the regional difference decreases for the diffuse photons, and the relative fluctuation is reduced.

We find that the correlated or anti-correlated distribution is also sensitive to the cloud depth. Fig.3.5b shows the variation of P with the cloud depth z_0. The other parameters are all the same as those used in Fig.3.3b. As cloud depth increases, P decreases. This is because the average geometric path length that the reflected photons undergo is larger for a thick cloud than for a shallow one. Therefore the interaction between different regions is stronger, and photons have a larger chance to "leak" from a region with a larger extinction coefficient to a region with a smaller extinction coefficient. The anti-correlated distributions are more likely to occur.

Fig.3.5c shows P as the function of the extinction coefficient. The other parameters are all the same as those used in Fig.3.3a. We find the anti-correlated distribution is more likely to occur with smaller extinction coefficients. The smaller the extinction coefficient, the larger the mean path length. Therefore, the diffuse photons are easier

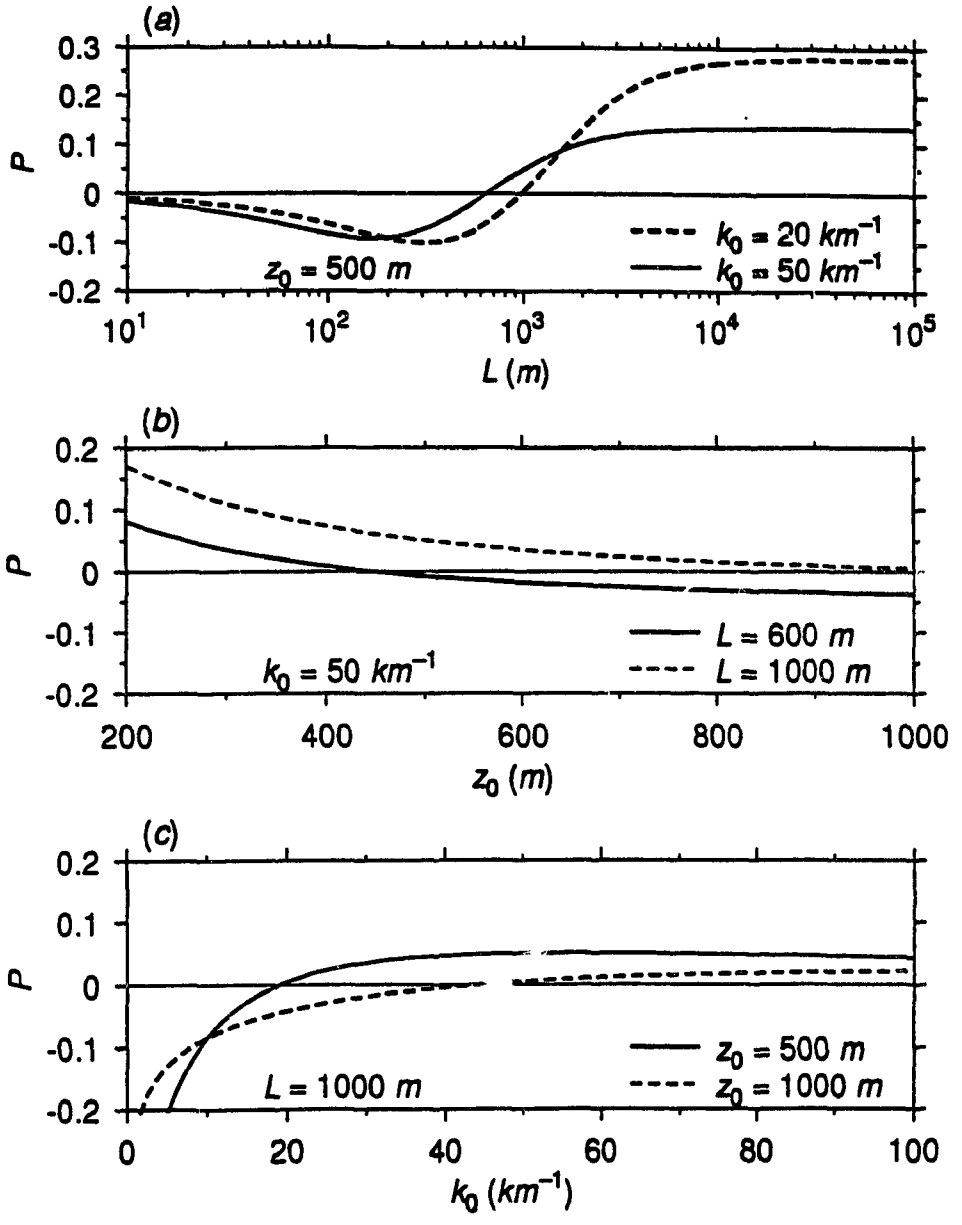

Figure 3.5: The relative fluctuation as a function of: (a) periodic length L, (b) cloud depth z_0, (c) extinction coefficient k_0. $g = 0.86$ and $\omega = 0.999$. Solar zenith angle $\theta_0 = 0°$.

to transport through regions with different extinction coefficients. The interaction between different regions becomes stronger and the "leaking" effect becomes larger.

3.3.2 Shift phenomenon

Reconsider the configurations of distribution of upwelling intensity in Fig.3.3 but with the solar zenith angle changed to $\theta_0 = 60^0$, and let $\varphi_0 = 0$, keeping the other parameters the same as those in Fig.3.3. Then the resulting distributions of the upwelling intensities are shown in Fig.3.6. We find that all of the configurations of the distribution for upwelling reflected intensity are distorted from those in Fig.3.3. In Fig.3.3 the upwelling intensities are symmetric with respect to the central points in x and y directions. However, from Fig.3.6a to 3.6c the symmetry in x direction is lost. Upwelling intensities are larger on the right hand side of the regions. For example in Fig.3.6c the raised region of the upwelling intensity is shifted to the positive x direction. In the y direction the symmetric distribution is preserved.

To show clearly the shift of the raised region in the distribution of the upwelling intensity, the one dimensional cross sections ($y = 0$) of the intensity are shown in Fig.3.7, for zenith angles $\theta_0 = 30^0$, 45^0, and 60^0. The other parameters are the same as those in Fig.3.6c. The raised regions of the distribution for the upwelling intensity are shifted towards the positive x direction, and the shift increases with increasing solar zenith angle. The direction of the shift is always along the direct solar beam direction. If we keep $\theta_0 = 60^0$, and switch the azimuth angle to $\varphi_0 = 90^0$, the shift direction would be towards the positive y direction. A similar shift in the distribution of intensity occurs in other directions. Later we will discuss the situation of downwelling intensity.

It is seen from Fig.3.7 that the shift is proportional to the solar zenith angle and is always along the direct solar beam direction. Therefore, the declination of the direct solar beam is naturally thought to be an important factor for the shift phenomenon. In Fig.3.8, one dimensional distributions ($y = 0$) of the vertical direct solar fluxes ($F_z^d = (1 - \epsilon H)\mu_0 \pi F_0 e^{-k_0' z/\mu_0}$) at different heights are shown, taking

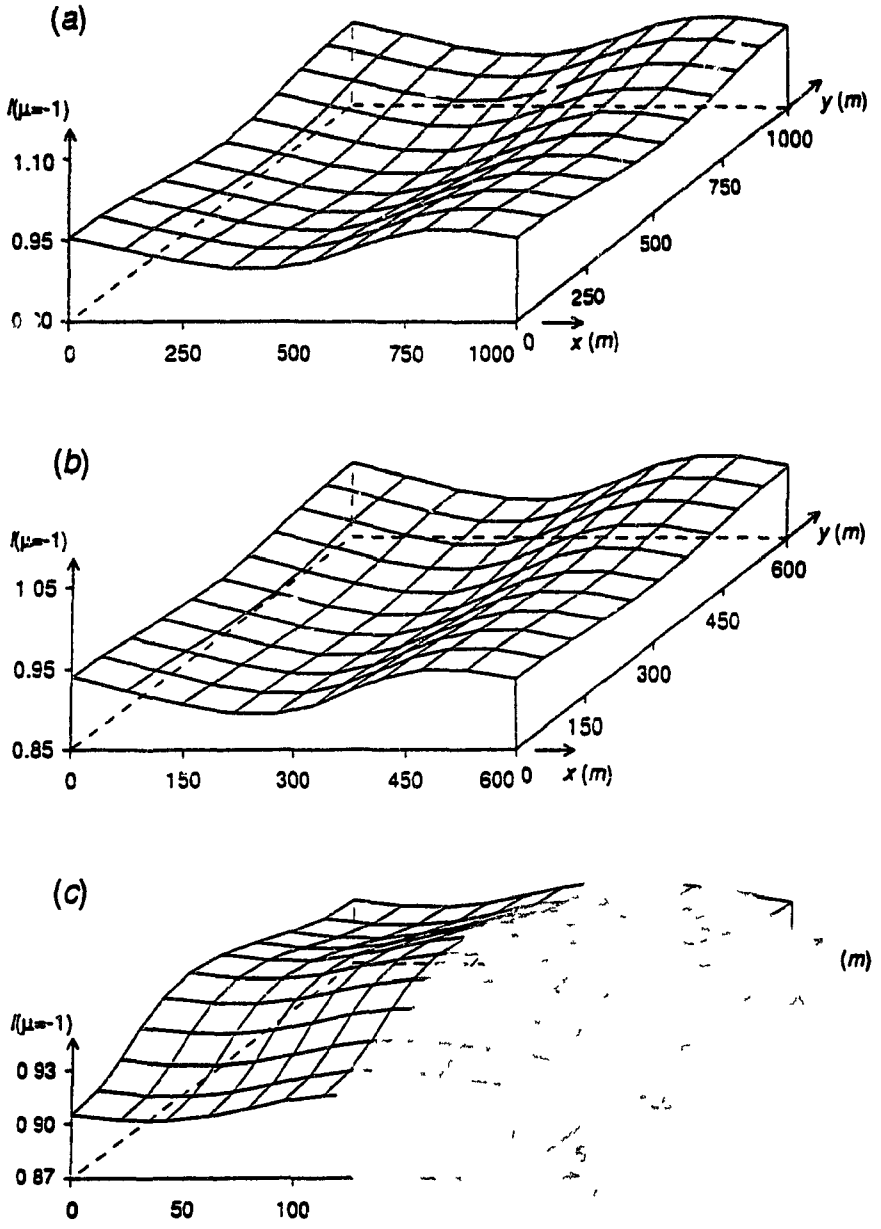

Figure 3.6: Two dimensional distributions of upwelling intensities with different periodic lengths: (a) $L = 1000\,m$, (b) $L = 600\,m$, (c) $L = 200\,m$. Solar zenith angle $\theta_0 = 60°$. The intensity unit is normalized with respect to $\mu_0 F_0$.

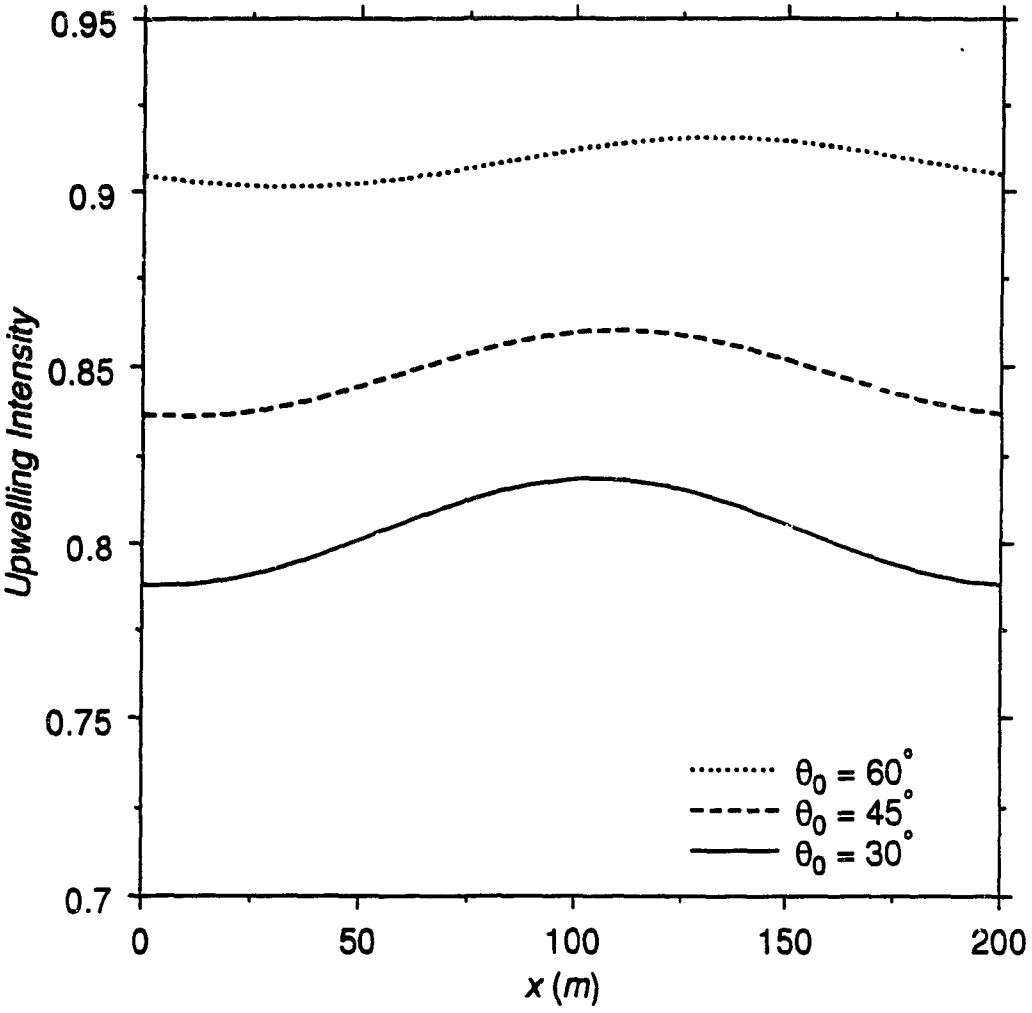

Figure 3.7: One dimensional distributions of upwelling intensities on the line ($y = 0$) with different solar zenith angles. The intensities are normalized with respect to $\mu_0 F_0$.

$\pi F_0 = 340\, W/m^{-2}$ and the other parameters as in Fig.3.6c. Near the top of the cloud ($z = 10\, m$, down from the top), the distribution of the direct solar flux is larger in the central region, which is due to Beer's law, and the distribution is nearly symmetric in the x direction. As the depth z increases, the shift in the distribution of the direct solar flux increases. Since the incident solar beam is now inclined towards larger values of x, for any two points symmetric to the center point ($x = 100\, m$) with the same height, the optical paths for the two points are different. Therefore the symmetric distribution is lost. From the geometric consideration, for $\theta_0 = 60^0$, $\varphi_0 = 0$, and $L = 200\, m$, the largest shift should happen at the height of $z = L/2\tan\theta_0 = 57.7\, m$. Then, as z increases further, the shift would decrease. In Fig.3.8, for $z = 100\, m$, the distribution becomes nearly completely homogeneous. When $z = L/\tan\theta_0 = 115\, m$, each ray has passed one period in variation of the extinction coefficient, and there is no difference in the optical path for each ray.

The regional asymmetric distribution for the direct solar beam will then make the distribution of the diffuse photons produced by the scatterings of the direct solar beam also regionally asymmetrical. The multiple scattering process acts to suppress the inhomogeneous distribution of such diffuse photons. Since more scatterings would happen in the region with more diffuse photons, this would allow the photons to have a greater chance of leaving this region. However, if the diffuse photons do not undergo a large number of multiple scatterings, the regional inhomogeneous distribution can be largely preserved in the outgoing diffuse photons. The shift phenomenon appears. Therefore, the shift effect is due to the interrelation between the diffuse photons and the direct solar beam.

Next, we consider the influences of the scattering factors on the distributions of the diffuse radiative intensities. In Fig.3.9, the upwelling intensities are plotted for different values of the asymmetry factor. All other parameters are the same as those used in Fig.3.6c. We find the shift is smaller with a larger asymmetry factor. In the case of a larger asymmetry factor, the scattering is concentrated in a more narrow angle in the forward direction of the incident photons, in comparison with the case

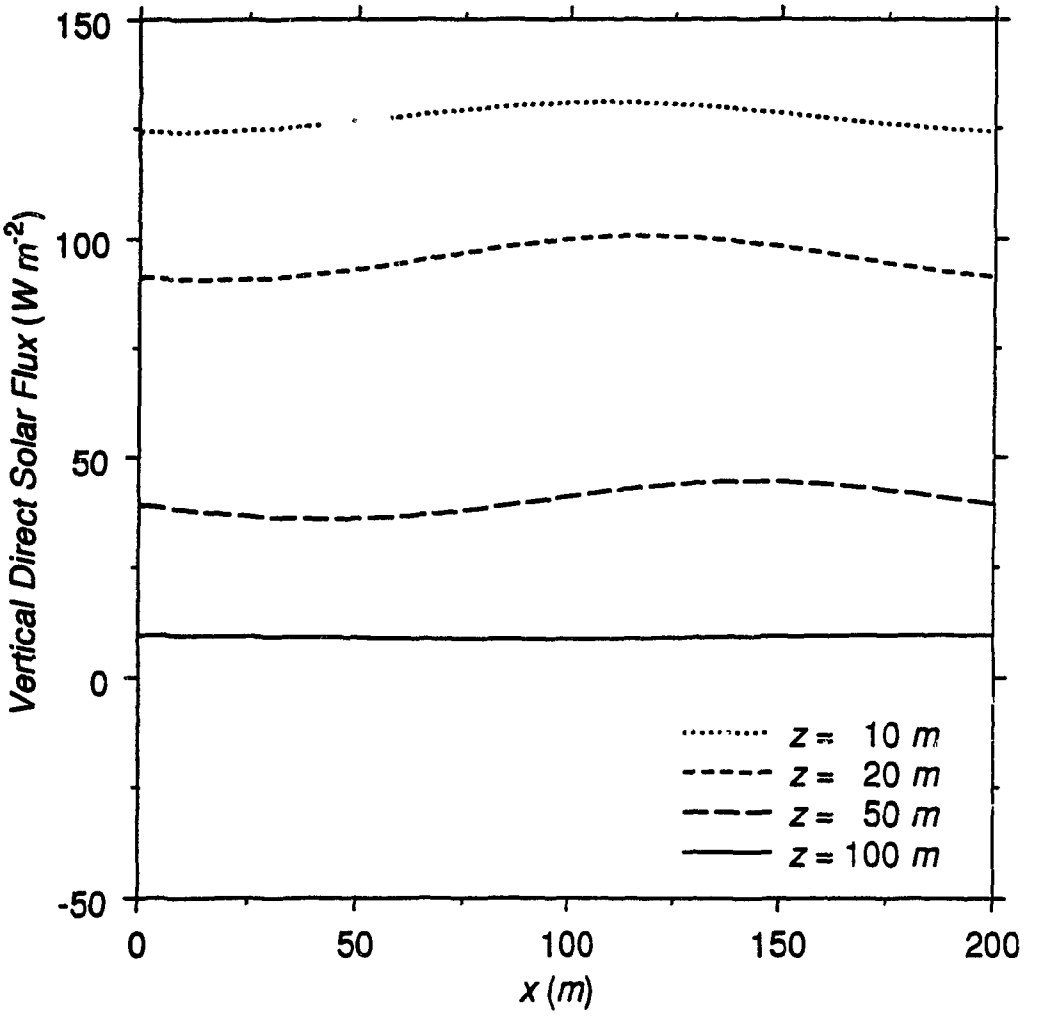

Figure 3.8: One dimensional distributions of vertical direct solar flux on the line ($y = 0$) at different heights. Solar zenith angle $\theta_0 = 60°$. $\pi F_0 = 340\, W\, m^{-2}$.

of a smaller asymmetry factor. Therefore the diffuse photons produced by the first scattering with the solar beam have a larger tendency to go downward. Then the final reflected diffuse photons must have undergone more multiple scatterings. The spatially asymmetric distribution for the diffuse photons is more largely suppressed by the multiple scattering processes, and the shift is reduced.

We can explore this point further by considering the distribution of downwelling intensity. Fig.3.10 presents the distributions of downwelling intensities with different values of asymmetry factor. All parameters for the cloud are the same as those used in Fig.3.6c except for the cloud depth which is taken to be $120\,m$. In Fig.3.10, the distribution of the downwelling intensity is opposite to that of the upwelling intensity in Fig.3.9. The shift effect is larger for a larger asymmetry factor. As we discussed above the larger asymmetry factor makes the diffuse photons more likely to pass through the bottom of the cloud, and suffer less multiple scattering. The regional inhomogeneous distribution is preserved more in the final transmitted diffuse photons. For this discussion of downwelling intensity, the cloud depth was taken to be only $120\,m$, since the shift phenomenon would disappear for a very thick cloud. The mean path length of a photon is $20\,m$ for the extinction coefficient $k_0 = 50\,km^{-1}$. In the case of Fig.3.10, if the cloud depth is $500\,m$, on average a photon should be scattered at least 50 times by cloud droplets before it passes through the cloud base. This large number of scatterings results in the regional asymmetric distribution of the diffuse photons being completely lost.

The cloud diffuse reflection intensity is very sensitive to the value of the single scattering albedo. In Fig.3.11, the distributions of upwelling intensities are plotted with different single scattering albedos, keeping the other parameters the same as those in Fig.3.6c. The diffuse upwelling intensity is larger for a larger single scattering albedo. The relative fluctuation of the distribution of upwelling intensity also increases as the single scattering albedo increases, and the shift effect is larger with a smaller single scattering albedo.

If a photon has undergone n scattering events, the probability of being absorbed by

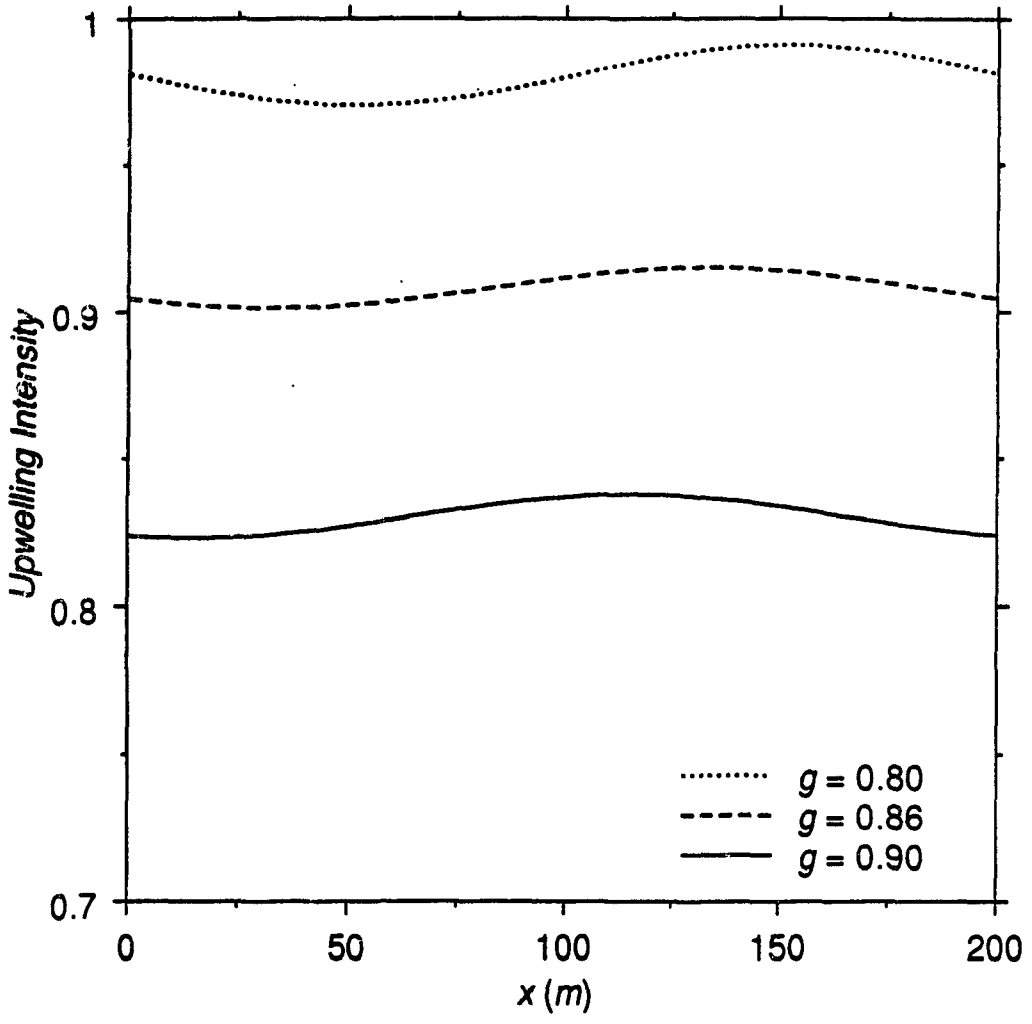

Figure 3.9: Upwelling intensities on the line ($y = 0$) with different asymmetry factors. Cloud thickness $z_0 = 500\,m$. Solar zenith angle $\theta_0 = 60°$. The intensities are normalized with respect to $\mu_0 F_0$.

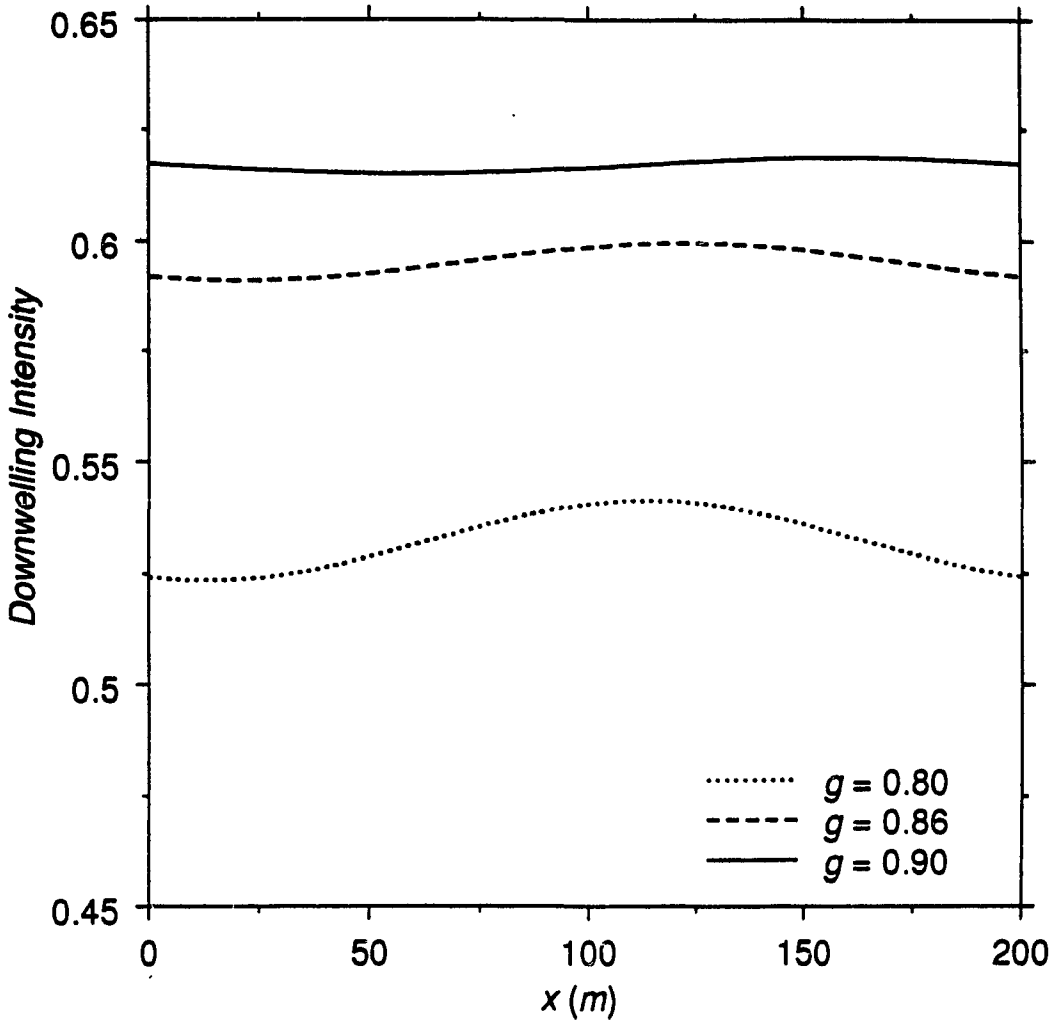

Figure 3.10: Downwelling intensities on the line ($y = 0$) with different asymmetry factors. Cloud thickness $z_0 = 120\,m$. Solar zenith angle $\theta_0 = 60°$. The intensities are normalized with respect to $\mu_0 F_0$.

cloud droplets is $1-\omega^n$. For a smaller single scattering albedo, the photons that have undergone a large number of scatterings are more likely to be absorbed; therefore, on average the reflected diffuse photons have suffered a less number of scattering events in comparison with the case of a larger single scattering albedo. Thus the regional asymmetric distribution of the diffuse photons is more largely preserved.

Although we have only investigated the shift phenomenon in the anti-correlated distribution cases, the discussion can be extended to the correlated distribution cases. In Fig.3.6a, the lowered region is shifted to the negative x direction relative to Fig.3.3a. The distribution of the upwelling intensity is anti-correlated in Fig.3.3b. However, it becomes correlated in Fig.3.6b. The delicate balance in regional distribution of the diffuse photons is easy lost for a large solar zenith angle. Also, the intensity distribution is shifted.

3.3.3 Distribution of cloud heating rate

The heating rate inside the cloud layer is given by Eq.(3.49). With parameters stated in Fig.3.6c and $\pi F_0 = 340\, Wm^{-2}$, we calculated the heating rates inside the cloud at different heights down from the cloud top. In Fig.3.12 only the one dimensional distributions ($y = 0$) are shown. Besides the case of zenith angle $\theta_0 = 60^0$ (Fig.3.12a), zenith angle $\theta_0 = 45^0$ is also considered (Fig.3.12b). In comparing with Fig.3.2, the correspondence in the distributions of the heating rates and the extinction coefficient is clear. There are no anti-correlated distributions in the cloud heating rates. If the cloud layer is homogeneous, the local cloud solar heating rate is proportional to the extinction coefficient. In the case of horizontally inhomogeneous cloud, the local cloud heating rate is also proportional to the local extinction coefficient (the first term in Eq.(3.49)); however another term is added due to the inhomogeneity of the cloud. The cloud heating rate is dominated by the first term, since the second term is a pure perturbation term. Because of the existence of the second term, the deviation from the distribution extinction coefficient is expected to appear in the distribution of cloud heating rate for a large solar zenith angle.

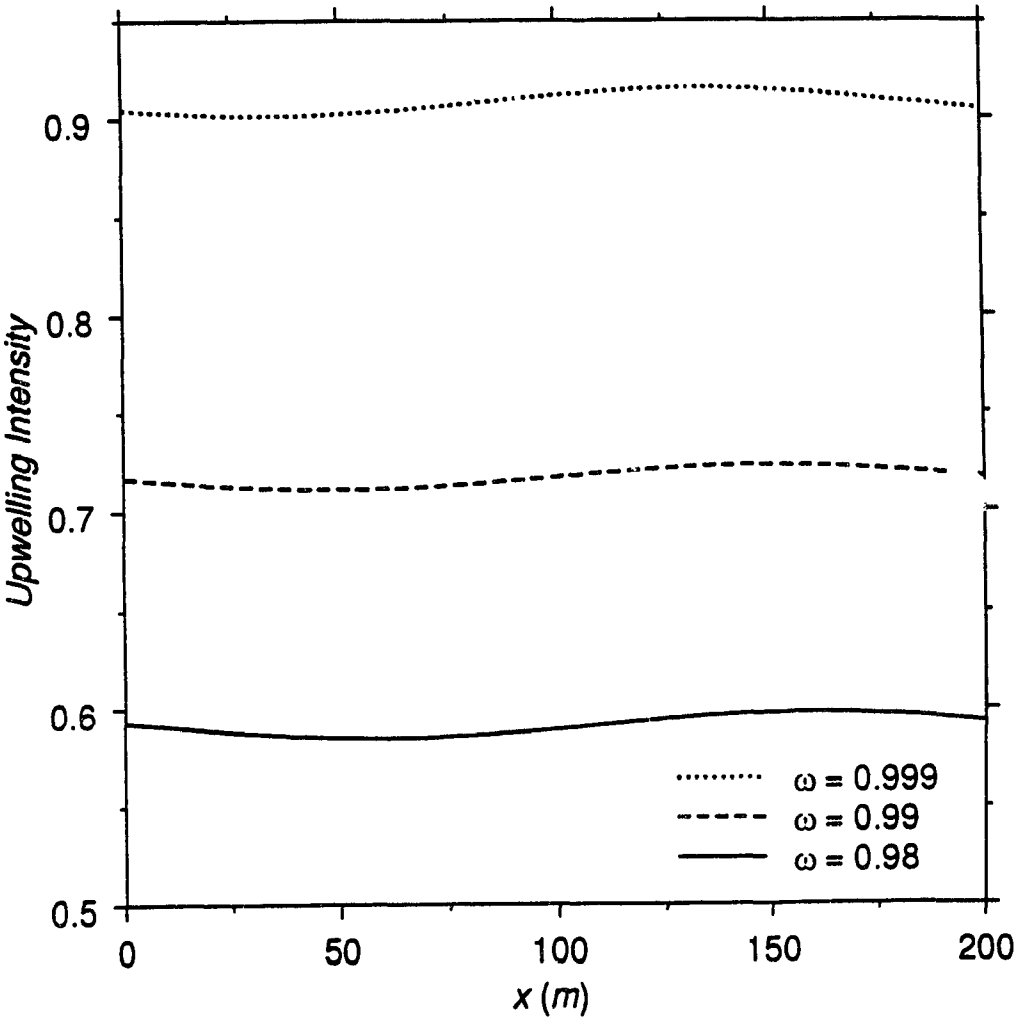

Figure 3.11: Upwelling intensities on the line ($y = 0$) with different single scattering albedos. Solar zenith angle $\theta_0 = 60°$. The intensities are normalized with respect to $\mu_0 F_0$.

As illustrated in Fig.3.8, for the vertical direct solar flux, the distribution is quite symmetric near the top of the cloud. The strong shifts happen near $z = 50\,m$. The distribution of the direct solar flux would affect the distribution of the diffuse photons. Since the heating rate is dependent on the local difference (divergence) of the total net flux, not directly associated with the total net flux, we find in Fig.3.12 the shifts in the distributions of the local heating rate are much reduced in comparison with that in Fig.3.8. For $\theta_0 = 45^0$, the maximum shift in the distribution of the vertical direct solar flux should happens at the height of $z = 100\,m$. In Fig.3.12b, the maximum shift in the distribution of heating rate also happens at the height of $z = 100\,m$.

The heating rate is the source term of the infrared radiation. Therefore, for a large solar zenith angle, inside the cloud and especially in the upper part of the cloud, the solar irradiance and the infrared irradiance are different in distribution. To balance the energy flow, the cloud would undergo thermal circulation. This effect may contribute to the small scale convection and turbulence in the upper part of clouds.

3.4 Summary

Using the first order perturbation method, an analytical solution of the 3-D radiative transfer equation in a horizontally inhomogeneous medium with a cosinusoidal distribution of extinction coefficient has been obtained. The solution shows that the horizontally averaged cloud albedo is equal to the plane-parallel results. This is a special feature of first order perturbation solution. However, even the first order perturbation calculation of the spatial distribution of diffuse intensity contains valuable information not previously available. Our study has been restricted to the cosinusoidal periodic variation of the extinction coefficient. However, we can conclude that for other forms of periodically weakly inhomogeneous cloud, the horizontally averaged results are close to that of the plane-parallel, since any periodic function can be expanded in a series of cosinusoidal functions with different modes. Our solution is

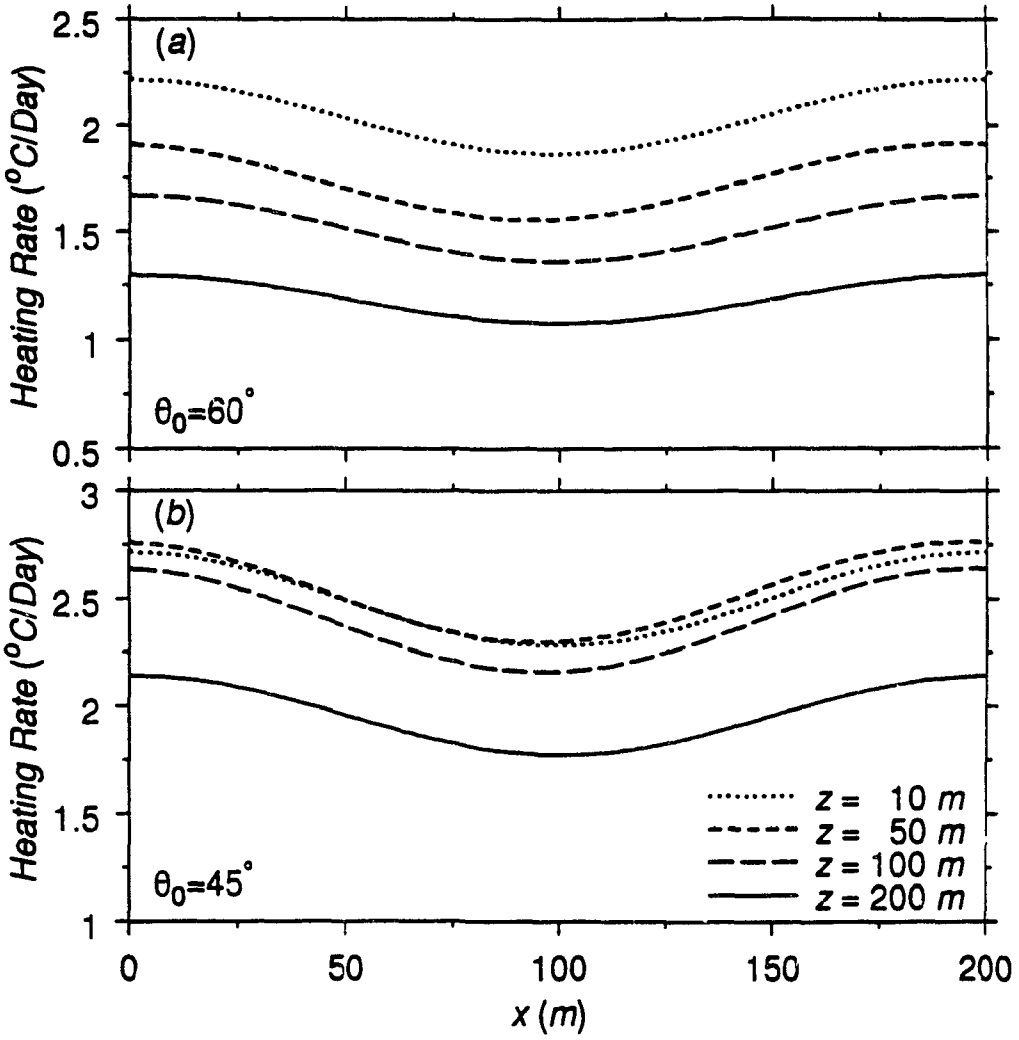

Figure 3.12: One dimensional distributions of heating rates on the line ($y = 0$) at different heights. $\pi F_0 = 340\, W\, m^{-2}$. (a) Solar zenith angle $\theta_0 = 60°$; (b) $\theta_0 = 45°$.

just for a single mode case. The solution for multi-mode is similar, provided that the first order perturbation approach is valid. The perturbation method can be extended to more inhomogeneous cloud fields, if higher order calculations are considered.

The most interesting results in our work are the anti-correlated distribution of the diffuse radiative intensity and the horizontal shift in the distribution of diffuse radiative intensity, relative to the extinction coefficient. These phenomena may have significant implications for the interpretation of aircraft soundings of solar radiation. The anti-correlated distribution of the diffuse radiative intensity is due to the horizontal "leaking" of photons through regions of larger extinction coefficient to regions of smaller extinction coefficient. The shift effect is caused by the external solar source term. When the solar zenith angle is large, the asymmetry in the regional distribution of the diffuse photons produced by scattering with the direct solar beam results in a shift in the distribution of the outgoing diffuse photons. This argument has been verified by the examination of the dependence of the distribution of the diffuse intensity on the scattering factors. The heating rate is mostly characterized by the local extinction coefficient and does not exhibit any anti-correlated distributions.

Chapter 4

Second Order Perturbation Solution for Radiative Transfer in Clouds with a Horizontally Arbitrary Periodic Inhomogeneity

In chapter 3 we have used a perturbation method for solving the three dimensional radiative transfer equation in a cloud layer with a horizontal cosinusoidal variation of extinction coefficient. The most interesting results obtained in chapter 3 are the anti-correlated distribution of upwelling intensity and the shift phenomenon. These show that the apparent cloud images may not correspond to the actual distributions of the cloud internal optical properties. Chapter 3 shows that the perturbation method opens up a potentially valuable approach to the analytical solution of the 3D radiative transfer equation in a medium having internal inhomogeneity. The work needs to be improved in the following two aspects. First, since only a single mode of cosinusoidal variation of inhomogeneity has been considered in chapter 3, the work should be extended for multi-mode case. Thus a more general type of inhomogeneity can be taken into account. Second, for larger values of the perturbation coefficient ϵ the higher order perturbation corrections are required. In the first order of perturbation

theory, there is no change in the horizontally averaged cloud albedo. What happens when the higher order perturbation corrections are applied?

4.1 Perturbation solution for multi-mode case

For radiative transfer in an inhomogeneous cloud, we consider the extinction coefficient with two-dimensional horizontally periodic variations

$$k' = k'_0[1 + \epsilon f(x, y)] \,, \tag{4.1}$$

where k'_0 is the scaled value of k_0 by Eq.(3.8) and $f(x, y)$ is an arbitrary two dimensional periodic function. We expand the real perturbation function in a complex exponential Fourier series,

$$f(x, y) = \sum_{mn} L_{mn} e^{i\pi(\frac{m}{a}x + \frac{n}{b}y)} \tag{4.2}$$

where a and b are the half periodic lengths in the x direction and the y direction respectively, The expansion coefficients L_{mn} are generally complex quantities. For convenience in calculation, if there should exist a zero mode in th expansion, it can be removed by the rescaling of $k'_0(1 + \epsilon L_{00}) \to k'_0$ and $\epsilon/(1 + \epsilon L_{00}) \to \epsilon$. Any zero mode contribution is therefore rearranged into the result of the zero order unperturbed solution.

The optical depth for the direct solar beam is

$$\tau_0 = \int k'_0[1 + \epsilon f(x, y)]\, ds = k'_0 s + \epsilon H(s, \theta_0, \varphi_0) \,, \tag{4.3}$$

where the geometric path length $s = z/\mu_0$ and

$$H = \int k'_0 f(x, y)\, ds = -ik'_0 \sum_{mn} L_{mn} e^{i\pi(\frac{m}{a}x + \frac{n}{b}y)}(1 - e^{-i\xi_{mn}z})/\mu_0\xi_{mn} \,, \tag{4.4}$$

where $\xi_{mn} = \pi(\tan\theta_0 \cos\varphi_0 m/a + \tan\theta_0 \sin\varphi_0 n/b)$, μ_0 and ν_0 are the cosine and sine of solar zenith angle respectively.

Since $f(x, y)$ is expanded in complex exponentials, the corresponding radiative intensity is similarly expanded. Therefore, in the transfer equation Eq.(3.2) we have

$(I, J, J_0) \rightarrow (\tilde{I}, \tilde{J}, \tilde{J}_0)$ for the corresponding quantities with complex expansion coefficients. Finally, after the transfer equation being solved, the resultant radiative intensity is obtained by $I = \mathrm{Re}\tilde{I}$.

The direct solar flux in the external source term can be expanded as

$$\pi F_0 e^{-k_0' s - \epsilon H} \approx (1 - \epsilon H + \frac{1}{2}\epsilon^2 H^2)\pi F_0 e^{-k_0' s} . \tag{4.5}$$

The accuracy of this expansion has been discussed in previous chapter.

Substituting the expansion in Eq.(4.5) into Eq.(3.5), $\tilde{J}_0$ therefore can be written as

$$\tilde{J}_0 = \tilde{J}_0^{(0)} + \epsilon \tilde{J}_0^{(1)} + \epsilon^2 \tilde{J}_0^{(2)} . \tag{4.6}$$

Expanding also the radiance $\tilde{I}$ in powers of ϵ,

$$\tilde{I} = \tilde{I}^{(0)} + \epsilon \tilde{I}^{(1)} + \epsilon^2 \tilde{I}^{(2)} . \tag{4.7}$$

Consequently,

$$\tilde{J} = \tilde{J}^{(0)} + \epsilon \tilde{J}^{(1)} + \epsilon^2 \tilde{J}^{(2)} , \tag{4.8}$$

which is obtained from Eq.(3.4). Substituting Eqs.(4.6), (4.7) and (4.8) into Eq.(3.2) and regrouping the terms with the same order of ϵ, we obtain

$$\frac{d\tilde{I}^{(0)}}{ds} = k_0'(-\tilde{I}^{(0)} + \tilde{J}^{(0)} + \tilde{J}_0^{(0)}) , \tag{4.9}$$

$$\frac{d\tilde{I}^{(1)}}{ds} = k_0'(-\tilde{I}^{(1)} + \tilde{J}^{(1)} + \tilde{J}_0^{(1)}) + k_0' f(x,y)(-\tilde{I}^{(0)} + \tilde{J}^{(0)} + \tilde{J}_0^{(0)}) . \tag{4.10}$$

$$\frac{d\tilde{I}^{(2)}}{ds} = k_0'(-\tilde{I}^{(2)} + \tilde{J}^{(2)} + \tilde{J}_0^{(2)}) + k_0' f(x,y)(-\tilde{I}^{(1)} + \tilde{J}^{(1)} + \tilde{J}_0^{(1)}) . \tag{4.11}$$

In the plane-parallel homogeneous case corresponding to Eq.(4.9), the radiative field does not involve the complex function H. Therefore, $\tilde{I}^{(0)}$ is still a real quantity, and the solution is the same as that in previous chapter.

Now consider the equation for the first order perturbation correction of Eq.(4.10), which is an inhomogeneous equation with constant coefficients. We apply the Eddington approximation to this first order correction for the intensity, which now is a

three-dimensional quantity,

$$\tilde{I}^{(1)}(s,\theta,\varphi) = \tilde{I}_0^{(1)}(s) + \tilde{I}_x^{(1)}(s)\nu\cos\varphi + \tilde{I}_y^{(1)}(s)\nu\sin\varphi + \tilde{I}_z^{(1)}(s)\mu\ . \tag{4.12}$$

Integrating Eq.(4.10) in turn over 4π steradians with respect to $d\mu d\varphi$, $\nu\cos\varphi d\mu d\varphi$, $\nu\sin\varphi d\mu d\varphi$, $\mu d\mu d\varphi$ yields respectively,

$$\frac{\partial\tilde{I}_x^{(1)}}{\partial x} + \frac{\partial\tilde{I}_y^{(1)}}{\partial y} + \frac{\partial\tilde{I}_z^{(1)}}{\partial z} = -3k_0'(1-\omega')\tilde{I}_0^{(1)} - \frac{3}{4}k_0'\omega' H F_0 e^{-k_0' z/\mu_0} +$$

$$3k_0' f(x,y)[-(1-\omega')\tilde{I}_0^{(0)} + \frac{\omega'}{4}F_0 e^{-k_0' z/\mu_0}]\ , \tag{4.13}$$

$$\frac{\partial\tilde{I}_0^{(1)}}{\partial x} = -k_0'(1-\omega' g')\tilde{I}_x^{(1)} - \frac{3}{4}k_0'\omega' g'\nu_0\cos\varphi_0 H F_0 e^{-k_0' z/\mu_0}\ , \tag{4.14}$$

$$\frac{\partial\tilde{I}_0^{(1)}}{\partial y} = -k_0'(1-\omega' g')\tilde{I}_y^{(1)} - \frac{3}{4}k_0'\omega' g'\nu_0\sin\varphi_0 H F_0 e^{-k_0' z/\mu_0}\ , \tag{4.15}$$

$$\frac{\partial\tilde{I}_0^{(1)}}{\partial z} = -k_0'(1-\omega' g')\tilde{I}_z^{(1)} - \frac{3}{4}k_0'\omega' g'\mu_0 H F_0 e^{-k_0' z/\mu_0} +$$

$$k_0' f(x,y)[-(1-\omega' g')\tilde{I}_z^{(0)} + \frac{3}{4}\omega' g'\mu_0 F_0 e^{-k_0' z/\mu_0}]\ . \tag{4.16}$$

Differentiating Eq.(4.14) with respect to x, Eq.(4.15) with respect to y and Eq.(4.16) with respect to z, and using Eqs.(4.13) we obtain

$$\nabla^2\tilde{I}_0^{(1)} - \lambda^2\tilde{I}_0^{(1)} = 2f(x,y)[\lambda^2\tilde{I}_0^{(0)} - he^{-k_0' z/\mu_0}] + hHe^{-k_0' z/\mu_0}\ , \tag{4.17}$$

where $h = \frac{3}{4}(1+g'-\omega' g')\omega' k_0'^2 F_0$

Let $\tilde{I}_0^{(1)} = \sum_{mn} e^{\imath\pi(\frac{m}{a}x+\frac{n}{b}y)}Z_{mn}^{(1)}$. By orthogonality relation of Fourier expansions (Zauberer, 1983)

$$\frac{\partial^2}{\partial z^2}Z_{mn}^{(1)} - \lambda_{mn}^2 Z_{mn}^{(1)} = L_{mn}[2\lambda^2\tilde{I}_0^{(0)} - 2he^{-k_0' z/\mu_0} - i\frac{k_0' h}{\mu_0\xi_{mn}}(1-e^{-\imath\xi_{mn}z})e^{-k_0' z/\mu_0}]\ , \tag{4.18}$$

where $\lambda_{mn}^2 = \lambda^2 + (\pi m/a)^2 + (\pi n/b)^2$. The solution of Eq.(4.18) is

$$Z_{mn}^{(1)} = C_{mn}^{(1)}e^{-\lambda_{mn}z} + D_{mn}^{(1)}e^{\lambda_{mn}z} - L_{mn}[\Gamma_{mn}(C^0e^{-\lambda z} + D^0e^{\lambda z}) +$$

$$(\alpha_{mn} + i\beta_{mn})e^{-k_0'z/\mu_0} - (A_{mn} + iB_{mn})e^{-i\xi_{mn}z}e^{k_0'z/\mu_0}] \,, \tag{4.19}$$

where $\Gamma_{mn} = 2\lambda^2/(\lambda_{mn}^2 - \lambda^2)$,
$\alpha_{mn} = 2(\lambda^2\alpha + h)/[(k_0'/\mu_0)^2 - \lambda_{mn}^2]$, $\beta_{mn} = [k_0'h/(\mu_0\xi_{mn})]/[k_0'/\mu_0)^2 - \lambda_{mn}^2]$,
$A_{mn} = 2h(k_0'/\mu_0)^2/[R_{mn}^2 + (2k_0'\xi_{mn}/\mu_0)^2]$, $B_{mn} = R_{mn}k_0'h/(\mu_0\xi_{mn})/[R_{mn}^2 + (2k_0'\xi_{mn}/\mu_0)^2]$
with $R_{mn} = (k_0'/\mu_0)^2 - \xi_{mn}^2 - \lambda_{mn}^2$.

$C_{mn}^{(1)}$ and $D_{mn}^{(1)}$ are complex constants determined by boundary conditions. The $\tilde{I}_x^{(1)}$, $\tilde{I}_y^{(1)}$ and $\tilde{I}_z^{(1)}$ can be derived from Eqs.(4.14), (4.15) and (4.16). Just as for the discussion in the last chapter, we have,

$$\tilde{I}_0^{(1)}(x,y,0) + \frac{2}{3}\tilde{I}_z^{(1)}(x,y,0) = 0 \,, \tag{4.20}$$

$$\tilde{I}_0^{(1)}(x,y,z_0) - \frac{2}{3}\tilde{I}_z^{(1)}(x,y,z_0) = 0 \,, \tag{4.21}$$

the orthogonality relations between different modes project out the $C_{mn}^{(1)}$ and $D_{mn}^{(1)}$ for each mode.

For the single mode case, the solution of Eq.(4.10) yields the same result as that of chapter 3. However the calculation process becomes much simpler in the scheme of a mode expansion in the complex space.

For the second order correction, considering Eq.(4.11) by a process similar to the first order solution, we obtain

$$\frac{\partial\tilde{I}_x^{(2)}}{\partial x} + \frac{\partial\tilde{I}_y^{(2)}}{\partial y} + \frac{\partial\tilde{I}_z^{(2)}}{\partial z} = -3k_0'(1-\omega')\tilde{I}_0^{(2)} + \frac{3}{8}k_0'\omega' HHF_0e^{-k_0'z/\mu_0}$$
$$+ 3k_0'f(x,y)[-(1-\omega')\tilde{I}_0^{(1)} - \frac{\omega'}{4}HF_0e^{-k_0'z/\mu_0}] \,, \tag{4.22}$$

$$\frac{\partial\tilde{I}_0^{(2)}}{\partial x} = -k_0'(1-\omega'g')\tilde{I}_x^{(2)} + \frac{3}{8}k_0'\omega'g'\nu_0\cos\varphi_0 HHF_0e^{-k_0'z/\mu_0}$$
$$+ k_0'f(x,y)[-(1-\omega')\tilde{I}_0^{(1)} - \frac{3}{4}\omega'g\nu_0\cos\varphi_0 HF_0e^{-k_0'z/\mu_0}] \tag{4.23}$$

$$\frac{\partial\tilde{I}_0^{(2)}}{\partial y} = -k_0'(1-\omega'g')\tilde{I}_x^{(2)} + \frac{3}{8}k_0'\omega'g'\nu_0\sin\varphi_0 HHF_0e^{-k_0'z/\mu_0}$$

$$+ k_0' f(x,y)[-(1-\omega')\tilde{I}_0^{(1)} - \frac{3}{4}\omega' g \nu_0 \sin\varphi_0 H F_0 e^{-k_0' z/\mu_0}] \tag{4.24}$$

$$\frac{\partial \tilde{I}_0^{(2)}}{\partial z} = -k_0'(1-\omega' g')\tilde{I}_z^{(2)} + \frac{3}{8}k_0'\omega' g' \mu_0 H H^{\Gamma_\backslash} e^{-k_0' z/\mu_0}$$

$$+ k_0' f(x,y)[-(1-\omega' g')\tilde{I}_z^{(1)} - \frac{3}{4}\omega' g' \mu_0 H F_0 e^{-k_0' z/\mu_0}] \,. \tag{4.25}$$

Also, by a process similar to the first order case, we have

$$\nabla^2 \tilde{I}_0^{(2)} - \lambda^2 \tilde{I}_0^{(2)} = 2\lambda^2 f \tilde{I}_0^{(1)} + \frac{\partial f}{\partial x}\frac{\partial \tilde{I}_0^{(1)}}{\partial x} + \frac{\partial f}{\partial y}\frac{\partial \tilde{I}_0^{(1)}}{\partial y} + \lambda^2 f^2 \tilde{I}_0^{(0)} - h(f^2 - 2fH + \frac{1}{2}HH)e^{-k_0' z/\mu_0} \,. \tag{4.26}$$

Let $\tilde{I}_0^{(2)} = \sum_{mn} e^{\imath\pi(\frac{m}{a}x + \frac{n}{b}y)} Z_{mn}^{(2)}$. The orthogonality relation between modes gives

$$\frac{\partial^2}{\partial z^2} Z_{mn}^{(2)} - \lambda_{mn}^2 Z_{mn}^{(2)} = \sum_{\substack{i+k=m \\ j+l=n}} L_{ij} L_{kl} [\Phi_{ijkl} Z_{kl}^{(1)} + \lambda^2 \tilde{I}_0^{(0)} - h e^{-k_0' z/\mu_0}$$

$$- i\frac{2k_0' h}{\mu_0 \xi_{kl}}(1 - e^{-\imath\xi_{kl} z})e^{-k_0' z/\mu_0} + \frac{k_0'^2 h}{2\mu_0^2 \xi_{ij}\xi_{kl}}(1 - e^{-\imath\xi_{ij} z})(1 - e^{-\imath\xi_{kl} z})e^{-k_0' z/\mu_0}] \,, \tag{4.27}$$

where $\Phi_{ijkl} = 2\lambda^2 - (\pi/a)^2 ik - (\pi/b)^2 jl$. The solution of Eq.(4.27) is

$$Z_{mn}^{(2)} = C_{mn}^{(2)} e^{-\lambda_{mn} z} + D_{mn}^{(2)} e^{\lambda_{mn} z} + \sum_{\substack{i+k=m \\ j+l=n}} L_{ij} L_{kl} [-(\alpha_{ijkl} + i\beta_{ijkl}) e^{-k_0' z/\mu_0}$$

$$-(A_{ijkl} + iB_{ijkl}) e^{-\imath\xi_{kl} z} e^{k_0' z/\mu_0} + (S_{ijkl} + iT_{ijkl}) e^{-\imath(\xi_{ij}+\xi_{kl})z} e^{k_0' z/\mu_0}$$

$$- \begin{cases} \Omega_{ijkl}^{*}(-C_{kl}^{(1)} z e^{-\lambda_{kl} z} + D_{kl}^{(1)} z e^{\lambda_{kl} z}) & , |i+k| = |k|, |j+l| = |l| \\ \Omega_{ijkl}(C_{kl}^{(1)} e^{-\lambda_{kl} z} + D_{kl}^{(1)} e^{\lambda_{kl} z}) & , \text{others} \end{cases}$$

$$- \left[\begin{cases} \Gamma_{ijkl}^{*}(-C^{(0)} z e^{-\lambda z} + D^{(0)} z e^{\lambda z}) & , i+k=0, j+l=0 \\ \Gamma_{ijkl}(C^{(0)} e^{-\lambda z} + D^{(0)} e^{\lambda z}) & , \text{others} \end{cases} \right] . \tag{4.28}$$

The coefficients in Eq.(4.28) are given in Appendix B. $\tilde{I}_x^{(2)}$, $\tilde{I}_y^{(2)}$ and $\tilde{I}_z^{(2)}$ can derived from Eqs.(4.23), (4.24) and (4.25). The complex constants $C_{mn}^{(2)}$ and $D_{mn}^{(2)}$ are determined in a way similar to that for the first order perturbation solution.

4.2 Numerical results and discussions

The second order perturbation solution to the radiative transfer equation in a medium with internal inhomogeneity has been derived in the last section. Calculations show that $I^{(0)}, I^{(1)}$ and $I^{(2)}$ are of the same order. The perturbation series is expected to be convergent with the increase of powers of ϵ. Therefore the configuration of the distribution of the upwelling intensity is dominated by the first order perturbation result for small perturbation coefficient. To show the second order correction, we consider a cloud field with an internal single mode variation of extinction coefficient of Eq.(3.1) as discussed in chapter 3. Take the extinction coefficient to be $k_0 = 50\,km^{-1}$, cloud droplet asymmetry factor $g = 0.86$, single scattering albedo $\omega = 0.999$, perturbation coefficient $\epsilon = 0.2$, cloud depth $z_0 = 500\,m$, and cloud horizontal periodic length $L = 2a = 2b$. Two values of L are considered in Fig.4.1.

Figures.4.1a and 4.1b show the distributions of the upwelling intensities when only the first order perturbation correction is included; Fig.4.1c and 4.1d are the corresponding distributions of upwelling intensities with the both first and second order corrections are included. In Fig.4.1a and 4.1c the solar zenith angle $\theta_0 = 0^0$, and in Fig.4.1b and 4.1d $\theta_0 = 60^0$, $\varphi_0 = 0^0$. The configurations of the distribution of the upwelling intensity in Fig.4.1a and 4.1c are consistent with the configuration of the distribution of the extinction coefficient of Eq.(3.1). These configurations are called correlated distributions in chapter 3. The configurations in Fig.4.1b and 4.1d are opposite to that of the extinction coefficient; they are called anti-correlated distributions. Also, there exists the shift phenomenon in Fig.4.1b and 4.1d, since the solar zenith angle is inclined towards the x direction. We find that there are only slight differences between the configurations when the second order correction is included. However, the difference is still noticeable. In Fig.4.1c the central region is lower and smoother in comparison with Fig.4.1a. The central raised region is higher in Fig.4.1d in comparison with Fig.4.1b.

In chapter 3 it was shown that there is no difference in cloud albedo (the horizontally averaged reflectance) due to the single mode cosinusoidal variation of extinction

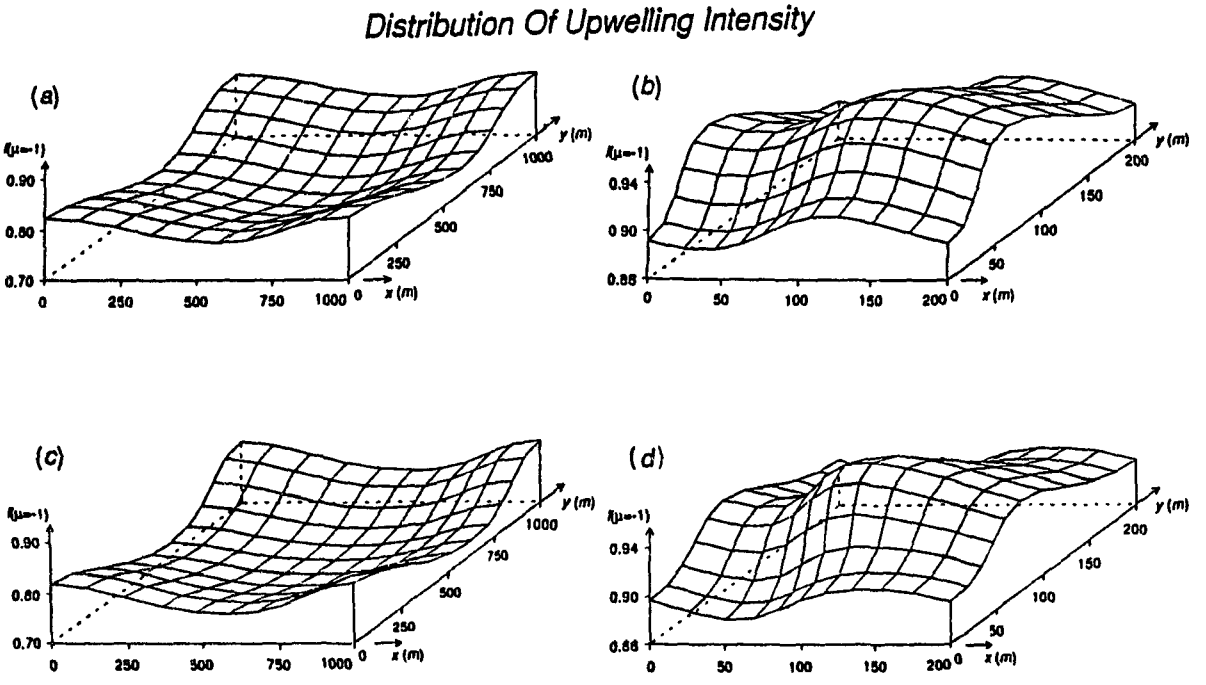

Figure 4.1: Two dimensional distributions of the upwelling intensities. In (a) and (b), the perturbation correction is up to the first order. In (c) and (d), the perturbation correction is up to the second order. Cloud depth 500m. Solar zenith angle $\theta_0 = 0^0$ in (a) and (b), and $\theta_0 = 60^0, \varphi_0 = 0^0$ in (b) and (d). The intensities are normalized with respect to $\mu_0 F_0$.

coefficient, since there is no zero mode correction existing in this case. However, even for the single mode case, the change of cloud albedo does not vanish if the second order perturbation is applied, because the horizontal eigenmode expansions are generally different for $I^{(1)}$ and $I^{(2)}$. Since the first order perturbation shows no contribution to the change of cloud albedo, the change of cloud albedo is proportional to ϵ^2, so a small change of cloud albedo is expected.

Fig.4.2 displays the relative change of cloud albedo ($\Delta\alpha/\alpha$) corresponding to the cloud geometrical factors, where α is the unperturbed value of cloud albedo for the plane-parallel case and $\Delta\alpha$ is the change of cloud albedo due to the internal inhomogeneity of the cloud. The single scattering parameters (k_0, ω, g) as well as ϵ are the same as those in Fig.4.1, and the solar zenith angle is zero. Fig.4.2 shows that the internal inhomogeneity of cloud always decreases the cloud albedo. This seems consistent with the common belief that the cloud internal inhomogeneity causes a reduction in cloud albedo (Stephens and Tsay, 1990). In Fig.4.2a the relative change of cloud albedo corresponding to the cloud depth is shown with two different horizontal periodic lengths considered. When the cloud is very shallow, the change of cloud albedo is very small for both lengths of L. As the the cloud depth increases, the value of the relative change of cloud albedo increases. However the relative change of cloud albedo reaches a maximum value at a certain value of cloud depth, and then becomes smaller with the further increase of cloud depth. In Fig.4.2a, for any given value of cloud depth, the relative change of cloud albedo is always larger for the smaller horizontal periodic length ($L = 200\,m$). The smaller L value represents larger internal inhomogeneity. Therefore the more inhomogeneous the cloud the larger the cloud albedo change. However this conclusion is not always true for small horizontal periodic length. In Fig.4.2b, when L is less than $100\,m$, the value of cloud albedo change shows no increase as the periodic length decreases, especially for the curve of $z_0 = 1000\,m$. For a small value of L close to the photon free path length, it is easy for the diffuse photon to pass through relatively large regions with different extinction coefficients. From this point of view, the cloud would not become more

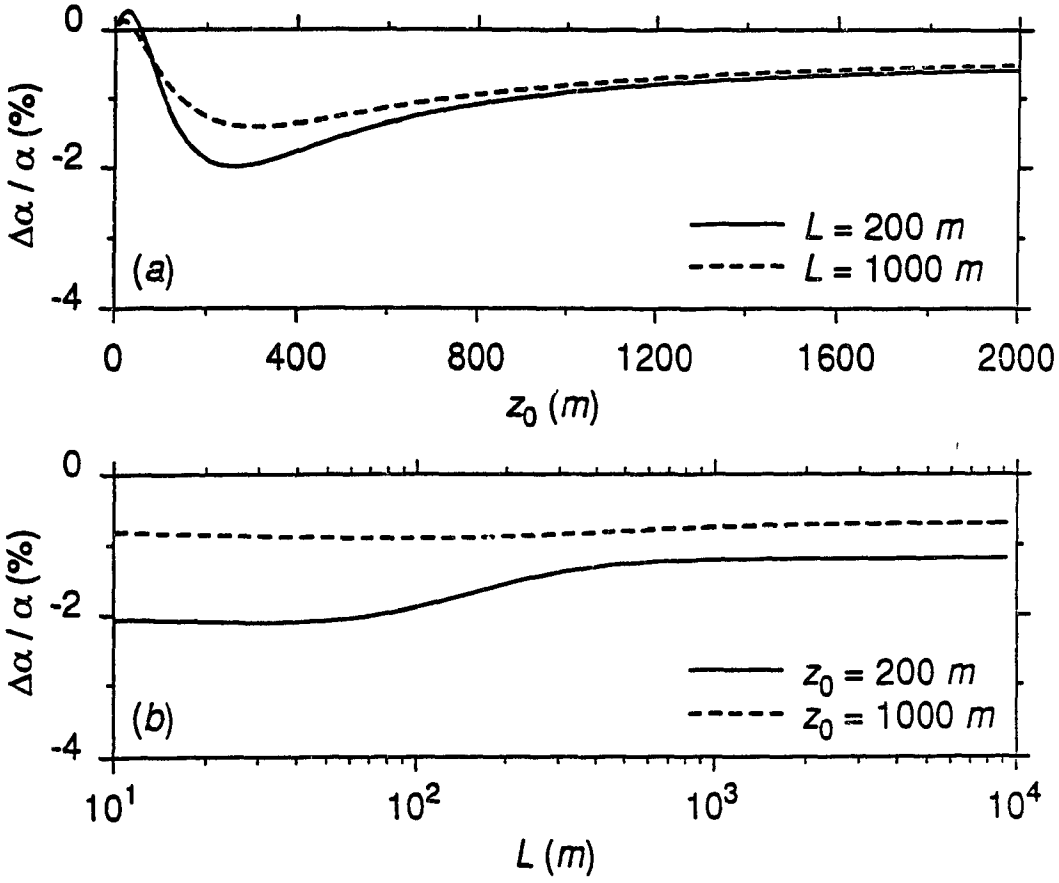

Figure 4.2: The relative change of cloud albedo as a function of: (a) cloud depth z_0, (b) cloud horizontal periodic length L. Solar zenith angle $\theta_0 = 0^0$.

inhomogeneous as L decreases further, and the change of cloud albedo would not increase.

The sensitivity of the cloud albedo to the cloud scattering parameters is shown in Fig.4.3. The cloud depth is $z_0 = 500\,m$, the horizontal periodic length is $L = 500\,m$ and the solar zenith angle is $\theta_0 = 0^0$. In most cases the relative change of cloud albedo is negative corresponding to the variation of cloud single scattering factors. However, in Fig.4.3a and 4.3c there are cases where the relative change of cloud albedo is positive. Therefore, the conclusion that the cloud internal inhomogeneity always brings about a decrease of cloud albedo is not a fully general correct statement. One case of positive change of cloud albedo happens when the extinction coefficient is very small. In this situation the probability of scattering or absorption of photons is very small, and the directed solar beam can easily pass through the cloud. Another case of the increase of cloud albedo happens when the asymmetry factor is close to one. In this situation the forward scattering dominates, and again it is easy for the directed solar beam to pass through the cloud. Therefore, the positive change of cloud albedo due to cloud internal inhomogeneity is likely to happen in the case when the cloud albedo is very small.

The multi-mode solution allows the calculation of the radiative transfer in a medium with an arbitrary type of horizontal periodic variation of the extinction coefficient, provided that the second order perturbation expansion is valid. Consider the two examples of the distribution of extinction coefficient shown in Fig.4.4. The variation in the distribution is only in one dimension which means the cloud field is homogeneous in the y direction.

Consider the cloud field with internal periodic variation of extinction coefficient shown in Fig.4.4a. Set the solar zenith angle $\theta_0 = 0^0$, the scattering parameters the same as those in Fig.4.1, and the cloud depth $z_0 = 500\,m$. $\epsilon = 0.2$. The calculations includes second order perturbation terms.

Since only the lowest mode of the local angular part of the radiance is considered in the Eddington approximation, the discussion of the resultant flux (angular integrated

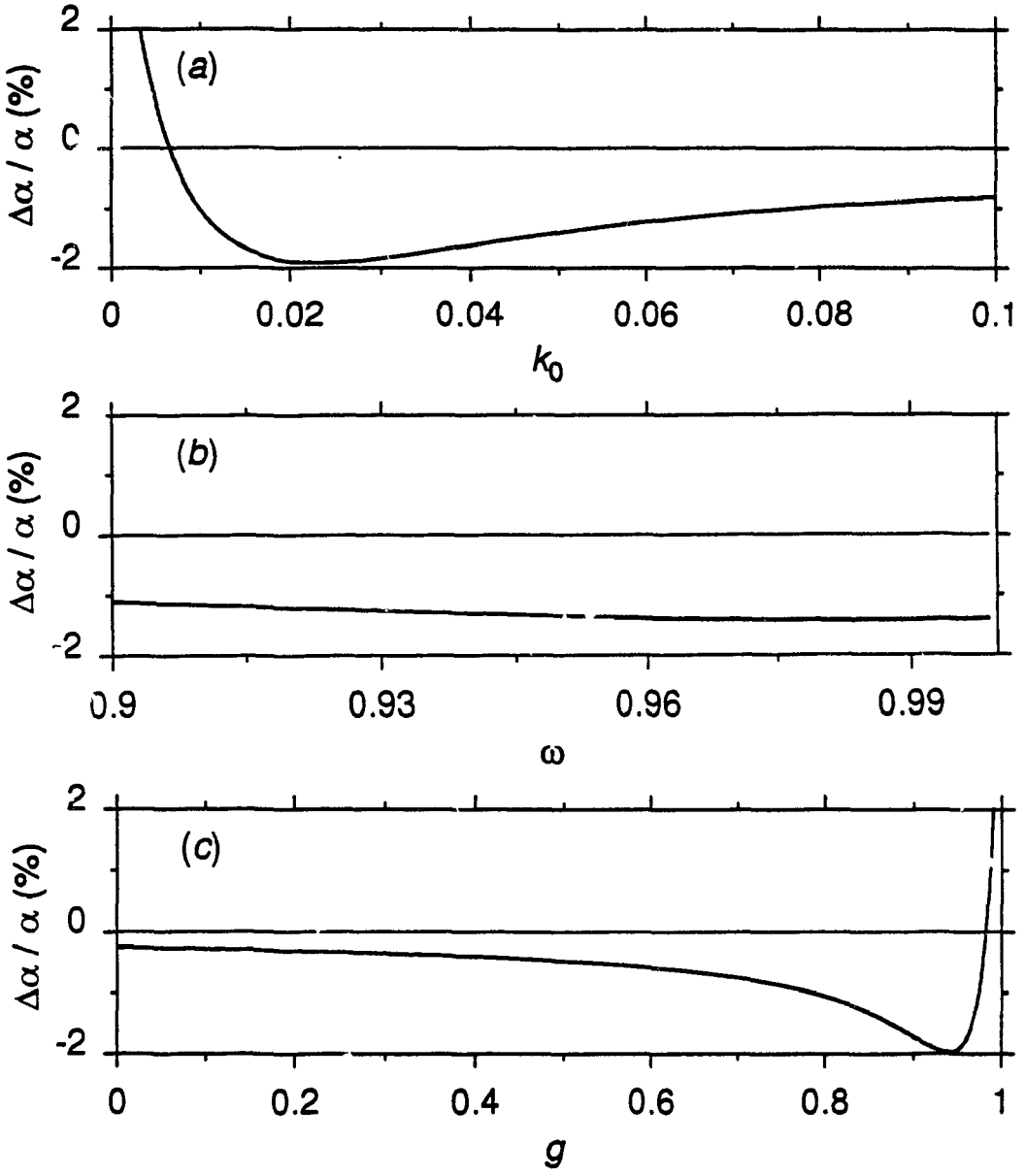

Figure 4.3: The relative change of cloud albedo as a function of: (a) extinction coefficient k_0 ($g = 0.86, \omega = 0.999$), (b) asymmetry factor g ($k_0 = 50\,km^{-1}, \omega = 0.999$), (c) single scattering albedo ω ($k_0 = 50\,km^{-1}, g = 0.86$). Solar zenith angle $\theta_0 = 0^0$.

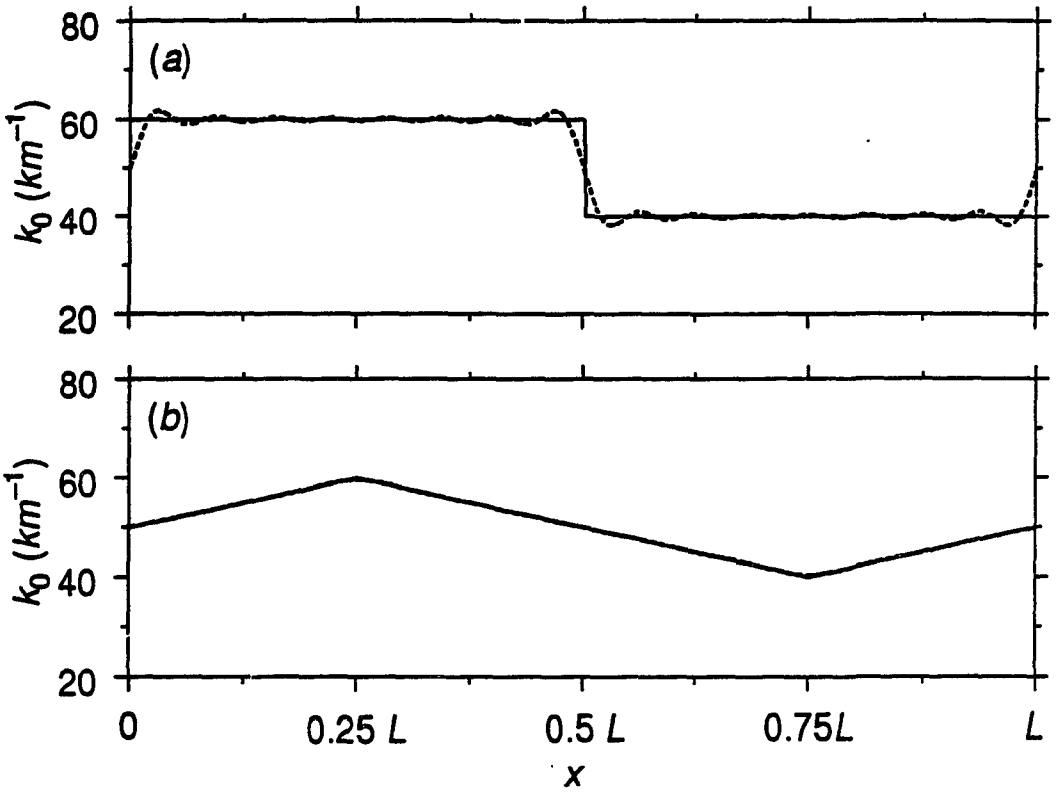

Figure 4.4: One dimensional distributions of extinction coefficient in one periodic region (solid line), and the 16 mode Fourier series fits (dashed line). In the y direction the distribution is homogeneous.

quantity) is more reliable than that of the radiance. Therefore we will consider the distribution of the upward flux instead of the upwelling intensity in the multi-mode case. In Fig.4.5 the upward fluxes corresponding to different periodic lengths are shown. Comparison of Fig.4.5a with Fig.4.4a indicates that the configuration of the distribution of the upward flux is nearly opposite to the configuration of the distribution of the extinction coefficient. The regions with larger extinction coefficient are the regions with the smaller reflected flux. This is called the anti-correlated distribution and is mostly due to the horizontal leaking of diffuse photons from the regions of a larger extinction coefficient to the regions of a smaller extinction coefficient. The more detailed physical explanation was presented in chapter 3.

Similar to the results in chapter 3, the upward flux tends to change from an anti-correlated distribution to a correlated distribution as the periodic length becomes larger. In Fig.4.5b the distribution of upward flux becomes larger on the left side and smaller on the right hand side. In Fig.4.5b we find that the shape of the distribution of the upward flux is distorted from the shape of distribution of the extinction coefficient. This is a new characteristic for the multi-mode case. For a further increase in the periodic length to $L = 2000\,m$, the upward flux is shown in Fig.4.5c. The amplitude of fluctuation is increased and the shape of the distribution is more closely correlated to the distribution of the extinction coefficient. In Fig.4.5b and 4.5c there are small fluctuations in the distributions of upward fluxes, which is mostly due to the termination of the Fourier series expansion (see Fig.4.4a).

Comparing Fig.4.5b and 4.5c with Fig.4.4a, the most distorted regions in distribution are observed at places with sudden change of extinction coefficient, such as the point of $x = \frac{L}{2}$. At $\frac{L}{2}$ there is not a sharp decrease in the distribution of upward flux as there is in the distribution of extinction coefficient, and a peak appears near $\frac{L}{2}$. As we discussed in chapter 3, the upward diffuse photons have a tendency of transporting from the regions of a larger extinction coefficient to the regions of a smaller extinction coefficient. These horizontal leakage of photons mostly occur at the transition regions of different extinction coefficients. Therefore the configuration of the distribution of

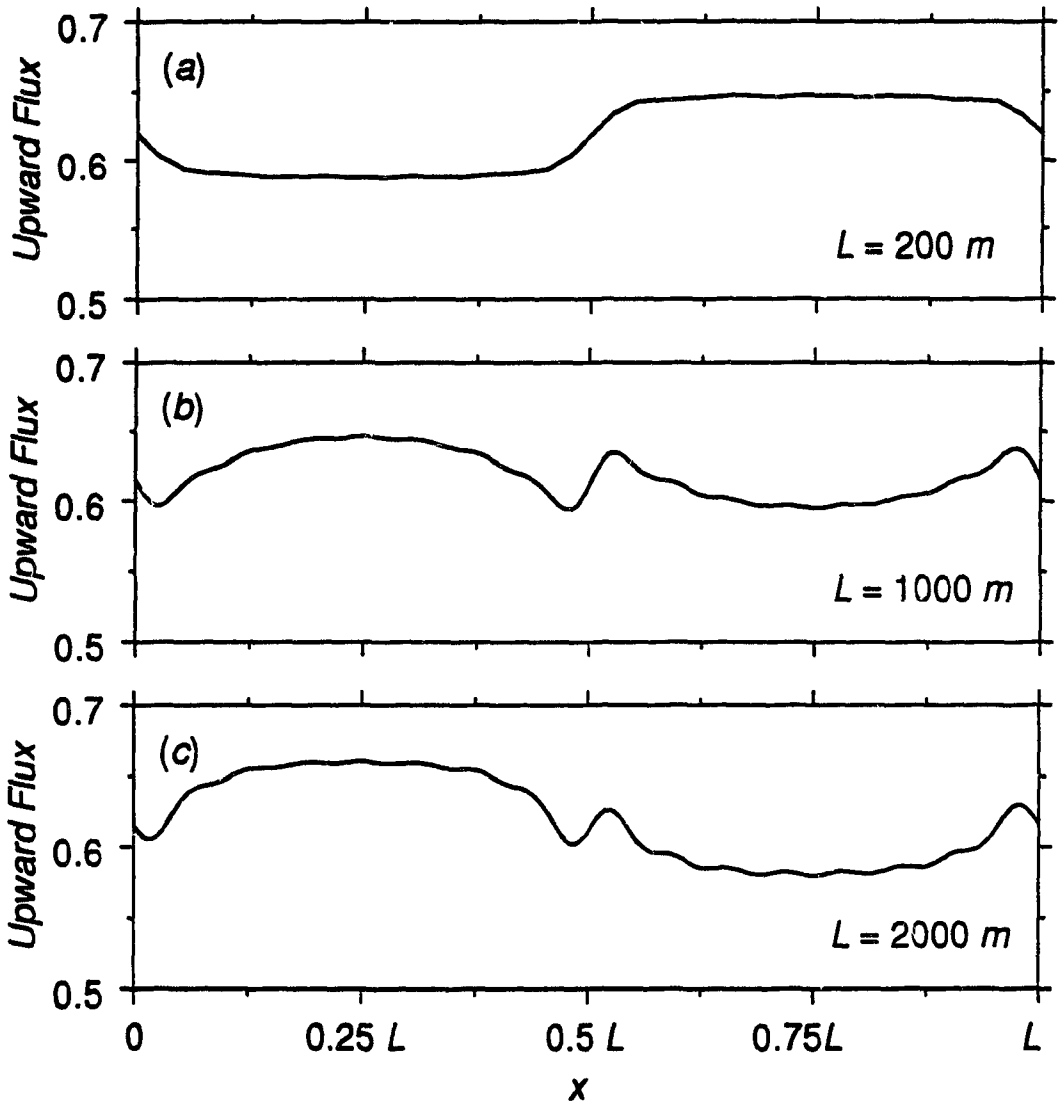

Figure 4.5: One dimensional distributions of upward fluxes corresponding to the distribution of extinction coefficient in Fig.4.4(a). Solar zenith angle $\theta_0 = 0^0$. The fluxes are normalized with respect to $\mu_0 \pi F_0$.

the upward flux shows a very different shape as compared to that of the extinction coefficient near the transition regions. The leaking photons have a smaller influence on the regions far from the boundary. In Fig.4.5b and 4.5c, the distribution of the upward flux is relatively smooth near $x = \frac{L}{4}$ and $\frac{3L}{4}$. Also, from this point of view it is easy to explain why the anti-correlated distribution happens in the case of small periodic length (Fig.4.5a).

Turning to the solar zenith angle $\theta_0 = 60^0$, setting the azimuth angle $\varphi_0 = 0^0$, and keeping the other parameters at the same values as those in Fig.4.5, the resultant upward fluxes are shown in Fig.4.6. In comparison with Fig.4.5, the configurations of the distributions of the upward flux are severely distorted. In the case of the single mode (see chapter 3), when the zenith angle is large, the raised regions (for anti-correlated distribution) shift in the direct solar beam direction or the lowered region (for correlated distribution) shift opposite to the direct solar beam direction. This is called the shift phenomenon. However, in the multi-mode case of Fig.4.6, one hardly finds the shift phenomenon any more. Fig.4.6 shows that the distribution of the upward flux strongly deviates from the distribution of the cloud internal optical property variations. The radiative transfer is a complicated process, which depends on many factors. One of the key points in the determination of the distribution of the reflectance is the horizontal leaking of diffuse photons between regions with different extinction coefficients. In dealing with radiative transfer in inhomogeneous clouds, the independent pixel approximation (IPA) is often used (Evans, 1993), in which the space is divided into each independent regions or pixels in radiative transfer processes. From the above discussion the reliability of IPA is not expected to be high, especially in the case of large solar zenith angles.

Let us briefly discuss the distributions of the upward flux in Fig.4.7, which correspond to the cloud field of Fig.4.4b. The solar zenith angle, scattering parameters and the cloud thickness are all the same as those in Fig.4.5. Also, the anti-correlated distribution of upward flux appears in the case of relatively smaller periodic length (see Fig.4.7a). In Fig.4.7b and 4.7c, for a larger periodic length, the configuration of

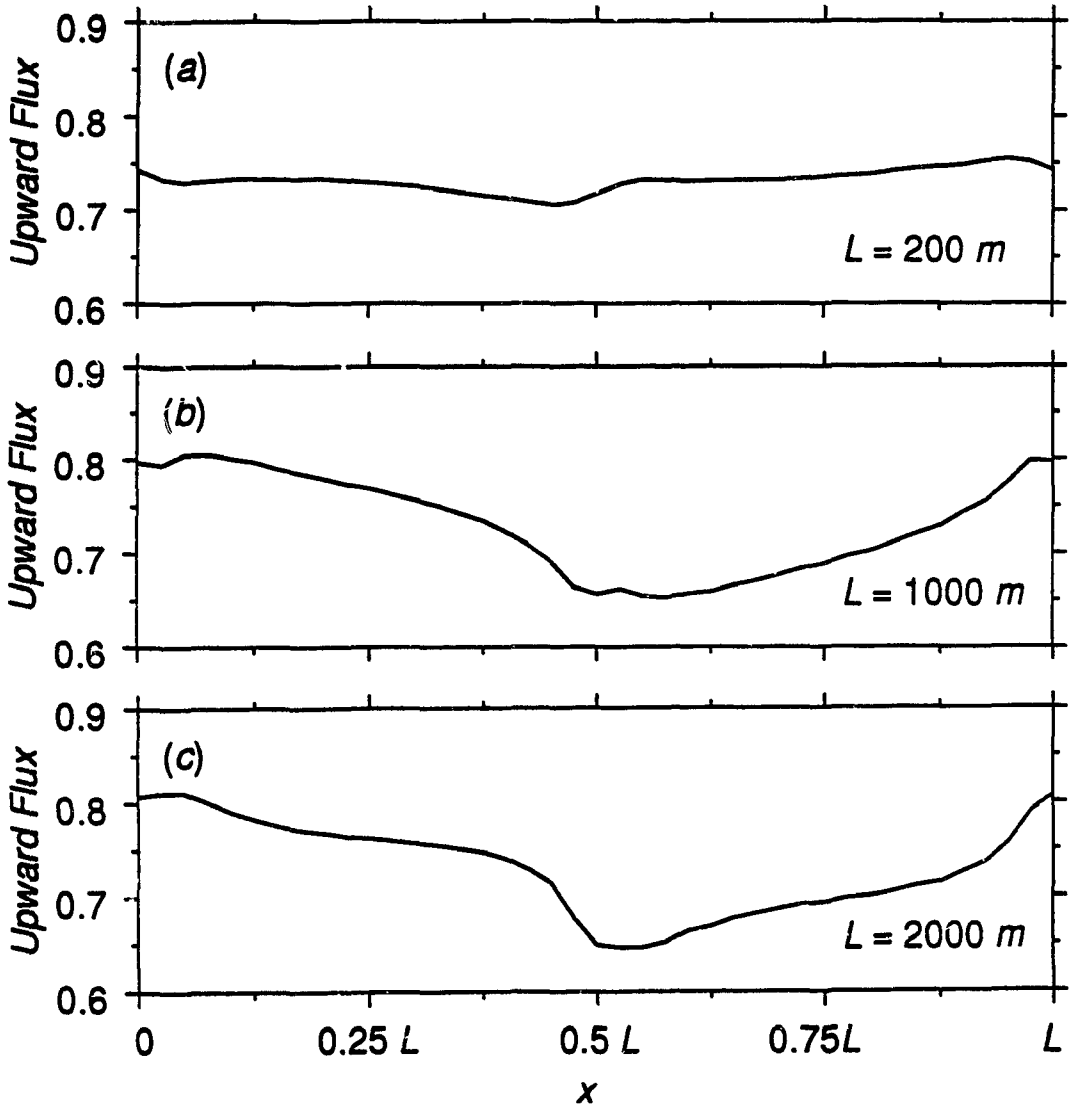

Figure 4.6: Same as that in Fig.4.5, with $\theta_0 = 60^0, \varphi_0 = 0^0$.

distribution of the upward flux becomes very close to the corresponding configuration of the distribution of the extinction coefficient. However in Fig.4.7b and 4.7c the peak at $\frac{L}{4}$ has been partly lowered, and the valley at $\frac{3L}{4}$ has been partly filled, especially in Fig.4.7b, which also can be explained by the net horizontal leaking of photons from the regions of larger extinction coefficient to the regions of smaller extinction coefficient.

4.3 Summary

For radiative transfer in a medium with internal variation of optical properties, the perturbation method is probably the only way to obtain an approximate analytical solution. In comparison with chapter 3, the expansion of the perturbation function in the complex exponentials makes the solution simpler, and easier to apply to the higher order multi-mode case. The numerical convergence properties of the perturbation series indicates that the perturbation solution is reliable.

Albedo changes only appear in the second order perturbation correction. Hence the cloud internal inhomogeneity has a much larger influence on the distribution of the reflected photons than on the cloud albedo. Contrary to the common but unproven belief that the cloud internal inhomogeneity always decreases the cloud albedo, it was found that in some cases the cloud internal inhomogeneity can increase the cloud albedo as well.

The multi-mode case calculations showed that the reflected upward flux generally corresponds poorly to the distribution of the internal variation of extinction coefficient, especially under the circumstance when the solar zenith angle is large. This probably may be one of the reasons why it is hard to retrieve the cloud internal optical properties from the cloud reflectance.

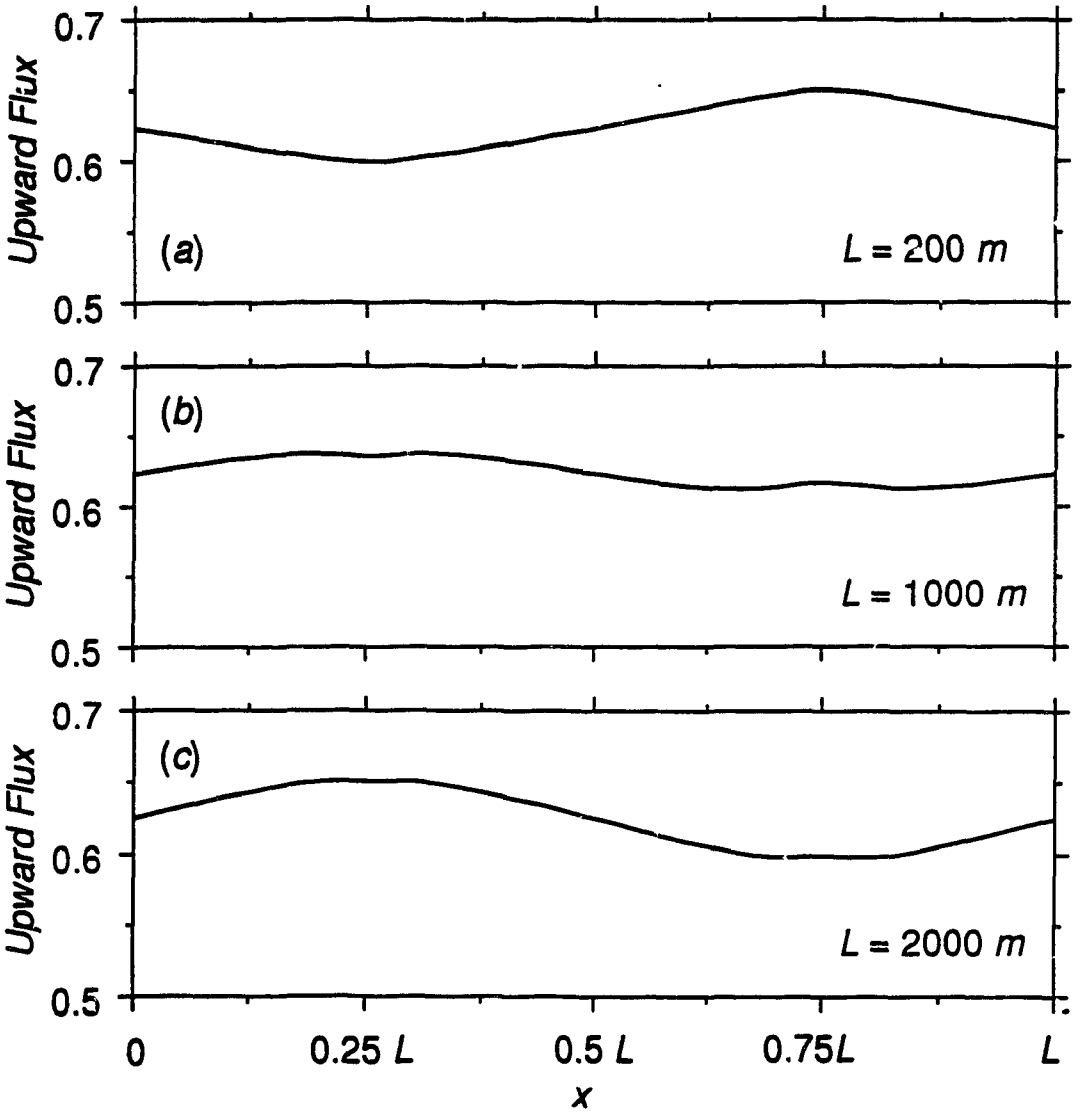

Figure 4.7: One dimensional distributions of upward fluxes corresponding to the distribution of extinction coefficient in Fig.4.4(b). Solar zenith angle $\theta_0 = 0^0$. The fluxes are normalized with respect to $\mu_0 \pi F_0$.

Chapter 5

Distributions of Irradiance, Monte Carlo Simulations

In this chapter the Monte Carlo simulation is used again to investigate the horizontal irradiance distribution in clouds. One goal of this work is to verify numerically of the results of the analytical solution in the last two chapters and to show phenomenon such as anti-correlated distributions through the realistic simulation of radiative transfer processes. This would support the physical findings in the last two chapters. Another goal is to investigate the impact of geometric variations on the distribution of irradiance, which is very hard to obtain through analytical methods. The cloud absorption anomaly will be discussed again in this chapter.

5.1 The limitations of Monte Carlo simulations

As we pointed out in chapter 2, the irradiance can be computed fairly easily for any cloud shape with internal inhomogeneity through Monte Carlo simulations. However, the calculated irradiance is for the total bulk of reflected photons for the whole cloud field considered. The Monte Carlo method can hardly be used to obtain the space distribution of reflected radiance (irradiance) at the top of the cloud. The problem is that the number of photons used in practical Monte Carlo simulations is very small in

comparison with the corresponding number of photons in the incoming solar beam. At the top of the atmosphere the flux of photons in the solar beam is about $10^{30}\, m^{-2} sec^{-1}$. However, in Monte Carlo simulation, only about 10^5 to 10^8 photons are spread out over an area of about 10^4 to $10^8\, m^2$. The very small number of photons per unit area causes large fluctuations in the calculation of the distribution of the reflected photons. For the radiance the situation is even worse, since the number of photons entering in a unit solid angle would be too small for statistically significant results. Therefore, the use of Monte Carlo simulations is limited and analytical solutions are necessary in some circumstances.

The cloud surface can be subdivided into regions which are of scale of the inhomogeneity. If the cloud internal variation in a certain region is small enough, this region can be taken to be homogeneous and the distribution of reflection in this region can be assumed to be the homogeneous as well. Then the reflected flux of this region can be obtained from the total number of photon reflected from this region. Therefore, the distribution of the reflected photons for the whole cloud can be obtained through interpolation of the reflectance values for the finite number of subdivided regions. If the number of the subdivided regions is not too large, the reflected photons in each region can still be large enough to keep a small standard deviation.

In this method the cloud field is divided into a limited number of homogeneous regions. The internal variation of the cloud is not continuous, and the distribution of the upward reflectance is assumed to be homogeneous for each subdivided region. However, this scheme differs from independent pixel approximation (IPA), since photons inside the cloud are allowed to be transported through different regions. As we pointed out, the interaction between the regions with different internal variation is important to determine the distribution of the cloud reflectance.

5.2 Horizontal distribution of irradiance

Monte Carlo simulations are used to explore the distributions of cloud upward irradiance. The cloud field has a two dimensional cosinusoidal periodic variation in extinction coefficient as described in Eq.(3.1). The optical parameters are $k_0 = 0.05\,m^{-1}$, $g = 0.86$, and $\omega = 0.999$. The cloud depth is $z_0 = 500\,m$ and the solar zenith angle is $\theta_0 = 0^0$. In the Monte Carlo simulations of Fig.5.1, the cloud field for one period is horizontally divided into ten by ten subregions each with homogeneous internal optical parameters. The outgoing photons gathered from each of subregions represent a point value for the distribution of the upward flux.

The Monte Carlo simulations of the distribution of upward irradiance are presented in Fig.5.1. It can be found that the anti-correlated distribution appears where the periodic length is small ($L = 200\,m$, Fig.5.1a). Also, the distribution turns to be correlated as the periodic length becomes larger (Fig.5.1b). The results in Fig.5.1 agree with our perturbation calculations in previous two chapters.

We can not expect the Monte Carlo results to be exactly same as those from analytical calculations. In the perturbation method the δ-Eddington approximation is used, in which the higher order angular contributions are ignored. In Monte Carlo simulations the Henyey-Greenstein phase function is used, in which the forward scattering peak is suppressed in comparison with the Mie scattering results. Also, as we discussed above the internal variation of the cloud fields is not continuous in Monte Carlo simulations. However, the anti-correlated distribution is still found in Monte Carlo simulations. In Fig.5.1, the fluctuations in the distribution is due to the limited number of photons used.

For the perturbation method described in the previous two chapters, the asymmetry factor g and the single scattering albedo ω are kept constant as the extinction coefficient k varies. Generally g and ω would also change as we discussed in chapter 2. However, for horizontal variation, there is no measurements to show the correlation of g and ω with k. Since the changes in g and ω are usually very small, the perturbation method would also be applicable with a more complicated derivation,

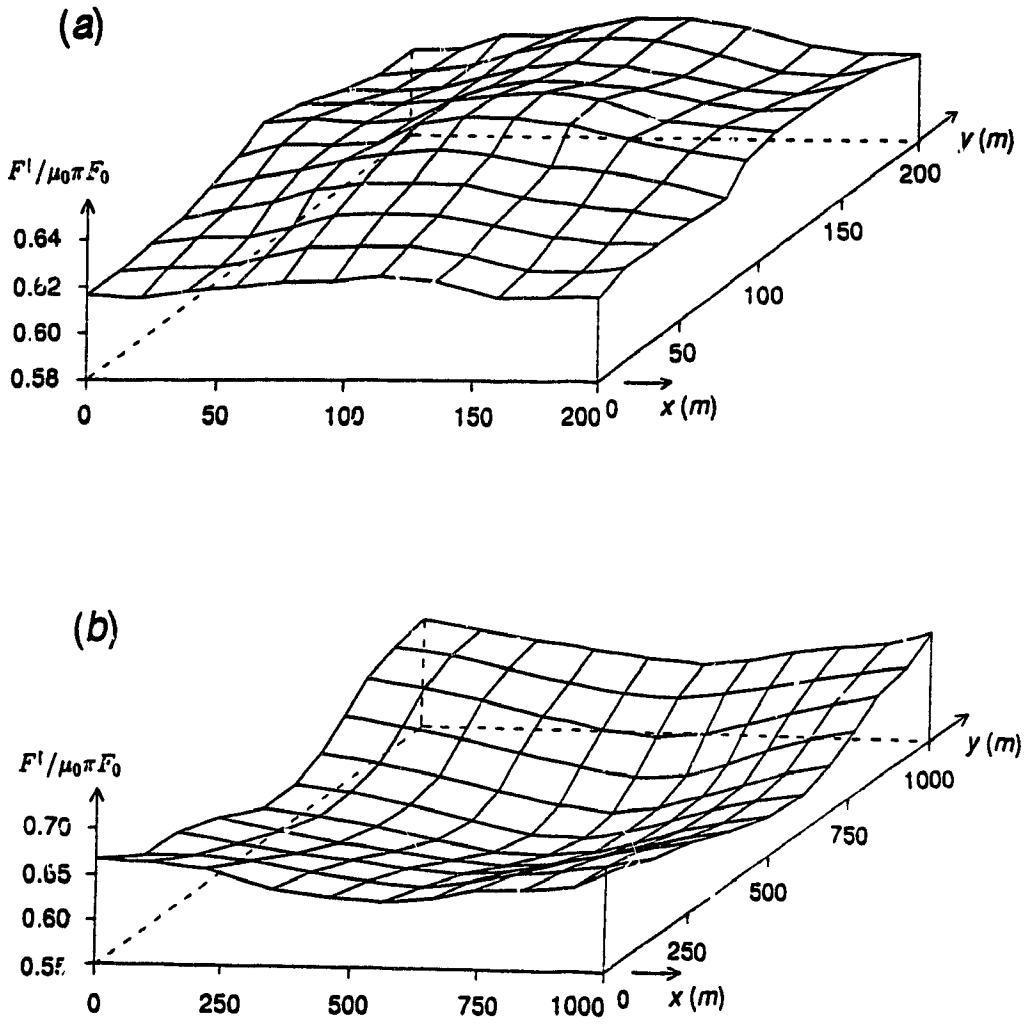

Figure 5.1: Two dimensional distributions of the upward irradiance $F^{\uparrow}$ at different periodic lengths. (a) $L = 200\,m$; (b) $L = 1000\,m$. Solar zenith angle $\theta_0 = 0°$. The optical parameters $k_0 = 0.05\,m^{-1}$, $g = 0.86$, and $\omega = 0.999$. Cloud depth $z_0 = 500\,m$. The irradiances are normalized with respect to $\mu_0\pi F_0$.

if the relationship between the three parameters is known. However, the sensitivity of the distribution of the reflectance to the variation of g and ω can be shown easily using Monte Carlo simulations.

In chapter 2, it was found that even for a large change in k, the corresponding changes of g and ω were very small. This is the reason why a large change in extinction coefficient does not lead to a large change in the reflectance. For overcast cloud the change in reflectance is only about 1%. In chapter 2, the relation between the liquid water content W and effective radius r_e was obtained through observational data. For the internal vertical variation there is a parameterization (Fouquart *et al.*,1990)

$$r_e = 4\mathrm{W} + 11 \,, \tag{5.1}$$

where W is in units of $g\,m^{-3}$ and r_e is in units of μm. If r_e is in proportional to W (in Eq.(5.1)), the density of the droplet number should not change very much in space, which is commonly observed. Though this approximation is obtained through the vertical variation, we hope to use it to explore the sensitivity of the variation of g and ω in the horizontal variations since there is no observation data available.

For easy comparison we take the case of a two-dimensional cloud. The cloud fields have an internal variation of

$$\mathrm{W} = \mathrm{W}_0[1 + \epsilon \cos(ax)] \tag{5.2}$$

where W_0 is the unperturbed liquid water content, and the corresponding effective radius is obtained by the Eq.(5.1). As in chapter 2, the optical properties of the cloud can be found through the Slingo parametrization, also the 4 band scheme is used.

In Fig.5.2, the parameters are as following: liquid water content $\mathrm{W}_0 = 0.2\,g\,m^{-3}$, $\epsilon = 0.2$, solar zenith angle $\theta_0 = 0^0$, and periodic length $L = 200\,m$. One of the two curves in Fig.5.2 shows the distribution of upward irradiance with only the spatial variation of extinction coefficient k, while g and ω are taken as their spatially averaged values. The other curve shows the distribution of upward irradiance when the g and ω change with k according to the relations of Eqs.(5.1), (5.2), (2.19), (2.20) and (2.21).

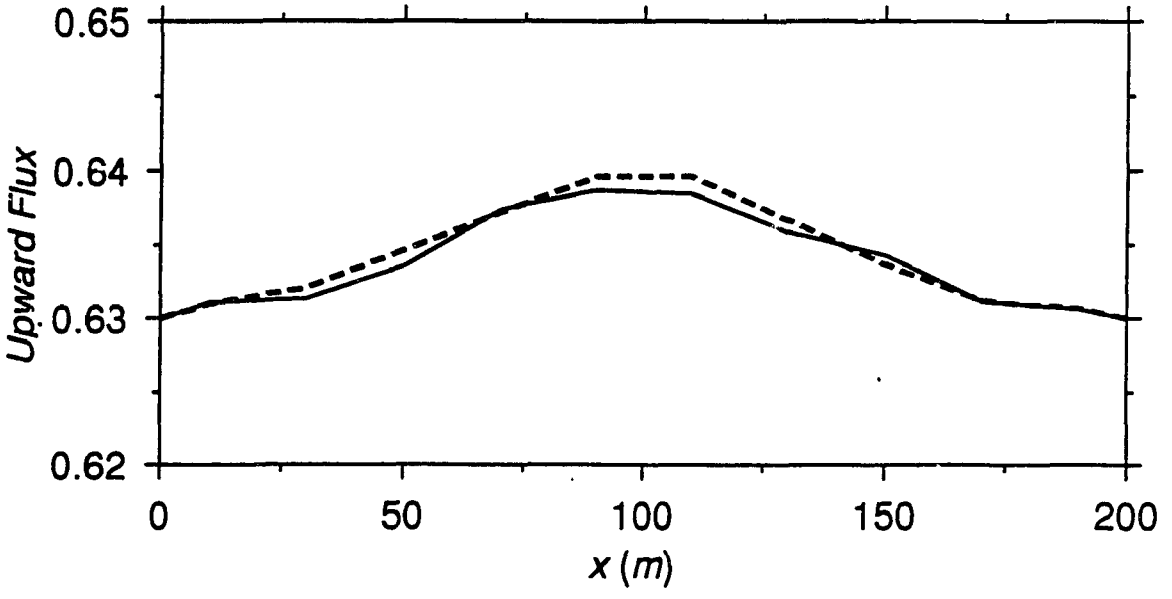

Figure 5.2: One-dimensional distributions of the upward irradiance. The g and ω vary with the change of k (solid line) or constant equal to the averaged values (dashed line). Solar zenith angle $\theta_0 = 0°$. The irradiances are normalized with respect to $\mu_0 \pi F_0$.

Fig.5.2 shows the sensitivity of the distribution of irradiance to the variation of g and ω. Similar to the bulk reflectance, the corresponding variations of g and ω have little impact on the distribution of irradiance.

5.3 The anomalous distribution in reflectance for a cloud field with geometric structure variation

The above discussions are mostly for clouds with internal variation. The clouds were taken to have a simple planar geometry so that boundary conditions could be easily satisfied in analytical solutions. In this subsection we consider another kind of problem where the distribution of cloud reflectance corresponds to the geometric variation in the cloud top. We take a cloud field with a flat plane on the bottom, but periodic height variation on the top surface. This is the so called turret structure, which is commonly observed in stratocumulus clouds. We simply describe the cloud height variation as

$$z = z_0\{1 + \epsilon[\cos(ax) + \cos(by)]\}\,, \tag{5.3}$$

where z_0 is the unperturbed cloud height and $a = b = 2\pi/L$, L is the periodic length. The cloud internal optical properties are taken to be constant, since our interest here is in the geometric factor. The method mentioned in subsection 5.1 is adopted to obtain the distribution of the irradiance.

In Fig.5.3 we have taken the unperturbed cloud depth $z_0 = 500\,m$, cloud internal optical factors $k_0 = 0.05\,m^{-1}$, $g = 0.86$, $\omega = 0.999$, solar zenith angle $\theta_0 = 0^0$ and the perturbation coefficient $\epsilon = 0.2$. The cloud field is divided into ten by ten square columns, each with a constant depth. Two values of cloud periodic length are considered. For the periodic length $L = 200\,m$ in Fig.5.3a, similar to the case of internal inhomogeneity in Fig.5.1a, the distribution of the irradiance is larger in the central region opposite to the distribution of cloud vertical optical depth. This

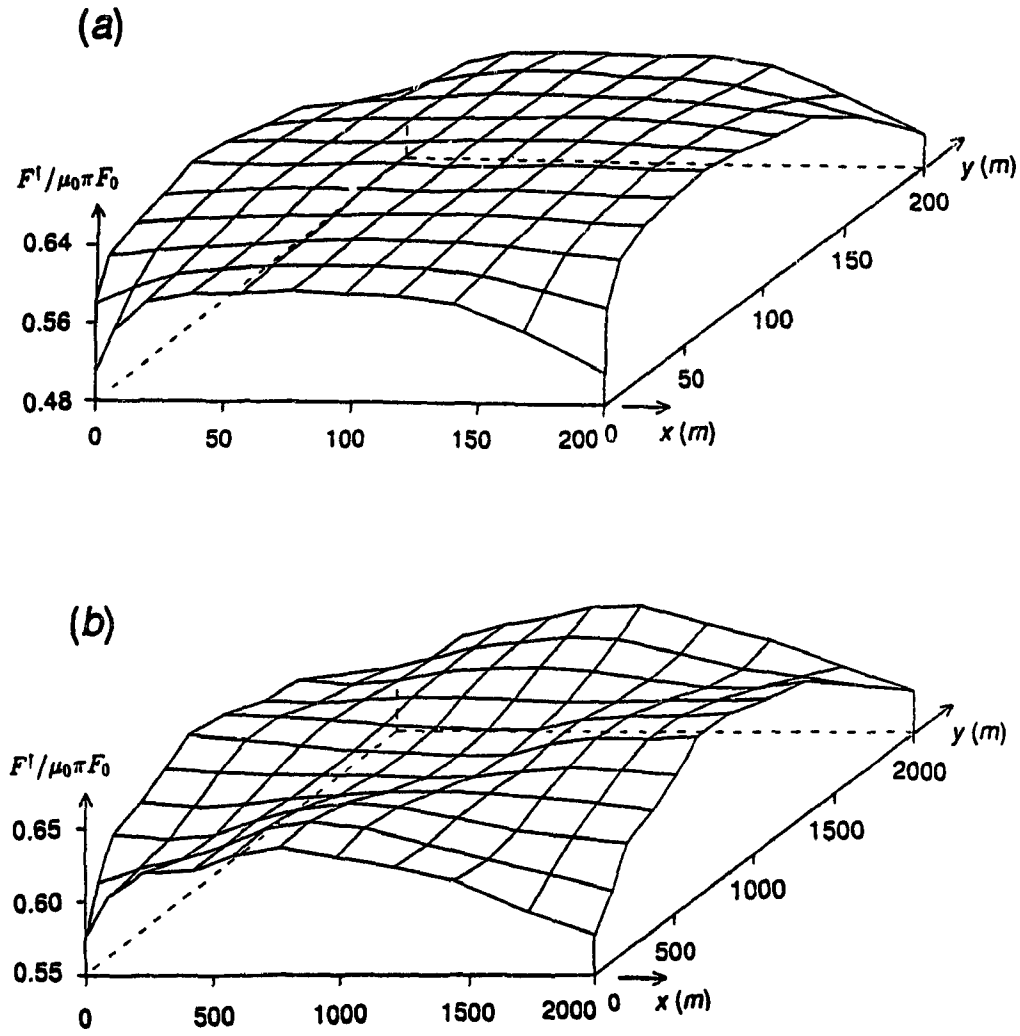

Figure 5.3: Two dimensional distributions of the upward irradiance for cloud field with height variation of Eq.(5.3). (a) $L = 200\,m$; (b) $L = 2000\,m$. Solar zenith angle $\theta_0 = 0°$. The cloud id internal homogeneous with optical parameters $k = 0.05m^{-1}$, $g = 0.86$, and $\omega = 0.999$. Unperturbated cloud depth $z_0 = 500m$. The irradiances are normalized with respect to $\mu_0\pi F_0$.

distribution is anomalous, since generally a thicker region of cloud should correspond to a larger reflectance. In comparison of Fig.5.3a with Fig.5.1a, the distribution in Fig.5.3a is very smooth except in the regions of the corners. When $L = 1000\,m$ the distribution is still anti-correlated, and the distribution is quite similar to that of Fig.5.3a. As the periodic length becomes larger (to $L = 2000\,m$ in Fig.5.3b), the distribution becomes more correlated with the geometric distribution of cloud field with less reflectance is in the central region.

The anomalous distribution is mostly due to multiple scattering inside the cloud. Photons transported upward from a thicker region to a thinner region can easily escape from the clouds. When the periodic length is large, the interaction between regions with different depths is weaker. The horizontally transported photons are not numerous enough to make an anti-correlated distribution. Therefore the distribution is likely to be more correlated to the distribution of the cloud depth.

We find in Fig.5.3 that average cloud irradiance is larger for the case of larger periodic length. The smaller periodic length represents a larger geometric variation. Therefore, the geometric inhomogeneity reduces the reflectance for the whole cloud field.

5.4 Again, on the cloud absorption anomaly

Fritz (1951) pointed out that the measurements of cloud absorption tended to exceed theoretical estimates. The measurements of cloud absorption are difficult and there is considerable variation in the numerical results. However, discrepancies of 20% to 50% are common. This is known as cloud absorption anomaly. In chapter 2, it was pointed out that one of the important factors for the enhancement of cloud solar absorption is the cloud internal vertical inhomogeneity. The physics is that more scattering events happen in the region (upper part of the clouds) with larger absorption (smaller single scattering albedo for cloud droplets). The enhancement of cloud absorption due to the vertical inhomogeneity of clouds can be up to 7% as

shown in chapter 2. The importance of this effect has not been realized before (see the review paper by Stephens and Tsay (1990)).

Since realistic radiative transfer processes in clouds are complex, other factors may also have a contribution, for example the aerosol effects as mentioned by Chýlek *et al.* (1984) and the water vapor effect (Davies *et al.*, 1984). It is pointed out here that the geometric effect is another important factor to take into account in considering the cloud absorption anomaly. Because of limitations in the theoretical calculations, the cloud anomaly refers only to planar clouds, i.e. the stratocumulus clouds. Therefore finite cloud size effects could not be considered. However, as we discussed in the last subsection the stratocumulus clouds always have a turret structure. What is the impact of such geometric variations on the cloud absorption?

For a comparison with the results in chapter 2, take cloud type A18 (Noonkester, 1984) as the cloud sample. As in chapter 2, in Fig.5.4 the cloud absorptions of cloud A18 with internal vertical inhomogeneity and its vertically averaged counterpart <A18> are considered. Also, the cloud top turret structures are considered by taking the cloud top height with the variation of Eq.(5.3). The perturbation coefficient is taken to be $\epsilon = 0.1$ in Fig.5.4. It is shown in Fig.5.4 that besides the existence of a difference in absorption between the cloud A18 and its vertically averaged counterpart <A18>, the top turret structure of the clouds would also result in further changes in cloud absorption. In Fig.5.4, several values of periodic length of L have been considered. For each value of L, the large enhancements of cloud absorption occur at small solar zenith angles. In Fig.5.4, without considering the cloud top geometric variation the vertical inhomogeneity can cause an increase of about 7% in cloud absorption for small zenith angle. However, the increase can be as much as 20% when the top turret structure effects are included. In Fig.5.4, when the solar beam is directly overhead, there is no further increase of cloud absorption due to the cloud turret structure in comparison with the case of vertical inhomogeneous cloud (A18). However, on average, the cloud top structures make a considerable increase in cloud absorptions. When the solar zenith angle is large the cloud top turret structure

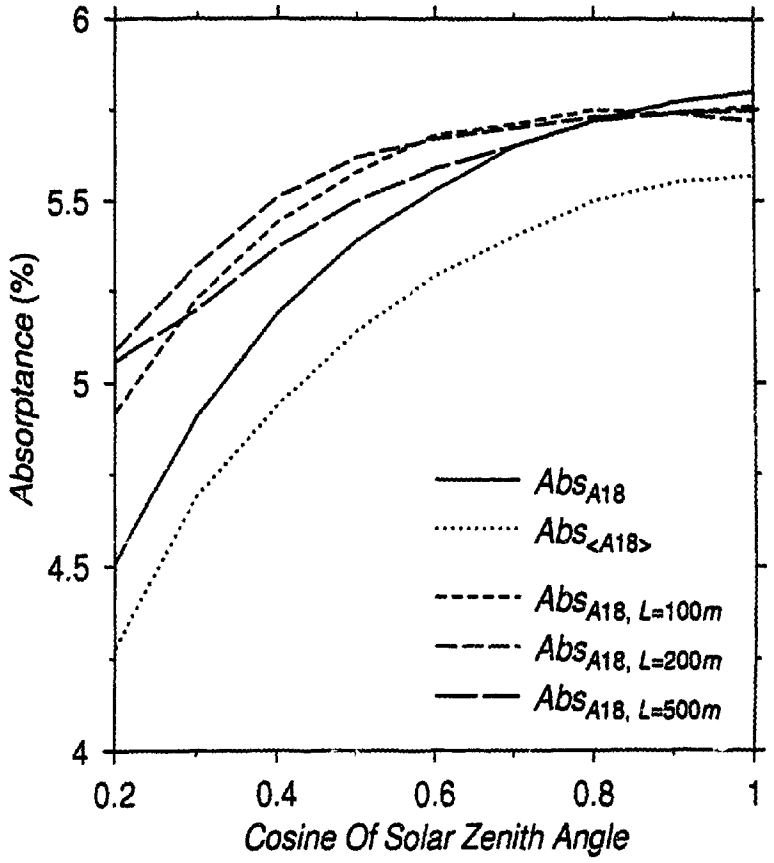

Figure 5.4: Cloud absorption for cloud A18 and its vertical averaged counterpart <A18>. Also cloud absorption for A18 with top cosinusoidal variation of different periodic lengths.

can decrease tne local incident angle. Therefore probability of reflection decreases, and the incoming photons are more like to be to be trapped in the top regions. As we mentioned in last two chapters the upper part of the clouds is very important in determination of cloud absorptance and reflectance, since the downward directed transport of solar photon number decreases exponentially inside the clouds. For small solar zenith angle the top turret structure would only slightly change the local incident angle for the incoming solar photons. Thus the change is small in cloud absorption.

The changes in cloud absorption in Fig.5.4 suggests that besides the cloud internal inhomogeneity the cloud top geometric variation is another factor which must be considered for an explanation of the cloud absorption anomaly.

5.5 Summary

The application of Monte Carlo simulations is limited due to the fact that the number of photons used is small in comparison with that of solar radiation. The Monte Carlo method is even difficult to apply to obtain the distribution of the reflected flux. In our method, the cloud top surface is separated into a number of regions, the reflectance for each region is taken to be similar to the plane-parallel case. However, inside the cloud the photon is allowed to transport from region to region. The interaction of the regions with different internal optical properties is considered. The anti-correlated distribution of the reflected photons has been shown in Monte Carlo simulations, which verifies the correctness of the perturbation theory in the previous two chapters.

The anomalous distribution of the reflectance happens not only for a cloud with internal inhomogeneity, but also for a cloud with geometric structural variation. The thicker regions of clouds may correspond to smaller reflectance. Radiative transfer is a complicated process, there are still a lot of phenomena remaining to be studied. Cloud top turret structure can also increase the cloud absorption,. This is an additional important factor that should considered in an explanation of the cloud absorption anomaly.

Chapter 6

Conclusions and Outlook for Further Work

The primary objective of this study was to investigate solar radiative transfer through clouds with internal inhomogeneity. The thesis consists two main components: Monte Carlo simulations of solar radiative transfer through clouds with vertical inhomogeneity; the development of perturbation method to solve analytically the 3D radiative transfer equation for a cloud field with internal horizontal variation. Monte Carlo simulations were also used to verify the results obtained through perturbation method.

In the first part, a Monte Carlo model was created to account for spatially varying cloud micro-physical properties. Calculations were performed to determine the properties of radiative transfer through clouds with internal inhomogeneity. Although there are large changes in LWC (extinction coefficient) in stratocumulus clouds, in the overcast cloud case the reduction in reflectance was found to be very small (around 1%) for a real cloud with internal vertical inhomogeneity in comparison with the vertical averaged counterpart. This showed that the plane-parallel approximation is a good model for planar clouds despite large changes in LWC. However, in broken cloud cases, the difference in reflectances between the vertically inhomogeneous cloud and its averaged counterpart was found to increase for large solar zenith angles. The difference was found to be generally less than 10%.

The cloud internal inhomogeneity and cloud top turret structures can increase the cloud absorption. These factors should be considered in an explanation of the cloud absorption anomaly. The increase in cloud absorption is up to 20% when the two factors are included..

In the second part of the thesis, an analytical solution of the 3D radiative transfer equation in a horizontally inhomogeneous medium with an arbitrary periodic variation in the extinction coefficient was obtained. Although there are some previous works on radiative transfer through clouds with internal inhomogeneity, the methods are all numerical or partly analytical. The occurrence of an anti-correlated distribution of the diffuse radiative intensity and of a horizontal shift in the distribution of diffuse radiative intensity, relative to the extinction coefficient are interesting new results that were found from this work. These phenomena show that the retrieved brightness of cloud images may not correspond to the cloud internal optical properties. The anti-correlated distributions of the reflected photons have been confirmed using the Monte Carlo simulations. It was found that the anomalous distribution of the reflectance also occurs in clouds with geometric structural variations. The thicker regions of clouds might correspond to smaller reflectance.

The solutions show that the cloud internal inhomogeneity has a larger influence on the distribution of the reflected number of photons than on the cloud albedo. Changes in the albedo occur only when the second order perturbation correction is included. Therefore, the change in cloud albedo is one order smaller than that of the perturbation coefficient. Contrary to the common belief that cloud internal inhomogeneity always decreases the cloud albedo, it was found that in some cases the cloud internal inhomogeneity can increase the cloud albedo as well.

The new physical findings in the thesis are: 1. Cloud internal inhomogeneity and cloud top turret structure can increase the cloud absorption. 2. Anti-correlated distributions of the reflected radiative intensity (flux) can occur for clouds with internal variations or with top geometric variations. 3. Cloud internal inhomogeneity can increase cloud albedo in some cases.

There are several recommendation for future research. First, in above Monte Carlo simulations, only clouds with internal inhomogeneity in the distribution of its droplets have been considered. However, the water vapor inside cloud is also a very important factor to radiative transfer processes. The distribution of water vapor inside clouds is also inhomogeneous. The inhomogeneous distributions of droplets and water vapor should be considered in further work. The spectral dependency of the reflectance and absorptance should be analysed. The cloud anomalous absorption will be better understood when this work is performed.

Second, the perturbation method for 3D radiative transfer in an internally inhomogeneous cloud will be extended to include the spatial variation of extinction coefficient asymmetry factor and the single scattering albedo, if the correlation of the three optical parameters are known. In perturbation solutions, the δ-Eddington approximation has been used in which only the lowest mode of local angular part of the radiance is considered. For higher accuracy the next order term of the spherical harmonic expansion will be needed. The corresponding analytical solution will become much more complicated.

Third, Monte Carlo models or other numerical simulations are very time consuming and are hard to be applied directly to climate models that include cloud-radiative interactions. Since any analytical solution can be easily included in climate models, it is hoped that through further improvement the perturbation model presented here can be applied to climate models.

Appendix A

Eq.(3.42) is an inhomogeneous partial differential equation with four particular solutions. Let $I_0^1 = L_1 + L_2 + L_3 + L_4$ (Zauberer, 1983), where the functions L_1 to L_4 satisfy

$$\nabla^2 L_1 - \lambda^2 L_1 = \cos(ax)[2\lambda^2 I_0^0 - 2he^{-k_0' z/\mu_0} + \frac{k_0' h}{\mu_0 \eta}\sin(\eta z)e^{-k_0' z/\mu_0}] , \qquad (A.1)$$

$$\nabla^2 L_2 - \lambda^2 L_2 = \cos(by)[2\lambda^2 I_0^0 - 2he^{-k_0' z/\mu_0} + \frac{k_0' h}{\mu_0 \zeta}\sin(\zeta z)e^{-k_0' z/\mu_0}] , \qquad (A.2)$$

$$\nabla^2 L_3 - \lambda^2 L_3 = \sin(ax)\frac{k_0' h}{\mu_0 \eta}[1 - \cos(\eta z)]e^{-k_0' z/\mu_0} , \qquad (A.3)$$

$$\nabla^2 L_4 - \lambda^2 L_4 = \sin(by)\frac{k_0' h}{\mu_0 \zeta}[1 - \cos(\zeta z)]e^{-k_0' z/\mu_0} . \qquad (A.4)$$

By Fourier expansion

$$L_1 = M_{10} + \sum_{n=1}[M_{1n}\cos(nax) + N_{1n}\sin(nax)] , \qquad (A.5)$$

where

$$M_{1n}(y,z) = \frac{a}{\pi}\int_0^{2\pi/a} L_1 \cos(nax)\, dx \qquad (n = 0, 1, 2, \cdots) , \qquad (A.6)$$

$$N_{1n}(y,z) = \frac{a}{\pi}\int_0^{2\pi/a} L_1 \sin(nax)\, dx \qquad (n = 1, 2, 3, \cdots) . \qquad (A.7)$$

Substituting Eq.(A.5) into Eq.(A.1) and using the orthogonality relation of the different modes, we obtain

$$(\frac{\partial^2}{\partial y^2}+\frac{\partial^2}{\partial z^2})M_{11}-\lambda_{11}^2 M_{11}=2\lambda^2 I_0^0-2he^{-k_0'z/\mu_0}+\frac{k_0'h}{\mu_0\eta}\sin(\eta z)e^{-k_0'z/\mu_0}\ , \qquad (A.8)$$

$$(\frac{\partial^2}{\partial y^2}+\frac{\partial^2}{\partial z^2})M_{1n}-\lambda_{1n}^2 M_{1n}=0 \qquad (n=0,2,3,\cdots)\ , \qquad (A.9)$$

$$(\frac{\partial^2}{\partial y^2}+\frac{\partial^2}{\partial z^2})N_{1n}-\lambda_{1n}^2 N_{1n}=0 \qquad (n=1,2,3,\cdots)\ . \qquad (A.10)$$

where $\lambda_{1n}^2=\lambda^2+(na)^2$.

The Eqs.(A.9) and (A.10) are homogeneous differential equations without a source term, which turn out to have only zero solutions under the required boundary conditions of Eqs.(3.45) and (3.46). The Eq.(A.8) has the solution

$$M_{11}=(c_{11}e^{-l_y y}+c_{12}e^{l_y y})(c_{13}e^{-l_z z}+c_{14}e^{l_z z})+f(z)\ , \qquad (A.11)$$

where c_{1i} are constants, $f(z)$ is a particular solution, l_y and l_z are eigen-wave vector components in y and z directions determined by boundary conditions, and $l_y^2+l_z^2=\lambda_{11}^2$. Since the particular solution is a function of z only, and the medium is of infinite extent in the y direction, we can only choose $l_y=0$. Therefore

$$M_{11}=C_1e^{-\lambda_1 z}+D_1e^{\lambda_1 z}-C\gamma_1e^{-\lambda z}-D\gamma_1e^{\lambda z}$$

$$-[\alpha_1-A_1\sin(\eta z)-B_1\cos(\eta z)]e^{-k_0'z/\mu_0}\ , \qquad (A.12)$$

where $\lambda_1^2=\lambda_{11}^2=\lambda^2+a^2$, $\gamma_1=2\lambda^2/a^2$, $\alpha_1=2(\lambda^2\alpha^2+h)\mu_0^2/(k_0'^2-\mu_0^2\lambda_1^2)$,

$$A_1=\frac{Qk_0'h/\mu_0\eta}{Q^2+(2k_0'\eta/\mu_0)^2}\ , \quad B_1=\frac{2h(k_0'/\mu_0)^2}{Q^2+(2k_0'\eta/\mu_0)^2}\ ,$$

with $Q=(k_0'/\mu_0)^2-\eta^2-\lambda_1^2$.

C_1 and D_1 are constants determined by boundary conditions. Similarly we let $L_2 = \cos(by)M_{21}(z)$, $L_3 = \sin(ax)N_{31}(z)$ and $L_4 = \sin(by)N_{41}(z)$, (all modes of zero solution can be neglected) and we obtain

$$M_{21} = C_2 e^{-\lambda_2 z} + D_2 e^{\lambda_2 z} - C\gamma_2 e^{-\lambda z} - D\gamma_2 e^{\lambda z}$$
$$- [\alpha_2 - A_2 \sin(\zeta z) - B_2 \cos(\zeta z)] e^{-k_0' z/\mu_0} , \qquad (A.13)$$

$$N_{31} = C_3 e^{-\lambda_1 z} + D_3 e^{\lambda_1 z} - [-\alpha_3 - B_1 \sin(\eta z) + A_1 \cos(\eta z)] e^{-k_0' z/\mu_0} , \qquad (A.14)$$

$$N_{41} = C_4 e^{-\lambda_2 z} + D_4 e^{\lambda_2 z} - [-\alpha_4 - B_2 \sin(\zeta z) + A_2 \cos(\zeta z)] e^{-k_0' z/\mu_0} , \qquad (A.15)$$

where $\lambda_2^2 = \lambda^2 + b^2$, $\gamma_2 = 2\lambda^2/b^2$, $\alpha_2 = 2(\lambda^2\alpha^2 + h)\mu_0^2/(k_0'^2 - \mu_0^2\lambda_2^2)$, $\alpha_3 = k_0'\mu_0 h/\eta(k_0'^2 - \mu_0^2\lambda_1^2)$, $\alpha_4 = k_0'\mu_0 h/\zeta(k_0'^2 - \mu_0^2\lambda_2^2)$,

$$A_2 = \frac{Rk_0' h/\mu_0\zeta}{R^2 + (2k_0'\zeta/\mu_0)^2} , \quad B_2 = \frac{2h(k_0'/\mu_0)^2}{R^2 + (2k_0'\zeta/\mu_0)^2} ,$$

with $R = (k_0'/\mu_0)^2 - \zeta^2 - \lambda_2^2$. The constants C_2, D_2; C_3, D_3; and C_4, D_4 are determined by the boundary conditions.

Appendix B

The coefficients in Eq.(4.28) are: $\lambda_{ijkl}^2 = \lambda^2 + [\pi(i+k)/a]^2 + [\pi(j+l)/b]^2$,
$\Omega_{ijkl} = \Phi_{ijkl}/(\lambda_{kl}^2 - \lambda_{ijkl}^2)$, $\Omega_{ijkl}^* = \Phi_{ijkl}/(2\lambda_{kl})$,
$\Gamma_{ijkl} = (\Gamma_{kl}\Phi_{ijkl} - \lambda^2)/[\lambda^2 - \lambda_{kl}^2]$, $\Gamma_{ijkl}^* = (\Gamma_{kl}\Phi_{ijkl} - \lambda^2)/(2\lambda)$,
$\alpha_{ijkl} = [h + \lambda^2\alpha + \Phi_{ijkl}\alpha_{kl} - hk_0'^2/(2\mu_0^2\xi_{ij}\xi_{kl})]/[(k_0'/\mu_0)^2 - \lambda_{ijkl}^2]$,
$\beta_{ijkl} = [\Phi_{ijkl}\beta_{kl} + 2k_0'h/(\mu_0\xi_{kl})]/[(k_0'/\mu_0)^2 - \lambda_{ijkl}^2]$,

$$A_{ijkl} = \frac{\bar{A}_{ijkl}R_{ijkl} + 2k_0'\xi_{kl}\bar{B}_{ijkl}/\mu_0}{R_{ijkl}^2 + (2k_0'\xi_{kl}/\mu_0)^2},$$

$$B_{ijkl} = \frac{-\bar{B}_{ijkl}R_{ijkl} + 2k_0'\xi_{kl}\bar{A}_{ijkl}/\mu_0}{R_{ijkl}^2 + (2k_0'\xi_{kl}/\mu_0)^2},$$

with $\bar{A}_{ijkl} = \Phi_{ijkl}A_{kl} - hk_0'^2/(2\mu_0^2\xi_{ij}\xi_{kl})$, $\bar{B}_{ijkl} = \Phi_{ijkl}B_{kl} + 2hk_0'/(\mu_0\xi_{kl})$,
$R_{ijkl} = (k_0'/\mu_0)^2 - \xi_{kl}^2 - \lambda_{ijkl}^2$.

$$S_{ijkl} = \frac{hk_0'^2Q_{ijkl}/(2\mu_0^2\xi_{ij}\xi_{kl})}{Q_{ijkl}^2 + [2k_0'(\xi_{ij} + \xi_{kl})/\mu_0]^2},$$

$$T_{ijkl} = \frac{hk_0'^3(\xi_{ij} + \xi_{kl})/(\mu_0^3\xi_{ij}\xi_{kl})}{Q_{ijkl}^2 + [2k_0'(\xi_{ij} + \xi_{kl})/\mu_0]^2},$$

with $Q_{ijkl} = (k_0'/\mu_0)^2 - (\xi_{ij} + \xi_{kl})^2 - \lambda_{ijkl}^2$.

Bibliography

AIDA, M. (1973). Reflection of solar radiation from an array of cumuli. *J. Meteor. Soc. Japan*, 55:174–181.

BARKER, H. W. AND DAVIES, J. A. (1992). Solar radiative fluxes for stochastic, scaling invariant broken cloud field. *J. Atmos. Sci.*, 49:1115–1126.

BOX, M. A., GERSTEL, S. A. W. AND SIMMER, C. (1989). Computation of atmospheric radiative effects via perturbation theory. *Contrib. Atmos. phys.*, 62:193–199.

BRADLEY, S. G. (1981). The relation between cumulus albedo and extinction coefficient and its application to remote sensing. *J. Atmos. Sci.*, 38:2243–2256.

BREON, F. M. (1992). Reflectance of broken cloud field: Simulation and paramerization. *J. Atmos. Sci.*, 49:1221–1232.

BUSYGIN, V. P., YEVSTRATOV, N. A. AND FEIGELSON, E. M. (1973). Optical properties of cumulus and radiant fluxes for cumulus cloud cover. *Izv. Atmos. Ocean. Phys.*, 9:1142–1151.

CAHALAN, R. F. AND SNIDER, J. B. (1989). Marine stratocumulus structure. *Remote Sens. Environ.*, 28:95–107.

CHÝLEK, P., RAMASWAMY, V., AND CHENG, R. J. (1984). Effect of graphitic carbon on the albedo of clouds. *J. Atmos. Sci.*, 41:3076–3084.

DAVIES, R. (1978). The effect of finite geometry on the three-dimensional transfer of solar irradiance in clouds. *J. Atmos. Sci.*, 35:1712–1725.

DAVIES, R., RIDGWAY, W. L. AND K. KYUNG EAK, R J. (1984). Spectral absorption of solar radiation in cloudy atmosphere: a 20 cm^{-1} model. *J. Atmos. Sci.*, 41:2126–2137.

EVANS, F. (1993). Two-dimensional radiative transfer in cloudy atmosphere: The spherical harmonic spatial grid method. *J. Atmos. Sci.*, 50:3111–3124.

FOUQUART, Y., BRUIEZ, J. C., HERMAN, M. AND KANDEL, R. S. (1990). The influence of clouds on radiation: a climate-modeling perspective. *Rev. Geophys.*, 28:145–166.

FRITZ, S. (1951). *Solar radiant energy.* Compendium of Meteorology, T. F. Malone, Ed., Wiley, 14-29.

GOODY, B. M. AND YUNG, Y. L. (1989). *Atmospheric radiation.* Oxford University Press, Oxford, 519 pp.

HARSHVARDHAN AND THOMAS, R. W. L. (1984). Solar reflection from interacting and shadowing cloud elements. *J. Geophys. Res.*, 89:7179–7185.

HARSHVARDHAN AND WEINMAN, J. A. (1982). Infrared radiative transfer through a regular array of cuboidal clouds. *J. Atmos. Sci.*, 39:431–439.

JOSEPH, J. H., WISCOMBE, W. J., AND WEINMAN, J. A (1976). The delta Eddington approximation for radiative flux transfer. *J. Atmos. Sci.*, 33:2452–2459.

KOBAYASHI, T. (1988). Parameterization of reflectivity for broken cloud. *J. Atmos. Sci.*, 45:3034–3045.

KOBAYASHI, T. (1991). Reflected solar flux for horizontally inhomogeneous atmospheres. *J. Atmos. Sci.*, 48:2436–2447.

MASON, B. J. (1971). *The physics of clouds.* Clarendon press, Oxford, 671 pp.

MCKEE, T. B. AND COX, S. K. (1974). Scattering of visible radiation by finite clouds. *J. Atmos. Sci.*, 31:1885–1892.

NOONKESTER, V. R. (1984). Droplet spectra observed in marine stratus cloud layers. *J. Atmos. Sci.*, 41:829–845.

PALTRIDGE, G. W. (1974). Infrared emissivity, short wave albedo, and the microphysics of stratiform water clouds. *J. Geophys. Res.*, 79(27):4053–4058.

PLATT, C. M. R. (1976). Infrared absorption and liquid water content in stratocumulus clouds. *Quart. J. Roy. Meteor. Soc.*, 102:515–522.

PREISENDORFER, W. R. AND STEPHENS, G. L. (1984). Multimode radiative transfer in finite optical media. I: solution. *J. Atmos. Sci.*, 41:709–724.

RAMASWAMY, V. AND DETWILER, A. (1986). Interdependence of radiation and microphysics in cirrus clouds. *J. Atmos. Sci.*, 43:2289–2301.

ROMANOVA, L. M. (1975). Radiative transfer in an inhomogeneous scattering medium. *Izv. Acad. Sci. USSR Atmos. Oceanic. Phys.*, 11:509–513.

SCHMETZ, J. (1984). On the parameterization of the radiative properties of broken clouds. *Tellus*, 36A:417–432.

SHETTLE, E. P. AND WEINMAN, J. A. (1971). The transfer of solar irradiance through inhomogeneous turbid atmospheres evaluated by eddington's approximation. *J. Atmos. Sci.*, 28:1048–1054.

SLINGO, A. (1989). A gcm parameterization for the shortwave radiative properties of water clouds. *J. Atmos. Sci.*, 43:1419–1427.

SLINGO, A., BROWN, R. AND WRENCH, C. L. (1982a). A field study of nocturnal stratocumulus:iii. high resolution radiative and microphysical observations. *Quart. J. Roy. Meteor. Soc.*, 108:145–165.

SLINGO, A., NICHOLLS, S. AND SCHMETZ, J. (1982b). Aircraft observations of marine atratocumulus during jasin. *Quart. J. Roy. Meteor. Soc.*, 108:833–856.

SPANIER, J. AND GELBARD, E. M. (1969). *Monte Carlo principles and neutron transport.* Addison-Wesley, 234 pp.

STEPHENS, G. L. (1983). The influence of radiative transfer on the mass and heat budgets of ice crystals falling in the atmosphere. *J. Atmos. Sci.*, 40:1729–1739.

STEPHENS, G. L. AND PREISENDORFER, R. W. (1984). Multimode radiative transfer in finite optical media. II: solution. *J. Atmos. Sci.*, 41:725–735.

STEPHENS, G. L. AND TSAY, S. C. (1990). On the cloud absorption anomaly. *Quart. J. Roy. Meteor. Soc.*, 116:671–704.

WEINMAN, J. A. AND HARSHVARDHAN (1982). Solar reflection from a regular array of horizontally finite clouds. *Appl. Optics*, 21:2940–2944.

WEINMAN, J. A. AND SWARZTRAUBER, P. N. (1967) Albedo of a striated medium of isotropically scattering particales. *J. Atmos. Sci.*, 25:497–501.

WELCH, R. M. AND WIELICKI, B. A. (1984). Stratocumulus cloud field reflected fluxes: The effect of cloud shape. *J. Atmos. Sci.*, 41:3085–3103.

WELCH, R. M. AND WIELICKI, B. A. (1985). A radiative parameterization of stratocumulus cloud fields. *J. Atmos. Sci.*, 42:2888–2897.

WISCOMBE, W. J., WELCH, R. M. AND HALL, W. D. (1985). The effects of very large drops on cloud absorption, Part I: parcel models. *J. Atmos. Sci.*, 41:1336–1355.

ZAUBERER, E. (1983). *Partial differential equations of applied mathematics.* Wiley interscience, New York, 779 pp.